

University of Stuttgart
Germany

Short-Range Surface Plasmonics on Single Crystalline Gold Platelets

Von der Fakultät Mathematik und Physik der Universität Stuttgart
zur Erlangung der Würde eines Doktors der
Naturwissenschaften (Dr. rer. nat.) genehmigte Abhandlung

vorgelegt von
Bettina Frank
aus Marbach

Hauptberichter: Prof. Dr. Harald Giessen
Mitberichter: Prof. Dr. Peter Michler
Vorsitzender: Prof. Dr. Günter Wunner

Tag der mündlichen Prüfung: 28.06.2016

4. Physikalisches Institut der Universität Stuttgart

Juni 2016

Bettina Frank:

Short-Range Surface Plasmonics on Single Crystalline Gold Platelets

I hereby certify that this dissertation is entirely my own work except where otherwise indicated. Passages and ideas from other sources have been clearly indicated.

Stuttgart, June 2016

Bettina Frank

ABSTRACT

Purpose of this work is the excitation and manipulation of surface plasmon polaritons on atomically flat and single crystalline gold platelets, deposited on doped silicon substrates.

Therefore, a new procedure has been introduced to synthesize single crystalline gold platelets electrochemically. Within this chemical reaction, a gold electrode is dissolved due to a cyclic voltammetry experiment, which is performed within dilute hydrochloric acid. During this process, gold atoms in the electrolyte form crystalline seeds. During the reaction more atoms attach to this nucleus in a two-dimensional, single crystalline fashion. Finally, after a certain reaction time, these gold platelets precipitate onto a suitable substrate and can be used for plasmonic experiments. The sample consists of a statistical ensemble of triangular and hexagonal gold platelets, exhibiting lateral dimensions in the micrometer range.

These platelets are fully characterized by various analytical methods. Energy dispersive x-ray measurements indicate that electrochemically grown platelets consist of pure gold. Low energy electron microscopy and atomic force microscopy are performed to characterize the surface quality. Both procedures reveal that electrochemically grown gold platelets have atomically flat surfaces without defects, inhomogeneities, or protrusions. Information about the atomic arrangement is provided by transmission electron microscopy. Selected area electron diffraction shows hexagonal atomic arrangement on each platelet spot. This implies single crystallinity in the (111) direction, which is supported by the substrate. Our platelets represent the best ever gold surfaces and nanostructures, which are as close to theoretical gold as possible. Furthermore, the transmission electron microscope facilitates collective electron oscillations due to high energy electron impact. Energy filtered electron loss images illustrate the platelet particle

plasmon modes of several orders.

Two-photon photoemission microscopy is a versatile tool for surface plasmon polariton excitation and imaging of the propagating plasmons as well as the emitted photo-electrons. Single crystalline gold platelets attached to a silicon substrate support one surface plasmon polariton at each interface. Due to different adjacent materials, these surface plasmon polaritons have different wavelengths and therefore are defined as long- and short range surface plasmon polaritons. Utilizing thin gold platelets between 20 and 30 nm thickness, both surface plasmon polaritons can be excited and imaged simultaneously at 800 nm excitation wavelength. From time-resolved measurements, the phase velocity of propagating surface plasmon polaritons is determined to be just about a quarter of the velocity of light in vacuum, hence the plasmon wavelength is also reduced by a factor of four when compared to the speed of light in vacuum.

Focused ion beam milling allows patterning of single crystalline gold platelets. During the structuring process, different disk and line patterns are milled into gold platelets to focus the short range surface plasmon polariton, leading to a spot of electron emission with minimum lateral size of 60 nm. This is less than one tenth of the vacuum wavelength of the exciting laser. Pump-probe experiments provide the dynamic behavior of the focused short range surface plasmon polariton and show alternating constructive and destructive interference of counter-propagating waves.

Circularly polarized light not only excites short range surface plasmon polaritons at sharp structural edges, but also transfers orbital angular momentum. This phenomenon is investigated on different Archimedean spiral structures of increasing topological charge l .

Finally, stadium structures on single crystalline gold platelets represent the first step towards a plasmonic stadium billiard experiment.

ZUSAMMENFASSUNG

Ziel dieser Arbeit ist die Untersuchung und Manipulation von Oberflächenplasmonen. Diese werden an Mikrometer großen, atomar glatten, einkristallinen Goldplättchen auf dotierten Siliziumsubstraten angeregt.

Hierzu wurde ein neues Verfahren entwickelt, das die elektrochemisch Synthese einkristalliner Goldplättchen ermöglicht. Bei dieser chemischen Reaktion wird eine Goldelektrode mittels zyklischer Voltammetrie in einem Salzsäure-Elektrolyten aufgelöst. Hierbei können Goldatome im Elektrolyten kristalline Keime bilden. Während des Reaktionsablaufes werden ständig weitere Atome an die Keime angelagert, die nach einiger Zeit auf dem Substrat ausfallen und vorzugsweise in lateraler Richtung zu einem zweidimensionalen Goldplättchen weiter wachsen. Die fertige Probe besteht aus einem Ensemble von dreieckigen und sechseckigen Strukturen unterschiedlicher Größe.

Im Rahmen dieser Arbeit werden die elektrochemisch gewachsenen Goldplättchen mit verschiedenen Analysemethoden charakterisiert. Ihre besonderen Eigenschaften werden im Folgenden kurz zusammengefasst. Sie sind ausschließlich aus Goldatomen aufgebaut und haben atomar glatte Oberflächen, ohne Defektstellen und Unebenheiten. Elektronenbeugung im Transmissions-Elektronenmikroskop zeigt sechszählige Anordnung der Atome an jeder untersuchten Stelle. Dies bedeutet Einkristallinität in 111-Richtung, welche durch das Substrat hervorgerufen wird. Damit stellen sie die bisher besten, jemals hergestellten Goldstrukturen dar, die so nah wie nur möglich am theoretisch idealen Gold sind. Des Weiteren lassen sich durch Wechselwirkung mit hochenergetischen Elektronen im Transmissions-Elektronenmikroskop kollektive Elektronenschwingungen im Goldplättchen anregen. Eine energieaufgelöste Bilderserie zeigt Partikelplasmon-Moden verschieden hoher Ordnungen.

Zwei-Photonen Photoemissions Mikroskopie eignet sich hervorragend, um Oberflächenplasmonen an den beiden Grenzflächen elektrochemisch hergestellter Goldplättchen anzuregen und auch abzubilden. Aufgrund unterschiedlicher Umgebungsmaterialien auf beiden Seiten haben die jeweiligen Oberflächenplasmonen unterschiedliche Wellenlängen und werden als lang- und kurzreichweitige Oberflächenplasmonen bezeichnet. Werden sehr dünne einkristalline Goldplättchen von nur 20 bis 30 nm Dicke verwendet, kann man Oberflächenplasmonen an beiden Materialgrenzflächen bei einer Anregungswellenlänge von 800 nm gleichzeitig anregen und abbilden. Aus zeitaufgelösten Messungen lässt sich die Phasengeschwindigkeit der kurzreichweitigen Oberflächenplasmonen bestimmen, die ungefähr ein Viertel der Lichtgeschwindigkeit im Vakuum beträgt. Die Plasmonenwellenlänge ist gegenüber der Vakuum-Lichtwellenlänge ebenfalls um den Faktor 4 reduziert.

Mit einem fokussierten Galliumionenstrahl lassen sich beliebige Strukturen in einkristalline Goldplättchen schneiden. Um das kurzreichweitige Oberflächenplasmon zu fokussieren, werden verschiedene Kreis- und Linienstrukturen aus den einkristallinen Goldplättchen herausgeschnitten. Der kleinste Fokussdurchmesser dieser emittierten Elektronen beträgt 60 nm, was weniger als 1/10 der Vakuum-Lichtwellenlänge des anregenden Lasers beträgt. Aus zeitaufgelösten Messungen wird das dynamische Verhalten des fokussierten Oberflächenplasmons bestimmt. Die Plasmondynamik im Fokusspunkt wird von abwechselnd konstruktiv und destruktiv interferierenden, entgegelaufenden Plasmonwellen bestimmt.

Zirkular polarisiertes Licht regt Oberflächenplasmonen nicht nur an den strukturierten Kanten an, sondern kann auch seinen intrinsische Drehimpuls auf die Plasmonenwellen übertragen. Dies wird an Archimedischen Spiralstrukturen unterschiedlich großer geometrischer Ordnung m untersucht.

Abschließend werden mit Hilfe von verschiedenen Stadionstrukturen auf großen einkristallinen Goldplättchen erste Versuche zur

Realisierung eines plasmonischen Stadionbilliard-Experimentes
vorgestellt.

PUBLICATIONS

Parts of this theses and the dissertation work will be published:

- B. Frank, P. Kahl, D. Podbiel, G Spektor, M. Orenstein, L. Fu, T. Weiss, M. Horn-von Hoegen, T. J. Davis, F.-J. Meyer zu Heringdorf, and H. Giessen
"Short-range surface plasmonics: Localized Electron Emission Dynamics from a 60 nm Spot on an Atomically Flat Single Crystalline Gold Surface" (2016)
- B. Frank, A. Ruff, W. Sigle, L. Fu, P. Kahl, F.-J. Meyer zu Heringdorf, S. Ludwigs, and H. Giessen
"Electrochemical route to micrometer-sized single crystalline gold platelets for plasmonic applications" (2016)
- G. Spektor, D. Kilbane, A. K. Mahro, B. Frank, S. Ristok, L. Gal, P. Kahl, D. Podbiel, S. Mathias, H. Giessen, F.-J. Meyer zu Heringdorf, M. Orenstein, M. Aeschlimann
"Revealing the attosecond dynamics of spin-orbit conversion in plasmonic nano vortices" (2016)

Additional scientific publications which are not presented in this thesis:

- D. Podbiel, P. Kahl, A. Makris, S. Sindermann, B. Frank, H. Giessen, M. Horn-von Hoegen, F.-J. Meyer zu Heringdorf
"Plasmoemission: Nonlinear Emission of Electrons from Strong Plasmonic Fields"
submitted to Nature Physics (2016)
- J. Vogt, C. Huck, B. Frank, X. Yin, H. Giessen, A. Pucci, F. Neubrech
"Surface-Enhanced Infrared Spectroscopy Benefits From Monocrystalline Gold Antennas"
submitted to ACS Photonics (2016)

- Z. Wang, J. Zhao, B. Frank, Q. Ran, G. Adamo, H. Giessen, C. Soci
"Plasmon-Polaron Coupling in Conjugated Polymer on Infrared Nanoantennas"
 Nano Lett. **15**, 5382 (2015)
- J. Zhao, B. Frank, F. Neubrech, C. Zhang, P. V. Braun, H. Giessen
"Hole-mask colloidal nanolithography combined with tilted-angle-rotation evaporation: A versatile method for fabrication of low-cost and large-area complex plasmonic nanostructures and metamaterials"
 Beilstein J. Nanotechnol. **5**, 577 (2014)
- B. Frank, X. Yin, M. Schäferling, J. Zhao, S. Hein, P. V. Braun, H. Giessen
"Large-area 3D chiral plasmonic structures"
 ACS Nano **7**, 6321 (2013)
- L. Wollet, B. Frank, M. Schäferling, M. Mesch, S. Hein, H. Giessen
"Plasmon hybridization in stacked metallic nanocups"
 Opt. Mater. Express **2**, 1384 (2012)
- B. Gompf, B. Krausz, B. Frank, M. Dressel
"k-dependent optics of nanostructures: Spatial dispersion of metallic nanorings and split-ring resonators"
 Phys. Rev. B **86**, 075462 (2012)
- S. Cataldo, J. Zhao, B. Frank, F. Neubrech, C. Zhang, P. V. Braun, H. Giessen
"Hole-Mask Colloidal Nanolithography for Large-Area Low-Cost Metamaterials and Antenna-Enhanced SEIRA Substrates"
 ACS Nano **6**, 979 (2012)
- J. Zhao, B. Frank, S. Burger, H. Giessen
"Large-Area High-Quality Plasmonic Oligomers Fabricated"

by Angle-Controlled Colloidal Nanolithography"

ACS Nano 5, 9009 (2011)

At international conferences (only own presentations):

- B. Frank, P. Kahl, G. Spektor, D. Podbiel, D. Kilbane, T. Weiss, M. Horn-von Hoegen, M. Aeschlimann, F.-J. Meyer zu Heringdorf, H. Giessen

"Short-Range Surface Plasmonics on Atomically Flat Gold Surfaces: Localized Electron Emission Dynamics from a 60 nm Spot and Plasmons with Higher Orbital Angular Momentum"

Nanolight, Benasque, Spain (2016)

- B. Frank, A. Ruff, W. Sigle, L. Fu, P. Kahl, S. Ludwigs, P. van Aken, W. Osten, F.-J. Meyer zu Heringdorf, P. Braun, P. Mulvaney, H. Giessen

"Electrochemical route to mono-crystalline gold platelets for high quality plasmonics"

Advanced Architectures in Photonics, Prague, Czech Republic (2014)

- B. Frank, P. Kahl, A. Ruff, W. Sigle, L. Fu, T. Weiss, F.-J. Meyer zu Heringdorf, H. Giessen

"Observation of short-range plasmons and sub-100 nm nanofocusing on atomically flat gold platelets"

Advanced Photonics Congress, Barcelona, Spain (2014)

- B. Frank, A. Ruff, W. Sigle, L. Fu, S. Ludwigs, P. van Aken, W. Osten, H. Giessen

"Electrochemical route to large-area mono-crystalline gold platelets for plasmonic applications"

WE-Heraeus-Seminar: Active Nanoplasmonics and Metamaterial Dynamics, Bad Honnef, Germany (2014)

2. Poster award

- B. Frank, X. Yin, M. Schäferling, J. Zhao, S. Hein, P. V. Braun, H. Giessen

"Large-area 3D chiral plasmonic structures"

NATO ASI: Nanomaterials and Nanoarchitectures, Cork, Ireland (2013)

- B. Frank, J. Zhao, M. Schäferling, X. Yin, S. Hein, H. Giessen
“Low-cost large-area fabrication and chiral optical properties of 3D chiral plasmonic nanoantennas”
Near-Field Optics, Nanophotonics and Related Techniques, San Sebastian, Spain (2012)

CONTENTS

1	INTRODUCTION	1
2	THEORY OF SURFACE PLASMON POLARITONS	5
2.1	Electrodynamics at interfaces	6
2.2	Plasmons at Metal-Dielectric Interfaces	12
2.3	Plasmons at Vacuum-Gold-Silicon Interfaces	21
2.4	Excitation of Surface Plasmon Polaritons	24
2.4.1	Excitation with Electrons	24
2.4.2	Excitation with Light	24
3	THE PLASMONIC ANGULAR ORBITAL MOMENTUM	29
3.1	The Angular Orbital Momentum of Light	29
3.2	Plasmon Vortices	31
4	A BRIEF INTRODUCTION TO ELECTROCHEMISTRY	35
5	SINGLE-CRYSTALLINE GOLD PLATELETS	39
5.1	Overview	39
5.2	Electrochemical Reaction and Platelet Growth	40
5.3	In-situ characterization	42
5.4	General Characterization	47
5.4.1	Atomic Force Microscopy	47
5.4.2	Low Energy Electron Microscopy	50
5.4.3	Transmission Electron Microscopy	51
5.4.4	Electron Diffraction	52
5.5	Energy filtered transmission electron microscopy	54
6	EXPERIMENTAL METHODS	57
6.1	Focused Ion Beam Milling	57
6.2	Experimental Concept of Plasmon Excitation	59
6.3	Two-Photon Photoemission Microscopy	61
6.3.1	Setup and Experiment	61
6.3.2	Basic Principles	62

Contents

7	SHORT-RANGE SURFACE PLASMONICS	65
7.1	Long- and Short-Range Surface Plasmon Polaritons	66
7.2	Focusing Short-Range Surface Plasmon Polaritons .	73
7.3	The Plasmonic Orbital Angular Momentum	84
7.4	A Plasmonic Stadium Billiard Experiment	95
7.4.1	Preliminary Remarks	95
7.4.2	Concepts and Experiments	98
8	CONCLUSION AND OUTLOOK	105
A	APPENDIX	115
	BIBLIOGRAPHY	121
	ACKNOWLEDGEMENTS	133
	CURRICULUM VITAE	135

INTRODUCTION

Optics [1] explores the behavior and properties of light. In particular, interaction of light with matter is important in many scientific areas, providing the key to fundamental concepts. Generally, light can be interpreted as electromagnetic wave propagating through space. This was postulated by Maxwell in the year 1891, within his work "Treaties on Electricity and Magnetism" [2], introducing a comprehensive electrodynamic theory.

Microscopy is a fascinating application in optics that essentially contributes to the exploration of life since the 17th century. However, using visible light in optical microscopy, the image resolution is restricted due to the Abbe diffraction limit [3]. This indicates that objects can only be resolved if their distance is at least $\Delta d = \lambda / (2n \sin \alpha)$, because the diameter of the light focal spot can not be smaller than the distance Δd . Here, λ is the light wavelength, n is the refractive index of the sample and α is half of the objective opening angle.

Abbe's refraction limit has been overcome for the first time in the end of the 20th century by stimulated emission depletion (STED) microscopy [4]. Based on molecular fluorescence imaging, the resolution limit is overcome by scanning the sample with an infinitesimal excitation spot. Characteristic fluorescence signals allow imaging and conclusions about the molecular composition of the investigated sample.

Alternatively, plasmonics could offer possibilities to circumvent the Abbe limit. This could be realized by exploiting emitted sub-wavelength radiation from a focal plasmonic spot and use it as sub-wavelength source for illumination.

In general, plasmonics [5, 6] is a sub-area of optics that investigates collective oscillations of conduction band electrons in metals, which are stimulated due to interaction with electromagnetic

waves. One defines two fundamental types of plasmonic excitations. First, surface plasmon polaritons [7, 8], which are electron oscillations in metals, coupled to propagating electromagnetic waves. These excitations are located at metal-dielectric interfaces and confined evanescently in the perpendicular direction. The second type is called localized surface plasmon or particle plasmon [9, 10]. This is the non-propagating oscillation of conduction electrons, restricted to sub-wavelength metal particles or lithographically defined structures. The particle plasmon response is governed by structure geometry and arrangement, as well as coupling or mutual interaction of neighboring elements [11, 12].

Usually, gold is utilized in plasmonic experiments, due to its material robustness and outstanding optical properties. In reference [13], single crystalline gold has been established in plasmonics, exhibiting extraordinary high signals compared to polycrystalline gold.

In this work, electrochemically synthesized single crystalline gold platelets on silicon substrates, in combination with two-photon photoemission microscopy, are used for plasmonic focusing. This leads to a minimum spot size of 60 nm.

From chapter 2 to 4 theoretical and fundamental background information is provided to understand the experimental findings. In chapter 2, the dispersion relation of surface plasmon polaritons at a single metal-dielectric interface is derived. In a next step, a system of two metal-dielectric interfaces is considered. Based on the solutions of Maxwell's equations at metal-insulator interfaces and appropriate boundary conditions, two solutions are found for the insulator-metal-insulator system. Then, the experimental conditions are applied to these solutions and the dispersion relations of surface plasmon polaritons for a vacuum-gold-silicon system are determined analytically. Finally in chapter 2, several techniques for surface plasmon polariton excitation are introduced.

Chapter 3 briefly reviews light carrying spin orbital momentum and angular orbital momentum due to certain polarization states.

Furthermore, it is shown that orbital angular momentum from light can be transferred to surface plasmon polaritons.

Electrochemistry plays an important role within this work. Therefore, the basic concept of reduction and oxidation reactions in electrochemistry are introduced briefly in chapter 4.

There are several methods possible to synthesize single crystalline gold platelets. Here, single crystalline gold platelets are produced electrochemically, utilizing a completely new mechanism. In chapter 5, this electrochemical procedure is introduced in detail. Furthermore, the obtained single crystalline gold platelets are characterized in material composition, surface quality, and crystal structure.

In chapter 6, the experimental concept of surface plasmon polariton excitation via ultra-short laser pulses at the material interfaces of single crystalline gold platelets dispersed on silicon substrates is introduced. This measurement procedure is realized by two-photon photoemission microscopy, where emitted photoelectrons from the gold platelet interfaces are imaged. These experiments have been carried out at the labs of our collaborators Frank Meyer zu Heringdorf in Duisburg and Martin Aeschliemann in Kaiserslautern.

Chapter 7 summarizes all two-photon photoemission microscopy results. Surface plasmon polaritons are excited on both interfaces of structured, electrochemically synthesized, single crystalline gold platelets. Time-resolved measurements explain the dynamics of these surface plasmon polaritons.

Investigations of surface plasmon polaritons on single crystalline gold platelets are the main subject of this work. By definition, surface plasmon polariton (SPP)s are oscillations of the conduction electrons in a metal, coupled to a propagating electromagnetic field. They exist at interfaces between a dielectric and a conductor. The SPP amplitude decays exponentially with increasing distance perpendicular to the interface. Hence, SPPs are surface electromagnetic waves having an electromagnetic field confined to the close proximity of the metal-dielectric interface. This leads to a strong field enhancement at the interface, making SPPs extraordinarily sensitive to the surface quality.

SPP excitation at metal-dielectric interfaces and the according dispersion relation are discussed theoretically and experimentally already in many reviews [6–8, 14]. This chapter theoretically introduces into SPP excitation and derivation of propagating wave solutions. Starting point are the macroscopic Maxwell's equations in matter leading to the Helmholtz equation, the special form of the wave equation allowing separation of variables to reduce the complexity of the system of coupled differential equations. Appropriate boundary conditions deliver the propagating wave solutions. Considering a finite metal film, SPP excitation at each interface has to be considered which results in the long- and short-range SPP mode. This is briefly introduced in chapter 2.2. The derivation of SPP dispersion relations is adopted from [6]. Furthermore in this chapter, different techniques for SPP excitation are introduced.

2.1 ELECTRODYNAMICS AT INTERFACES

The Helmholtz equation is one form of the fundamental wave equation in electrodynamics describing wave propagation at material interfaces. As all electrodynamic phenomena, the Helmholtz equation is derived by using the four macroscopic Maxwell equations in matter [6]:

1. Gauss' law

$$\nabla \cdot \mathbf{D} = \rho_{\text{ext}} \quad (2.1a)$$

2. Gauss' law for magnetism

$$\nabla \cdot \mathbf{B} = 0 \quad (2.1b)$$

3. Faraday's law of induction

$$\nabla \times \mathbf{E} = -\frac{\partial \mathbf{B}}{\partial t} \quad (2.1c)$$

4. Ampère's law

$$\nabla \times \mathbf{H} = \mathbf{J}_{\text{ext}} + \frac{\partial \mathbf{D}}{\partial t} \quad (2.1d)$$

The Maxwell's equations interconnect the four macroscopic vector fields. \mathbf{D} is the dielectric displacement, \mathbf{E} is the electric field, \mathbf{H} is the magnetic field and \mathbf{B} is the magnetic induction. The external charge density ρ_{ext} and the external current density \mathbf{J}_{ext} are the sources of these fields.

Furthermore in matter, the four electromagnetic fields are linked to the polarization \mathbf{P} and the magnetization \mathbf{M} via the constitutive relations:

$$\mathbf{D} = \epsilon_0 \mathbf{E} + \mathbf{P} \quad (2.2a)$$

$$\mathbf{B} = \mu_0 (\mathbf{H} + \mathbf{M}), \quad (2.2b)$$

where ϵ_0 is the electric permittivity in vacuum and μ_0 is the magnetic permeability in vacuum. Provided that all materials within this work are linear, isotropic and nonmagnetic, the constitutive relations simplify to:

$$\mathbf{D} = \epsilon_0 \epsilon \mathbf{E} \quad (2.3a)$$

$$\mathbf{B} = \mu_0 \mu \mathbf{H}. \quad (2.3b)$$

ϵ is the relative permittivity and μ is the relative permeability, which equals 1 for nonmagnetic media.

To describe the properties of SPPs, Maxwell's equations need to be transformed into a general form applicable to the flat interface between a metal and a dielectric, which is the wave equation. Considering no external stimuli, the curl equations (2.1c) and (2.1d) are combined to the following relation:

$$\nabla \times \nabla \times \mathbf{E} = -\mu_0 \frac{\partial^2 \mathbf{D}}{\partial t^2}. \quad (2.4)$$

Transcribing equation (2.4) by using the vector analytical identities $\nabla \times \nabla \times \mathbf{E} \equiv \nabla (\nabla \cdot \mathbf{E}) - \nabla^2 \mathbf{E}$ and $\nabla \cdot (\epsilon \mathbf{E}) \equiv \mathbf{E} \cdot \nabla \epsilon + \epsilon \nabla \cdot \mathbf{E}$ leads to

$$\nabla \left(-\frac{1}{\epsilon} \mathbf{E} \cdot \nabla \epsilon \right) - \nabla^2 \mathbf{E} = -\mu_0 \epsilon_0 \epsilon \frac{\partial^2 \mathbf{E}}{\partial t^2}. \quad (2.5)$$

Equation (2.5) becomes the central equation of electromagnetic wave theory by considering negligible variations of the dielectric profile $\epsilon = \epsilon(\mathbf{r})$ within distances of one optical wavelength:

$$\nabla^2 \mathbf{E} - \frac{\epsilon}{c^2} \frac{\partial^2 \mathbf{E}}{\partial t^2} = 0, \quad (2.6)$$

where $c = 1/\sqrt{\epsilon_0 \mu_0}$ is the velocity of light in free space.

To obtain a description of confined propagating modes, harmonic time dependency of the electric field $\mathbf{E}(\mathbf{r}, t) = \mathbf{E}(\mathbf{r}) e^{-i\omega t}$ has to be assumed. This, inserted into equation (2.6), leads to a time-independent form of the wave equation:

$$\nabla^2 \mathbf{E} + k_0^2 \epsilon \mathbf{E} = 0, \quad (2.7)$$

$k_0 = \omega/c$ is the wave vector of a propagating wave in vacuum. Equation (2.7) is the desired form of the wave equation, which is called Helmholtz equation.

To evaluate the SPP solutions, an appropriate propagation geometry has to be specified. In figure 2.1, a schematic metal slab is illustrated and a Cartesian coordinate system defines the spacial directions. The x -direction is marked in red, indicating the SPP propagation direction and furthermore, SPPs should exhibit no spacial variation in y -direction. Here, the surface plane is defined as the $z = 0$ plane, containing the propagating SPP waves. Using these specifications, the propagating wave can now be described via $\mathbf{E}(x, y, z) = \mathbf{E}(z) e^{i\beta x}$. β is the complex propagation constant and correlates to the wave vector component k_x in propagation direction. Insert the expression for propagating waves into (2.7), produces the suitable wave equation for the electric field:

$$\frac{\partial^2 \mathbf{E}(z)}{\partial z^2} + (k_0^2 \epsilon - \beta^2) \mathbf{E} = 0 \quad (2.8)$$

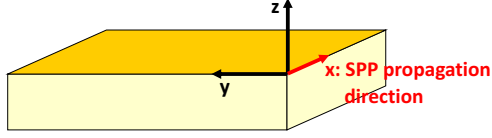


Figure 2.1.: Schematic of a planar waveguide, defining the x-direction, labeled in red, as SPP propagation direction.

For the magnetic field, a corresponding wave equation exists.

To determine the dispersion relation and the spacial field profile, explicit expressions for the field components of the electric and the magnetic field are needed. This is done by using the curl equations (2.1c) and (2.1d) and considering $\partial/\partial t = -i\omega$ for harmonic time-dependence:

$$\frac{\partial E_z}{\partial y} - \frac{\partial E_y}{\partial z} = i\omega\mu_0 H_x \quad (2.9a)$$

$$\frac{\partial E_x}{\partial z} - \frac{\partial E_z}{\partial x} = i\omega\mu_0 H_y \quad (2.9b)$$

$$\frac{\partial E_y}{\partial x} - \frac{\partial E_x}{\partial y} = i\omega\mu_0 H_z \quad (2.9c)$$

$$\frac{\partial H_z}{\partial y} - \frac{\partial H_y}{\partial z} = -i\omega\epsilon\epsilon_0 E_x \quad (2.9d)$$

$$\frac{\partial H_x}{\partial z} - \frac{\partial H_z}{\partial x} = -i\omega\epsilon\epsilon_0 E_y \quad (2.9e)$$

$$\frac{\partial H_y}{\partial x} - \frac{\partial H_x}{\partial y} = -i\omega\epsilon\epsilon_0 E_z \quad (2.9f)$$

This system of equations simplifies for propagation in x-direction, which means $\partial/\partial x = i\beta$ and homogeneity in y-direction, implying $\partial/\partial y = 0$:

$$\frac{\partial E_y}{\partial z} = -i\omega\mu_0 H_x \quad (2.10a)$$

$$\frac{\partial E_x}{\partial z} - i\beta E_z = i\omega\mu_0 H_y \quad (2.10b)$$

$$i\beta E_y = i\omega\mu_0 H_z \quad (2.10c)$$

$$\frac{\partial H_y}{\partial z} = i\omega\epsilon\epsilon_0 E_x \quad (2.10d)$$

$$\frac{\partial H_x}{\partial z} - i\beta H_z = -i\omega\epsilon\epsilon_0 E_y \quad (2.10e)$$

$$i\beta H_y = -i\omega\epsilon\epsilon_0 E_z \quad (2.10f)$$

This system of equation has two self-consistent sets of solutions, leading to different polarization states of the waves solutions. Transverse magnetic (TM) modes have non-zero E_x -, E_z -, and H_y -components, while in the transverse electric (TE) solution the H_x -, H_z -, and E_y -components are unequal to zero.

Considering this, the wave equation for TM modes becomes:

$$\frac{\partial^2 H_y}{\partial z^2} + \left(k_0^2 \epsilon - \beta^2\right) H_y = 0. \quad (2.11a)$$

And the corresponding system of equations (2.10a) to (2.10f) results in:

$$E_x = -i \frac{1}{\omega \epsilon \epsilon_0} \frac{\partial H_y}{\partial z} \quad (2.11b)$$

$$E_z = -\frac{\beta}{\omega \epsilon \epsilon_0} H_y. \quad (2.11c)$$

Furthermore, the wave equation for TE modes becomes:

$$\frac{\partial^2 E_y}{\partial z^2} + (k_0^2 \epsilon - \beta^2) E_y = 0, \quad (2.12a)$$

and the governing equations are:

$$H_x = i \frac{1}{\omega \mu_0} \frac{\partial E_y}{\partial z} \quad (2.12b)$$

$$H_z = \frac{\beta}{\omega \mu_0} E_y. \quad (2.12c)$$

These equations are initial point for the following discussion on surface plasmon polaritons.

2.2 SURFACE PLASMON POLARITONS AT METAL-DIELECTRIC INTERFACES

SPPs occur at metal-dielectric interfaces. A schematic illustration is shown in figure 2.2.

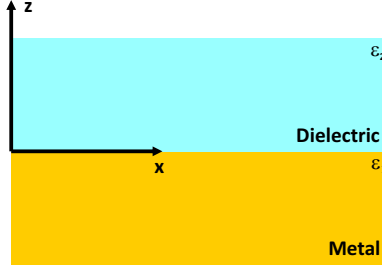


Figure 2.2.: Metal-dielectric interface which supports SPP propagation. SPP propagation takes place in x-direction.

This means, the $z > 0$ half space is filled with dielectric material, having a positive and real dielectric constant ϵ_2 . The adjacent metallic half space $z < 0$ exhibits a complex dielectric function $\epsilon_1(\omega)$. For metals, $\text{Re}[\epsilon_1] < 0$ is required.

First, TE wave solutions are considered. Equations (2.12a) to (2.12c) produce expressions of the field components for the dielectric half space $z > 0$:

$$E_y(z) = A_2 e^{i\beta x} e^{-k_2 z} \quad (2.13a)$$

$$H_x(z) = -iA_2 \frac{1}{\omega\mu_0} k_2 e^{i\beta x} e^{-k_2 z} \quad (2.13b)$$

$$H_z(z) = A_2 \frac{\beta}{\omega\mu_0} e^{i\beta x} e^{-k_2 z} \quad (2.13c)$$

For the metallic half space $z < 0$, the following set of field components applies:

$$E_y(z) = A_1 e^{i\beta x} e^{k_1 z} \quad (2.14a)$$

$$H_x(z) = iA_1 \frac{1}{\omega\mu_0} k_1 e^{i\beta x} e^{k_1 z} \quad (2.14b)$$

$$H_z(z) = A_1 \frac{\beta}{\omega\mu_0} e^{i\beta x} e^{k_1 z} \quad (2.14c)$$

Wave vectors $k_{1,2}z$ represent the component of the wave vector perpendicular to the interface. The reciprocal value $\hat{z} = 1/|k_z|$ defines the evanescent decay length of the fields perpendicular to the interface.

Continuity of E_y and H_x at the interface requires the boundary condition:

$$A_1 (k_1 + k_2) = 0 \quad (2.15)$$

Confinement to the interface requires $\text{Re}[k_1] > 0$ and $\text{Re}[k_2] > 0$, which is fulfilled if $A_1 = 0$. Therefore, it is $A_1 = A_2 = 0$. This leads to the conclusion that no TE surface modes exist and that SPP excitation is possible only for TM modes.

TM solutions are gained from equations (2.11a) to (2.11c) for the dielectric half space $z > 0$:

$$H_y(z) = A_2 e^{i\beta x} e^{-k_2 z} \quad (2.16a)$$

$$E_x(z) = iA_2 \frac{1}{\omega \epsilon_0 \epsilon_2} k_2 e^{i\beta x} e^{-k_2 z} \quad (2.16b)$$

$$E_z(z) = -A_2 \frac{\beta}{\omega \epsilon_0 \epsilon_2} e^{i\beta x} e^{-k_2 z} \quad (2.16c)$$

For the metallic half space $z < 0$ the following set of solutions apply:

$$H_y(z) = A_1 e^{i\beta x} e^{k_1 z} \quad (2.17a)$$

$$E_x(z) = -iA_1 \frac{1}{\omega \epsilon_0 \epsilon_1} k_1 e^{i\beta x} e^{k_1 z} \quad (2.17b)$$

$$E_z(z) = -A_1 \frac{\beta}{\omega \epsilon_0 \epsilon_1} e^{i\beta x} e^{k_1 z} \quad (2.17c)$$

Continuity of H_y and $\epsilon_{1/2} E_z$ at the interface requires $A_1 = A_2$ and

$$\frac{k_2}{k_1} = -\frac{\epsilon_2}{\epsilon_1} \quad (2.18)$$

As SPP waves only exist at material interfaces with opposite signs of the real part of their dielectric permittivities. Therefore, $\text{Re}[\epsilon_1] < 0$ and $\epsilon_2 > 0$ has to apply. This is the case between a metal and an insulator.

Furthermore, the expression for H_y has to fulfill equation (2.11a), which yields

$$k_1^2 = \beta^2 - k_0^2 \epsilon_1 \quad (2.19a)$$

$$k_2^2 = \beta^2 - k_0^2 \epsilon_2 \quad (2.19b)$$

Equations (2.19a) and (2.19b) combined with (2.18) results in the dispersion relation of SPPs propagating along metal-dielectric interfaces:

$$\beta = k_0 \sqrt{\frac{\epsilon_1 \epsilon_2}{\epsilon_1 + \epsilon_2}} \quad (2.20)$$

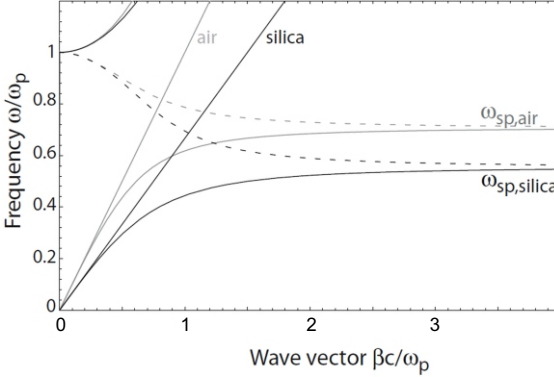


Figure 2.3.: SPP dispersion relation of a single metal-dielectric interface. The gray curves show the metal-air dispersion relation and the black curves illustrate the metal-silica dispersion relation, assuming a perfect conductor as metal. The dashed curves are the imaginary parts, respectively. The image is taken from reference [6].

Figure 2.3 illustrates dispersion relation plots from equation (2.20) at single metal-dielectric interfaces. Assuming a metal without damping, the SPP dispersion relation is considered for a metal-air and a metal-silica interface and plotted as a gray and

a black curve, respectively. The dashed curves represent both dispersion relation imaginary parts. Due to the bound nature of SPPs, excitation is possible only for wave vectors lying on the right side of the light lines of air and silica. Therefore, phase-matching techniques are necessary for SPP excitation with light beams.

Furthermore, equation (2.20) allows calculation of the characteristic surface plasmon polariton frequency ω_{SPP} by using the free-electron dielectric function $\epsilon_1(\omega) = 1 - \omega_p^2 / (\omega^2 + i\gamma\omega)$ of an idealized metal:

$$\omega_{\text{SPP}} = \frac{\omega_p}{\sqrt{1 + \epsilon_2}}. \quad (2.21)$$

$\omega_p^2 = ne^2/\epsilon_0 m$ is the plasma frequency of the free electron gas and γ is a characteristic collision frequency.

In multilayer systems, several interfaces between different materials have to be considered. In figure 2.4, a three layer system is illustrated and in the following, the lowest-order bound SPP modes for TM polarization are derived for such systems.

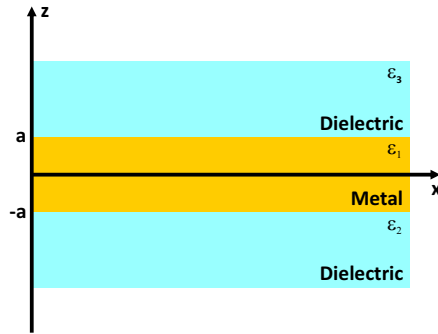


Figure 2.4.: In multilayer systems, SPPs exist at each material interface.

The field components for $z > a$ acquire the following form:

$$H_y = Ae^{i\beta x} e^{-k_3 z} \quad (2.22a)$$

$$E_x = iA \frac{1}{\omega \epsilon_0 \epsilon_3} k_3 e^{i\beta x} e^{-k_3 z} \quad (2.22b)$$

$$E_z = -A \frac{\beta}{\omega \epsilon_0 \epsilon_3} e^{i\beta x} e^{-k_3 z}. \quad (2.22c)$$

For $z < -a$, the following field components are required:

$$H_y = Be^{i\beta x} e^{k_2 z} \quad (2.23a)$$

$$E_x = -iB \frac{1}{\omega \epsilon_0 \epsilon_2} k_2 e^{i\beta x} e^{k_2 z} \quad (2.23b)$$

$$E_z = -B \frac{\beta}{\omega \epsilon_0 \epsilon_2} e^{i\beta x} e^{k_2 z}. \quad (2.23c)$$

The SPP fields should decay exponentially into layer 2 and 3. The component of the wave vector perpendicular to the interfaces is $k_i \equiv k_i z$.

Within the core region 1, which is $-a < z < a$, the modes localized at the top and the bottom interface couple with each other. Therefore the field components become:

$$H_y = Ce^{i\beta x} e^{k_1 z} + De^{i\beta x} e^{-k_1 z} \quad (2.24a)$$

$$E_x = -iC \frac{1}{\omega \epsilon_0 \epsilon_1} k_1 e^{i\beta x} e^{k_1 z} + iD \frac{1}{\omega \epsilon_0 \epsilon_1} k_1 e^{i\beta x} e^{-k_1 z} \quad (2.24b)$$

$$E_z = C \frac{\beta}{\omega \epsilon_0 \epsilon_1} e^{i\beta x} e^{k_1 z} + D \frac{\beta}{\omega \epsilon_0 \epsilon_1} e^{i\beta x} e^{-k_1 z} \quad (2.24c)$$

Again, continuity of H_y and E_x is required and leads to the following conditions at $z = a$:

$$Ae^{-k_3 a} = Ce^{k_1 a} + De^{-k_1 a} \quad (2.25a)$$

$$\frac{A}{\epsilon_3} k_3 e^{-k_3 a} = -\frac{C}{\epsilon_1} k_1 e^{k_1 a} + \frac{D}{\epsilon_1} k_1 e^{-k_1 a} \quad (2.25b)$$

and at $z = -a$:

$$Be^{-k_2 a} = Ce^{-k_1 a} + De^{k_1 a} \quad (2.26a)$$

$$-\frac{B}{\epsilon_2} k_2 e^{-k_2 a} = -\frac{C}{\epsilon_1} k_1 e^{-k_1 a} + \frac{D}{\epsilon_1} k_1 e^{k_1 a}, \quad (2.26b)$$

which is a linear system of four coupled equations. Furthermore, H_y has to fulfill the wave equation (2.11a) in the three different regions, leading to the condition:

$$k_i^2 = \beta^2 - k_0^2 \epsilon_i, \quad (2.27)$$

where $i = 1, 2, 3$.

Solution of this system of linear equations is an implicit expression for the dispersion relation linking β and ω :

$$e^{-4k_1 a} = \frac{k_1/\epsilon_1 + k_2/\epsilon_2}{k_1/\epsilon_1 - k_2/\epsilon_2} \frac{k_1/\epsilon_1 + k_3/\epsilon_3}{k_1/\epsilon_1 - k_3/\epsilon_3} \quad (2.28)$$

However, for infinite thickness, (2.28) reduces to (2.18), which gives the dispersion relation of two uncoupled SPPs at the particular interface.

Assuming the material in region 2 and region 3 being the same, $\epsilon_2 = \epsilon_3$ and therefore $k_2 = k_3$, the dispersion relation from equation (2.28) splits up into two parts:

$$\tanh k_1 a = -\frac{k_2 \epsilon_1}{k_1 \epsilon_2} \quad (2.29a)$$

$$\tanh k_1 a = -\frac{k_1 \epsilon_2}{k_2 \epsilon_1} \quad (2.29b)$$

Equation (2.29a) describes modes of odd vector parity. This means, $E_x(z)$ is odd while $H_y(z)$ and $E_z(z)$ are even functions. On the other hand, equation (2.29b) modes of even vector parity. Here, $E_x(z)$ is an even function whereas $H_y(z)$ and $E_z(z)$ are odd.

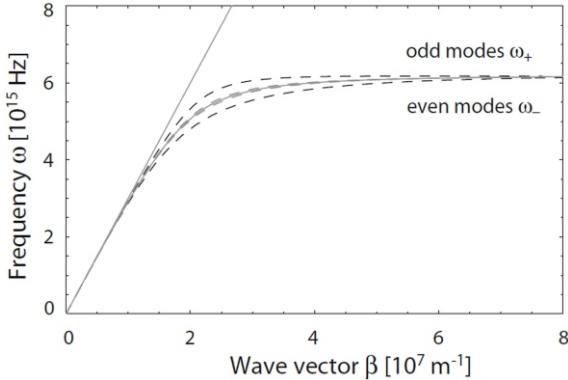


Figure 2.5.: Dispersion relation of the two coupled modes ω_+ and ω_- for an air-silver-air multilayer system. The dashed gray curves represent a 100 nm thick silver film and the dashed black curves are from a 50 nm thick silver film. The continuous gray line comes from a single silver-air interface. The image is taken from reference [6].

In figure 2.5, the dispersion relation of an air-silver-air system is plotted according to equations (2.29a) and (2.29b). The dashed black curves represent a 50 nm thick silver film and clearly show

the splitting into an coupled odd- and even mode. For comparison, the continuous gray curve represents the dispersion relation of a single silver-air interface.

Approximating the silver dielectric function $\epsilon_1(\omega)$ via the Drude model [5, 6], odd and even modes can be derived from equations (2.29a) and (2.29b):

$$\omega_+ = \frac{\omega_p}{\sqrt{1 + \epsilon_2}} \sqrt{1 + \frac{2\epsilon_2 e^{-2\beta a}}{1 + \epsilon_2}} \quad (2.30a)$$

$$\omega_- = \frac{\omega_p}{\sqrt{1 + \epsilon_2}} \sqrt{1 - \frac{2\epsilon_2 e^{-2\beta a}}{1 + \epsilon_2}} \quad (2.30b)$$

These two coupled modes exhibit opposite behavior. Considering real, absorptive metals, the confinement to the metal decreases as the film thickness decreases. Therefore, the propagation length of odd modes increases drastically, which ascribes the name long-range SPP. Even modes are defined as short-range SPPs, as their confinement to the metal increases for a decreasing metal thickness and therefore have decreased propagation length [15].

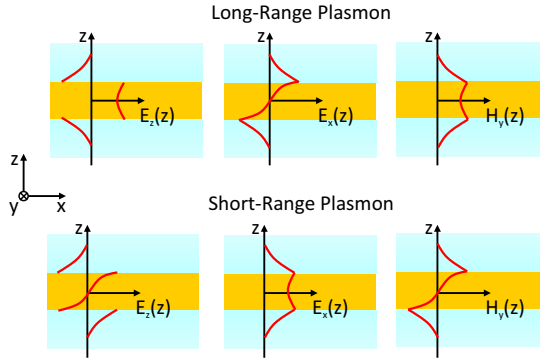


Figure 2.6.: Schematic mode structure of long- and short-range SPPs, representing all field components for the TM-polarization state.

Figure 2.6 schematically depicts the field distributions of the E_x -, E_z -, and H_y -components for long- and short-range SPPs [16] within a thin metal film, surrounded by a dielectric. The E_x - and H_y -component for long-range SPPs have symmetric field distribution, while for short-range SPPs, antisymmetric behavior is attributed to these field components. For both modes, the evanescent fields penetrate into the metal film. It is shown in [15], that long-range SPPs have a considerably smaller fraction of fields inside the metal and therefore have a propagation length which is much longer.

2.3 DISPERSION RELATION OF SURFACE PLASMON POLARITONS AT VACUUM-GOLD-SILICON INTERFACES

For many decades, SPP excitations at both interfaces of a thin metal film, which is surrounded by a dielectric, are investigated experimentally and theoretically [15, 17–23]. In essence, at thick metal films SPP waves propagate at each interface. Both modes exhibit the same wavelength and cannot couple due to the thickness of the metal film. Assuming a sufficient thin metal film, the two SPP waves couple and split into two modes. The first SPP mode possesses a longer wavelength, while the second one has a short wavelength. The experiment, introduced within this work, consists of a completely asymmetric system, which has a gold-vacuum- and a gold-silicon interface. As silicon is a high refractive index material in the visible region, the dispersion relation experience extreme flattening and additional wavelength reduction should occur for excited SPPs. In this section, dispersion relations are calculated numerically for SPPs at gold-vacuum- and gold-silicon interfaces, meaning $\epsilon_2 \neq \epsilon_3$. Therefore, suitable material parameters are applied to equations (2.29a) and (2.29b).

A 20 nm thick layer of Johnson-Christy [24] gold is assumed to be directly attached on top of a silicon substrate, which is covered with the 2.5 nm thick layer of native oxide. To calculate the dispersion relations for long range (LR) SPPs at the gold-vacuum interface and short range (SR) SPPs at the gold-silicon interface,

analytical equations for complex propagation constants along interfaces have to be solved¹. The results are shown in figure 2.7 (A), where the excitation energy is plotted over the x-component of the wave vector k_x . The blue curve in figure 2.7 (A) is the calculated dispersion relation for LR SPPs propagating at the gold-vacuum interface. This coincides with the vacuum cone, representing the propagation of light in free space. Hence, the LR SPP wavelength should not differ markedly from the excitation wavelength. SPP propagation in the bulk silicon substrate is described by the silicon cone. The red curve represents the dispersion relation of propagating SR SPPs at the gold-silicon interface. From these dispersion relations, characteristics of the expected SPP excitations are determined.

In the two-photon photoemission (2PPE) photoemission electron microscopy (PEEM) experiment, the excitation laser source has a central wavelength of $\lambda_0 = 800$ nm, which is illustrated in figure 2.7 (A) as horizontally dashed black line. From the intersection points with the dispersion relation curves, LR- and SR SPP wavelengths are calculated: $\lambda_{\text{LR-SPP}} = 787$ nm and $\lambda_{\text{SR-SPP}} = 176$ nm. Furthermore, propagation lengths for LR- and SR SPPs are 3.6 μm and 1.12 μm , respectively. The phase velocity of the two SPPs are 0.983 c and 0.221 c expressed in unities of the velocity of light.

Considering higher excitation energies or smaller excitation wavelengths respectively, a wave vector maximum of 80 $1/\mu\text{m}$ is obtained at about 500 nm excitation wavelength. This means further reduction of the SR SPP wavelength should be possible, down to a minimum of 90 nm.

In 2PPE PEEM, SPP waves are accompanied by the x-component of an electric field [25]. Figure 2.7 (b) illustrates a cross-section through the sample, represented by the material sequence vacuum, gold and native silicon dioxide on top of the bulk silicon substrate. The E_x -field distribution for LR SPPs in (i) and SR SPP in (ii) is overlaid, red indicates maximum field intensity, while blue implies field minima. The field distributions show that the

¹ Thomas Weiss, 4th Physics Institute, University of Stuttgart

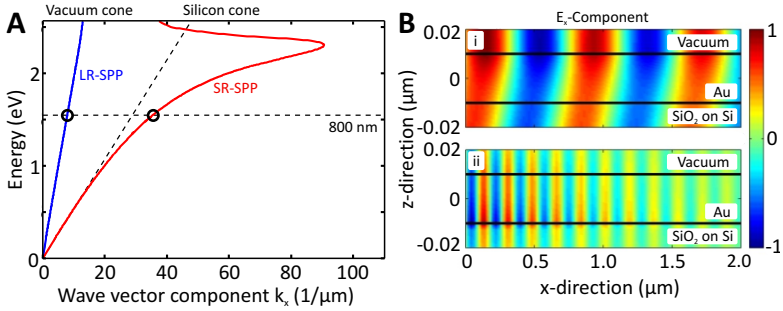


Figure 2.7.: (A) Dispersion diagram of LR- (blue) and SR SPPs (red), excited on a 20 nm thick film of Johnson-Christy gold on an atomically flat silicon substrate, covered with a 2.5 nm thick native oxide layer. Considering $\lambda_0 = 800$ nm (dashed black line) as excitation wavelength, LR- and SR SPP wavelength are calculated from the cross-section points, which are marked with black circles: $\lambda_{\text{LR-SPP}} = 787$ nm and $\lambda_{\text{SR-SPP}} = 176$ nm. (B) Cross-section through the sample, superposed with the x-component of the electric field vector propagating in x-direction. Image (i) shows LR SPPs, being predominantly located at the gold-vacuum interface. Image (ii) illustrates SR SPPs, primarily existing at the gold-silicon interface. From this plot, the SR SPP wavelength can be roughly estimated to 180 nm. Furthermore, field plot (ii) confirms SR SPPs decaying after a few micrometer of propagation.

LR SPP in (i) is mainly located at the gold-vacuum interface and propagates over several micrometers. The SR SPP however, predominantly exists at the gold-silicon interface and decays after roughly 1 μm of propagation.

2.4 EXCITATION OF SURFACE PLASMON POLARITONS

Besides SPP excitation due to impact of charged particles like electrons, straightforward SPP stimulation by light is not possible, because the SPP dispersion relation curve is located to the right side of the light line. Therefore, special phase-matching techniques are necessary for SPP excitation and therefore briefly introduced within this chapter.

2.4.1 *Excitation with Electrons*

Ritchie [26] utilized loss spectra of low-energy electron beams, performing experiments at thin metal foils. Besides the excitation of volume plasmons of energy $\hbar\omega_p$, he assumed an extra energy loss at $\hbar\omega_p/2$, called the low-lying energy loss.

This low-lying energy loss was determined experimentally over the following years [27, 28] by the energy loss spectra of aluminum and magnesium films. It was ascribed to an electromagnetic excitation at a metal-air surface, corresponding to the surface plasmon polariton.

Further theoretical considerations by Stern and Ferrell [29] confirmed the dispersion relation of SPPs and furthermore, its splitting into odd and even coupled modes as shown in equations (2.29a) and (2.29b).

Finally, Vincent and Silcox [30] were able to determine the complete SPP dispersion relation via analysis of the change in energy and momentum of fast electrons transmitted through thin metal films.

2.4.2 *Excitation with Light*

It is impossible to directly excite SPPs on a metal-dielectric interface by light, because of $\beta > k$. β is the SPP propagation constant and k is the wave vector of the incident light. This implies, that a momentum projection of photons, impinging under an angle θ to the surface normal, $k_x = k \sin \theta$ onto the interface is always

smaller than the SPP propagation constant β , even at grazing incidence. This condition prohibits phase-matching and therefore SPP excitation.

Therefore, phase-matching has to be realized artificially. For example by a three-layer system, which is composed of a thin metal film surrounded by two different dielectrics. One of the dielectrics is supposed to be air ($\epsilon = 1$). Usually, the insulator of higher dielectric constant ϵ is a prism, see figure 2.9. A light beam reflected at the interface between the prism and the metal film, therefore has an in-plane momentum of $k_x = k\sqrt{\epsilon} \sin \theta$. This is condition allows SPP excitation at the interface between the low-index dielectric and the metal film.

Therefore, the SPP propagation constant β has to be located between the light lines of air and the dielectric material, see figure 2.8. SPP excitation influences the reflected beam intensity by exhibiting a minimum. However, SPP excitation at the metal-prism interface is not possible, because the respective SPP dispersion relation lies outside the prism light cone. This principle is known as attenuated total internal reflection.

There are two different coupling geometries for SPP excitation. Both principles involve tunneling of the excitation beam electro-

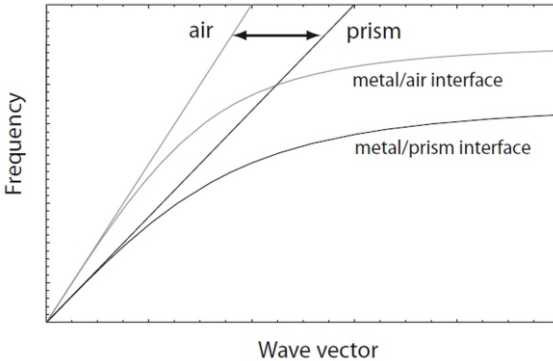


Figure 2.8.: Prism coupling is possible for SPP wave vectors lying in between the prism light cone and the air light cone. The image is taken from reference [6].

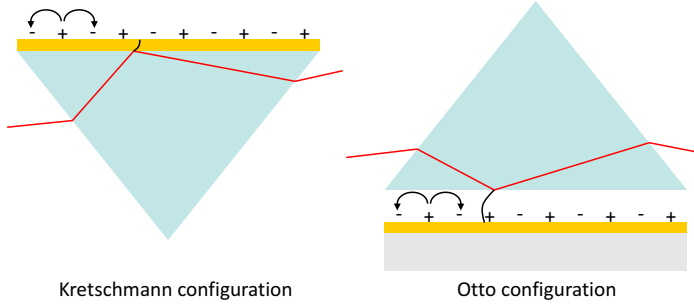


Figure 2.9.: SPP excitation by means of prism coupling in the Kretschmann configuration on the left side and the Otto configuration in the right image.

magnetic to the metal-air interface, where SPP excitation is possible. The left picture of figure 2.9 illustrates the most common configuration, which is the Kretschmann method [31]. Here, a thin metal film is evaporated onto a glass prism. Light from the incident beam impinges from the glass side at an angle that is greater than the critical angle for total internal reflection. Such configuration allows photons to tunnel through the metal film and excitation of SPPs at the metal air interface.

The second possibility is known as Otto configuration [32] and is illustrated in the right image of figure 2.9. Here, the prism is separated from the metal film by a small air gap. Total internal reflection can occur at the prism-air interface and SPPs are excited due to tunneling to the metal-air interface. The Otto configuration is preferred to avoid direct sample contact, for example during surface quality studies.

Coupling via grating is a second approach to overcome the wave vector mismatch between the in-plane component of the impinging photons $k_x = k \sin \theta$ and the SPP propagation constant β . For that purpose, the metal film is structured with a grating of period a . This requires the following phase matching condition:

$$\beta = k \sin \theta \pm \nu g \quad (2.31)$$

$\nu = 2\pi/a$ is the reciprocal vector of the grating and furthermore, ν has to be integer. Here as well, excitation of SPPs is detected as minimum of the reflected light intensity.

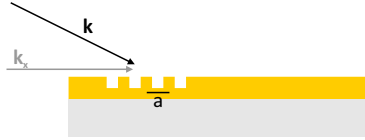


Figure 2.10.: SPP excitation on a thin metal film via phase matching of light using a periodic grating.

Within this work, SPP excitation is performed via normal incidence two-photon photoemission microscopy on single crystalline gold platelets, directly attached on silicon substrates. Here, the wave vector mismatch is overcome due to the sharp, single crystalline edges of the platelet and normal incident laser pulses.

THE PLASMONIC ANGULAR ORBITAL MOMENTUM

Surface plasmon polaritons are an exciting field for light-matter interaction. The main hurdle is the momentum mismatch between SPPs and a free-space light field, however, multiple schemes for overcoming this have been established. One particularly intriguing example is the transfer of orbital momentum from circularly polarized light to a plasmonic system. This chapter introduces the concept of orbital momentum of light and shows the first example of rotational light beams coupling to surface plasmon polaritons.

3.1 THE ANGULAR ORBITAL MOMENTUM OF LIGHT

Usually, light carries linear momentum of $\hbar k_0$ per photon. However, due to specific polarization states, it can also possess angular momentum. For example, spin angular momentum (SAM) is ascribed to circularly polarized light due to rotation of the electric and the magnetic field vectors. Furthermore, interaction with specific materials results in orbital angular momentum (OAM) [33–35] of light, exhibiting propagating helical phase fronts.

In 1909, Poynting [36] theoretically predicted light beams with SAM. In 1936, Beth [37] successfully detected and measured light angular momentum mechanically.

The SAM of $\pm\hbar$ per photon is attributed to circular polarization states of the light. It is oriented parallel to the propagation direction of the light beam and determined by the polarization helicity σ , which describes the degree of circular polarization. It takes the value of ± 1 for right- and left-hand circularly polarized light, respectively, and is defined from the point of view of the source.

Allen [38] ascribed OAM as natural property to all helically phased

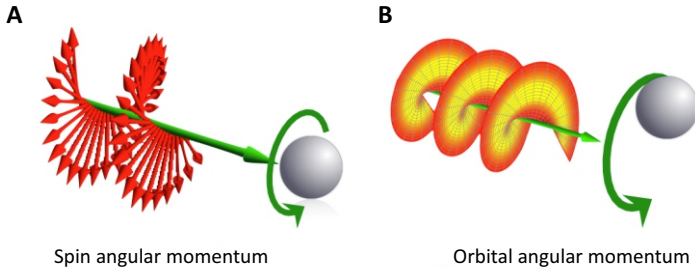


Figure 3.1.: (A) Circularly polarized light carries SAM according to the rotation direction of the electric field vector. (B) Helical light beams have OAM. This image is taken from E-karimi (Own work) [CC BY-SA 3.0 (<http://creativecommons.org/licenses/by-sa/3.0>)], via Wikimedia Commons.

light beams. The OAM can be characterized as azimuthal phase dependence $\exp(il\phi)$ of the light beam, where ϕ is the angular coordinate and l is the topological charge, describing the phase increment around the vortex core. It can have any positive or negative integer value, leading to helical phase fronts of such beams. The number of inter-wound helices and the handedness depend on magnitude and sign of l . Figure 3.1 schematically illustrates these two angular momenta of light. In (A), the SAM of a circularly polarized light beam is illustrated by rotating the electric field vector around the propagation axis. (B) represents the OAM of light. Here, the phase fronts screw in a helical fashion in propagation direction. Both SAM and OAM can be transferred to matter, respectively.

The energy of each photon is $\hbar\omega$, directly leads to the corresponding energy expressions for the orbital angular momentum, which is $l\hbar$, and the spin angular momentum of $\sigma\hbar$, respectively.

Crucial point within this chapter is, the transfer of angular momentum to microscopic particles due to absorption, leading to a rotational motion of the particle. For a beam carrying SAM the object will rotate around its own axis, while a beam carrying

OAM will lead to a rotation of the particle around the beam axis.

Optical tweezers are a well known example of such particle light interaction. Here, a microscopic object is trapped within a tightly focused, either circularly polarized or helical light beam. These beams force the particle either to a spin or a torque movement, respectively.

3.2 PLASMON VORTICES

Pioneering work was done by Erez Hasman [39] in 2008, which was followed by several others [40–45]. Here, near field optical techniques in combination with circularly polarized light are utilized for SPP excitation on helical shaped slits in metal films. The angular momentum from the circularly polarized light field impinging on the structure, is transferred to the excited surface plasmon polaritons and a helically shaped plasmon pattern forms. Their fundamental results are summarized in figure 3.2 (A) and (B), which compare the SPP near fields excited via right hand circularly polarized (RCP) light and left hand circularly polarized (LCP) light. Illumination with LCP light is characterized by helicity $\sigma = -1$ and RCP light by $\sigma = +1$. Excitation with $\sigma = -1$ polarized light yields a bright maximum in the central region of the structure, while illumination with $\sigma = +1$ light generates a field minimum.

This polarization dependent near-field intensity distribution is caused by the phase of the excited SPP mode. The phase images are plotted in figure 3.2 (C) and (D). From geometrical considerations it is shown that this phase difference is caused by the helical spiral structure.

Using near field optical techniques, the SPP electric field profile in z-direction is investigated and the SPP vortex is considered to be located in the metal-dielectric interface in the x-y plane. Mathematically, the SPP electric field of the spiral plasmon modes can be described by the l^{th} order Bessel function:

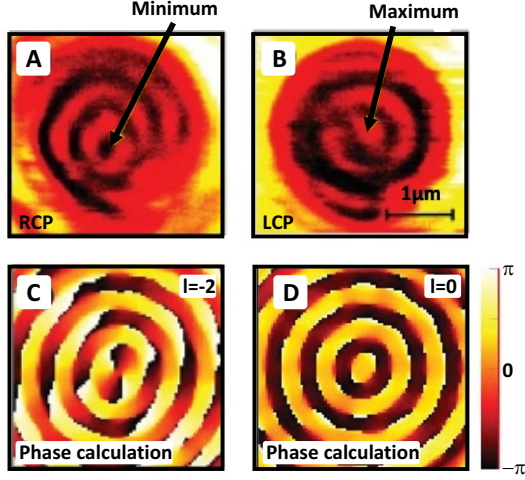


Figure 3.2.: (A) and (B) show near field images from [39], representing a minimum for SPP excitation with RCP and a maximum for LCP excitation. (C) and (D) reveal phase calculations yielding the topological charge of the structure. Images are taken from [39].

$$E_{l,p}(\phi, r) = E_0 \exp(ik_z z) [\exp(il\phi)] J_l(k_p r) \hat{z}. \quad (3.1)$$

Here, k_z is the wavenumber perpendicular to the surface and k_p is the radial wave number. l is the topological charge, r , z and ϕ is the cylindrical coordinate set and E_0 is a constant. $\exp(il\phi)$ is a spiral mode, with ϕ corresponding to the azimuthal angle.

Furthermore, it is shown in [39] that the total topological charge of a spiral mode is $l = -(\sigma_{\pm} + m)$, where m is the geometrical charge or the pitch of the spiral structure. For $m = 1$ the spiral mode has the form $J_0(k_p r)$ for $\sigma = -1$ and $\exp(-i2\phi)J_2(k_p r)$ for $\sigma = +1$ illumination.

The plasmonic modes occurring in this experiment are dominated by Bessel functions. In figure 3.3, the 0th- and the 2nd order Bessel functions, J_0 and J_2 , are plotted in 2D (A) and 3D (B). The 2D plots illustrate the field profiles. J_0 , which is described by the blue curve, has a global maximum at zero position. The red curve describes the J_2 Bessel function, with a minimum in

the center.

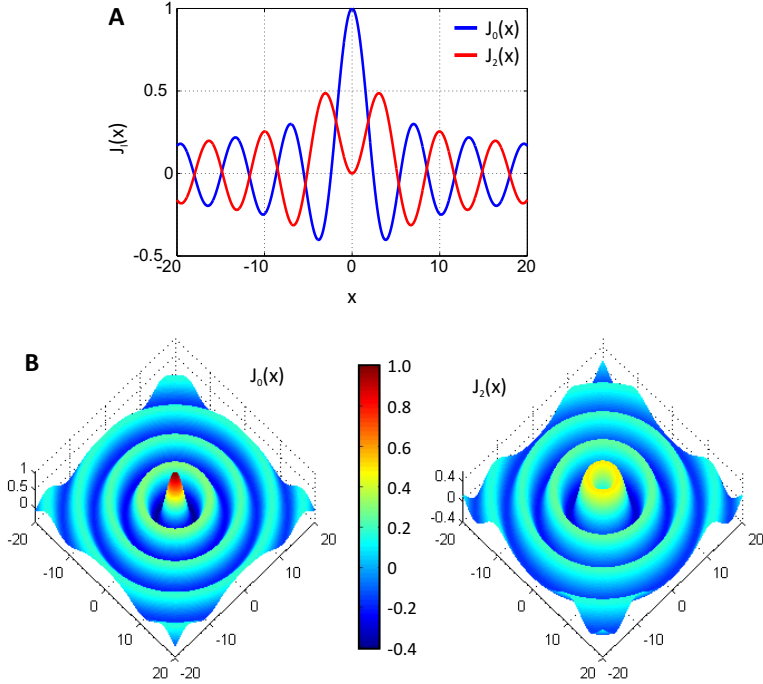


Figure 3.3.: (A) profile of the 0th- and the 2nd order Bessel function. The 0th order Bessel function in blue shows a maximum at zero position, the 2nd order Bessel function in red has a minimum in the center. (B) 3D plots of the 0th- and the 2nd order Bessel function describe the plasmonic pattern.

In figure 3.3 (B), 3D plots of the J_0 - and the J_2 Bessel functions are illustrated. The color coding represents the maximum 1 of J_0 in red and its minimum of 0.4 in dark blue. The second order Bessel function on the right side has a local minimum at the central position and therefore, its maxima are shifted compared to J_0 . These plots describe the characteristic plasmon mode pat-

terns, supported by a spiral structure.

In addition, higher order spiral structures of geometrical charge m [45] are used to investigate angular momentum transfer from light to a plasmonic system. Here, corresponding to the structure geometrical charge, multiple SPP waves are excited, which result in a complex pattern. In the center of the spiral, a lobe structure is formed, corresponding to the geometrical charge.

Near field investigations, however, describe only the static situation, revealing no time dependent information about the plasmon orbital angular momentum. In chapter 7.4, time-resolved two-photon photoemission microscopy is used for dynamic SPP investigations on spiral structures of different geometrical charges up to $m = 20$. This method facilitates full analysis of the temporal development of SPP orbital angular momenta generated by such helical structures.

A BRIEF INTRODUCTION TO ELECTROCHEMISTRY

Electrochemistry [46] is a scientific field that extends into several directions. It aids material- and surface science, establishing an atomistic picture of solid-liquid interfaces [47, 48]. Furthermore, detection of molecular trace elements can be realized via electrochemical spectroscopy. Most applications, however, are galvanic and metallization techniques. In this work, a new electrochemical reaction is introduced, demonstrating the dissolution of a gold electrode and subsequent formation of single crystalline gold platelets. Therefore, some basic definitions and relations should be given within this chapter.

The intrinsic processes, which are investigated in electrochemistry, are charge transfer reactions. During such chemical reactions, charge exchange between ions from an electrolyte and metal electrodes are analyzed. Thus, conversion from electric current in the metal electrodes to ionic current in the electrolyte is one special characteristic.

Figure 4.1 exemplarily describes a simple electrochemical reaction. Usually, an electrochemical reaction takes place within an electrochemical cell, filled with liquid electrolyte. In figure 4.1, the electrolyte is based on hydrochloric acid (HCl). In aqueous solution, HCl splits into positively charged hydronium ions (H_3O^+) and negatively charged chloride ions (Cl^-). Two metal electrodes are immersed into the electrolyte. Usually, they are chemically stable and therefore not affected by electrochemical processes. To start the reaction, a potential is applied between the two electrodes. One electrode is the source of negative charge carriers (cathode), the other one is positively charged (anode). Due

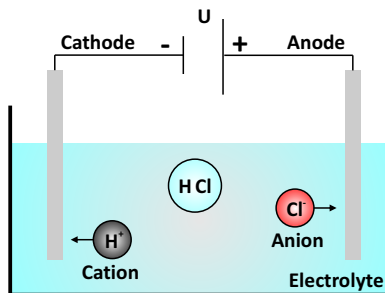


Figure 4.1.: Schematic illustration of an electrochemical reaction, using an HCl electrolyte as example. A potential is applied between the two electrodes. Therefore, the negatively charged cathode attracts positively charged ions from the electrolyte, while the anode attracts the negatively charged ions.

to an applied potential, a force is exerted on the ions in the electrolyte and thus, they are attracted from the oppositely charged electrodes. Positively charged hydronium ions, the cations, move towards the cathode, and negatively charged chlorine ions are moving towards the anode. This ion movement is defined as ionic conductivity.

At the electrodes, a charge equilibrium appears after a certain reaction time. This is sketched in figure 4.2, where the microscopical charge distribution at a metal-electrolyte interface is illustrated schematically. Usually, this is compared to a capacitor model. One part of the capacitor is the positively charged metal electrode and the other part consists of negatively charged ions, having a defined distances from the metal electrode. Region i) in figure 4.2 describes the inner Helmholtz plane, where ions are directly attached to the electrode. Region ii) is defined as outer Helmholtz plane, where completely hydrated ions are bound to the positively charged metal electrode. Due to their hydrate shell, these ions are not in direct contact with the electrode.

Charge transfer reactions can only take place within this capacitor region. Using again the HCl example, chlorine ions transfer their electrons to the anode and therefore, negative charge is removed from the electrolyte. This process is defined as oxidation

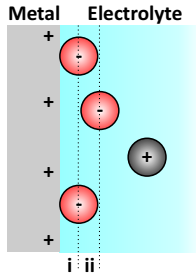


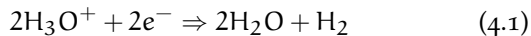
Figure 4.2.: Metal-electrolyte interface, depicted in more detail. Oppositely charged ions are attracted from the metal electrode and build up a capacitor. This capacitor is defined by two regions, i) the inner Helmholtz plane and ii) the outer Helmholtz plane.

of the negatively charged species to its elementary state.

At the cathode, a reverse process occurs. Electrons are released into the electrolyte solution and directly absorbed by the positively charged H_3O^+ ion. Consequently, the H^+ -Ion is reduced to elementary hydrogen. The cathode reaction initiates the reduction process of positively charged ions. The two elementary products of this reaction, hydrogen and chlorine, escape as gaseous substances into the atmosphere.

The overall electrochemical reaction, consisting of one reduction and one oxidation step, is called redox reaction and can be summarized by the following reaction system, using again the example of HCl:

- Ion reduction at the cathode:



- Ion oxidation at the anode:



- Overall electrochemical reaction:



In the following chapter, electrochemically decomposition of a gold electrode and the subsequent rearrangement of gold atoms into single crystalline gold platelets are investigated.

SINGLE-CRYSTALLINE GOLD PLATELETS

5.1 OVERVIEW

Single-crystalline gold platelets are fascinating because of their ideal triangular or hexagonal shape and atomically flat surfaces. Normally, their lateral size extends up to several tens of micrometers without any crystal defects, while their extension in height is in the nanometer range. This makes them highly attractive for plasmonic nano-structure fabrication and related applications. Therefore, a multitude of wet chemical reactions appeared within the last decade. However, three completely different principles should be briefly highlighted here.

Well established is the formation of gold nuclei in ethylene glycol solution due to heating [49]. Due to aniline oxidation and adhesion of these surfactants at the lowest energy (111)-facet of the gold seed, gold growth in the third dimension is prevented and growth only occurs in lateral directions. The reaction yields a large amount of gold platelets, up to several micrometers side lengths but only a few nanometers height. After a washing process, the platelets are contained in ethanol solution. The platelet solution can be drop-coated onto any arbitrary substrate, making this method quite attractive for many applications in plasmonics and material science.

A phase-transition method [50] results in remarkably large gold platelets of hundreds of micrometers lateral dimension. Here, gold chloride ions in aqueous solution undergo a phase transition into organic toluene solution where tetraoctylammonium bromide is the phase transfer agent. The organic phase is separated and drop-coated onto a suitable substrate. Heating over several hours leads to the desired gold platelet structures.

Park et al. applied a completely different radiolysis method [51].

They observe in-situ the growth kinetics of gold nano prisms due to reduction of gold ions in aqueous solution during electron irradiation in a transmission electron microscope (TEM) liquid cell. This technique is extremely powerful to study crystal growth on the atomic scale.

5.2 ELECTROCHEMICAL REACTION AND PLATELET GROWTH

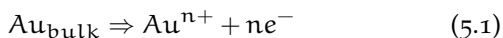
Within this work, a new approach to synthesize micrometer sized single-crystalline gold platelets electrochemically is introduced. In this section, the synthesis is explained and first insights into the proposed growth mechanism are given.

In figure 5.1, setup and synthesis of single crystalline gold platelets are explained schematically by introducing the electrochemical reaction. The reaction takes place in an electrochemical cell, as illustrated in figure 5.1 (A). The flat dish is filled with 15 μl of 0.14 molar HCl, which is used as supporting electrolyte. Two gold wires, acting as working electrode (WE) and counter electrode (CE), are extending into the solution. The WE usually carries out the reaction of interest, whereas the CE closes the electric circuit from the electrolyte to the voltage source, which is a WaveNow potentiostat from Pine Research Instrumentation. The electrodes are placed directly next to each other in the middle of the electrochemical cell, and a substrate of arbitrary shape and material is placed underneath to collect the precipitated structures. In order to normalize the reaction to the normal hydrogen standard in electrochemistry, a silver-silver chloride reference electrode is utilized.

The reaction mechanism is explained in figure 5.1 (B). It proceeds at room temperature during a cyclic voltammetry experiment, sweeping with 1 mV/s between -150 mV and $+180$ mV. While a negative voltage is applied to the WE, the CE is positively charged. During the electrochemical reaction, positively charged gold ions are dissolved from the CE into the electrolyte. These are attracted from the WE and reduced back to atomic gold [52]. Additionally, negatively charged ions in the electrolyte reduce

gold ions from the sacrificial CE back to the zero oxidation state. Finally, these gold atoms aggregate to crystalline seeds which grow during the reaction until they have a certain weight and then precipitate onto the substrate. Due to further adsorption of gold atoms, the crystal growth proceeds on the substrate until triangular and hexagonal platelets have reached micrometer-size. Usually, the reaction is stopped after 3.5 hours. The overall reaction can be summarized by the following two equations.

- Gold ionization at the counter electrode:



- Back reduction of gold ions at the working electrode and in the electrolyte:

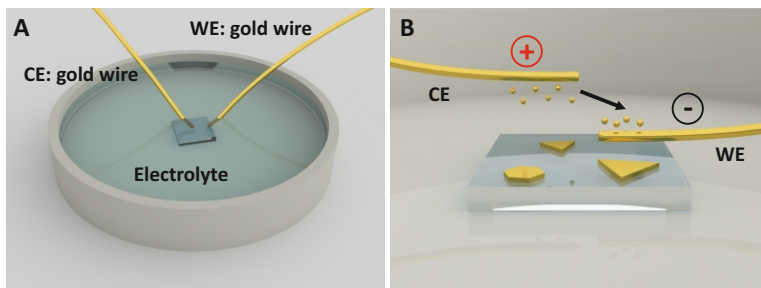
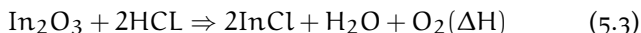


Figure 5.1: (A) Electrochemical cell, filled with dilute hydrochloric acid which is used as electrolyte. Two gold wires are working- and counter electrode, respectively and underneath the two electrodes, the precipitated material is collected by a substrate. (B) An electric potential between the two electrodes causes dissolution of the positively charged counter electrode. Positively charged gold ions are reduced back to gold atoms at the working electrode and in the electrolyte where they aggregate and form new structures.

Requirement for the synthesis to proceed is the following pre-process. One glass substrate of 1 cm^2 in size, which is covered with a thin layer of 20 nm indium tin oxide (ITO), is added into the electrolyte. The ITO film was sputtered with a Leybold ZV 6000 DC sputter machine and receives no further treatment. Due to the HCl-based electrolyte, the ITO layer is etched away from the glass substrate according to the following reaction [53]:



These new products seem to be essential for intense gold dissolution and ionization from the CE, recrystallization, and structure formation. Further and more detailed investigations about this mechanism are in progress. We suspect that the indium acts as essential surfactant. Whether this process can be controlled also by adding InCl to the solution or with other surfactants is so far unknown.

In figure 5.2 (A), the applied voltage is illustrated for five electrochemical cycles. During one electrochemical cycle, the potential between WE and CE runs through a voltage range between -150 mV and $+180 \text{ mV}$. During the cyclic voltammetry process, the ionic current is recorded in dependency of the applied voltage. The corresponding voltammogram is plotted in figure 5.2 (B). Apart from an initial negative current peak, which originally comes from the potentiostat, no remarkable features are observable. The ionic current is around $25 \mu\text{A}$ during the entire experiment.

5.3 IN-SITU CHARACTERIZATION

It is of highest interest to study the gold platelet growth in-situ during the electrochemical reaction. Therefore, the electrochemical cell is designed to be combined with an inverted optical microscope Nikon Eclipse TE2000U which is equipped with a digital camera Nikon DXM1200C and can be used both in bright- and dark-field mode. Using a magnification of 60x in the transmission bright-field mode, a movie of our gold platelets during

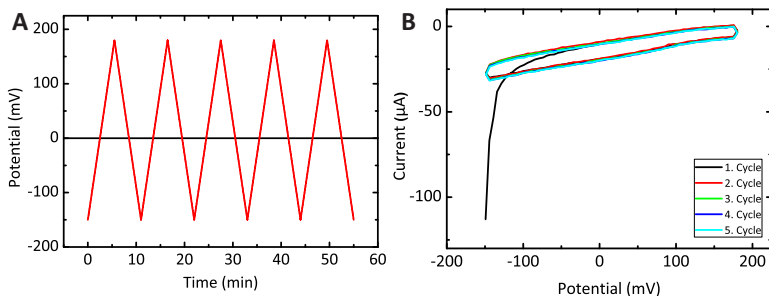


Figure 5.2.: (A) Delta voltage between -150 mV and $+180$ mV used for cyclic voltametry. (B) The corresponding cyclic voltamogram represents the ionic current between working- and counter-electrode.

growth has been recorded. The overall reaction time is 3.5 hours and one image per minute is recorded while the gold platelet structures precipitate onto a transparent glass substrate. In figure 5.3, four representative images of different growth stages are illustrated. Within the first hour, the reaction is initialized. Gold ions are produced from the counter electrode, and seeds on the atomic scale are formed. Approximately 50 minutes after the reaction was started, a few gold platelets become visible in the optical microscope, see figure 5.3 (A). During the reaction, the particle within the red circle is observed. Figure 5.3 (B) shows the situation after 1.5 hours after the electrochemical reaction is started. Platelets are growing in lateral size and their amount is increasing. Now, the particle within the red circle clearly has triangular shape. The next snapshot is taken after 2.5 hours reaction time and illustrated in figure 5.3 (C). Several platelets stop growing in lateral direction. Instead, they preferably increase in height, resulting in darker areas in the microscope images. The platelet in the red circle has performed a shape transition from triangular to hexagonal. New seeds are still added and the amount of platelets is still increasing. The reaction is stopped in figure 5.3 (D) after 3.5 hours. Eventually, the substrate is covered with a statistical ensemble of hexagonal, triangular and truncated triangular gold platelet structures of different sizes, up to several

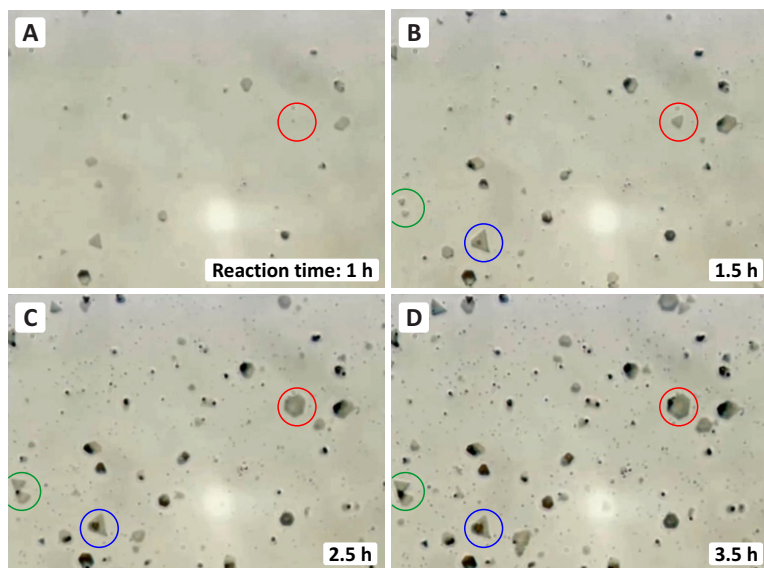


Figure 5.3.: Platelet growth during the electrochemical reaction observed with an optical microscope at four different growth stages: (A) after 1 hour, (B) after 1.5 hours, (C) after 2.5 hours and (D) after 3.5 hours. The platelet marked with a circle performs a shape transition from a triangle to a hexagon

tens of micrometers. Usually, these structures do not overlap and seem to have a perfectly smooth surface and highly geometrical shapes. As inevitable side products of this electrochemical reaction, small colloids and clusters come along with gold platelets. In addition, two more interesting crystallographic phenomena are introduced, resulting in different types of twin-structures. At the top of the blue circled platelet in figure 5.3 (B) a second particle starts to grow. It continues to grow until the reaction is stopped. The second phenomenon is marked within the green circle. The two platelets are well separated in figure 5.3 (B). However, they approach during the reaction and overlap already in figure 5.3 (C), after 2.5 hours. In chapter 5.4.4, the crystallography of special platelet twin-structures via electron diffraction is described in more detail.

This picture is confirmed by the low magnification scanning electron microscopy (SEM) image shown in figure 5.4 (A). There is a large amount of well separated, extremely flat hexagonal, triangular, and truncated triangular gold platelet structures, spread across the whole square-centimeter substrate. The high magnification SEM image in figure 5.4 (B) reveals all possible types of platelet structures, showing highest symmetry without any defects.

It is essential to determine the material composition of these synthesized structures. In collaboration with the Max Planck Institute for Solid State Research in Stuttgart, energy dispersive X-ray (EDX)² spectroscopy is performed to analyze their material composition. A typical EDX spectrum is shown in figure 5.5, which only reveals peaks at the characteristic energy values for gold. This exhibits that the platelets solely consist of gold, without material impurities. Ingredients from the electrolyte only help the reaction to proceed and are not incorporated into the precipitated gold structures, which is particularly true for ITO. However, the EDX spectrum shows traces of silicon and carbon. These signals are caused by the substrate and an adhesive carbon pad, which is used to fix the sample in the measurement system.

² EDX measurements: Claudia Kamella, Max Planck Institute for Solid State Research, Stuttgart

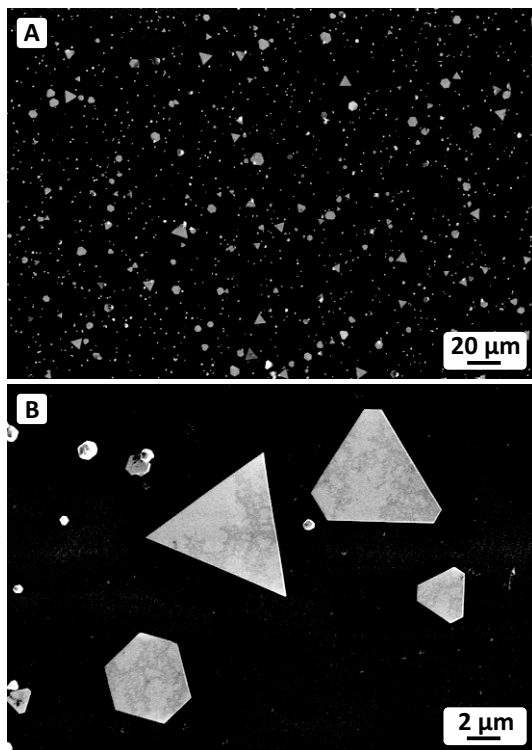


Figure 5.4.: The low magnification SEM image in (A) gives an overview, showing a statistical ensemble of regularly shaped gold structures of different sizes. The zoom-in in (B) illustrates the synthesized structure types. Triangles, truncated triangles and hexagons up to 10 μm in lateral size are present within the sample. Growth time is 3.5 hours.

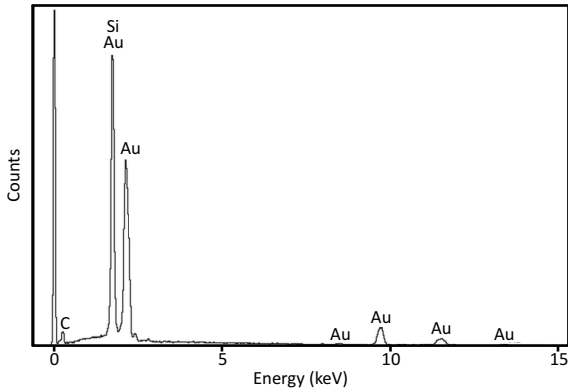


Figure 5.5.: The characteristic EDX spectrum of synthesized platelet structures gives information about the material composition. Peaks related to gold are the only features occurring. The two elements silicon and carbon correspond to the substrate and an adhesive carbon patch, respectively.

5.4 GENERAL CHARACTERIZATION OF ELECTROCHEMICALLY GROWN GOLD PLATELETS

Electrochemically synthesized gold platelets exhibit highly symmetric shapes and extraordinarily flat surfaces. This motivates a thorough analysis of the surface morphology and the crystal structure. In this chapter, different analysis techniques are applied to fully characterize their surface and crystal quality.

5.4.1 Atomic Force Microscopy

To investigate height distribution and surface quality of these electrochemically grown gold platelets, atomic force microscopy (AFM) measurements³ are performed by using a Veeco Dimension Icon instrument which is suitable for tapping mode in air performance. AFM analysis is carried out with the Veeco Nanoscope software package. During the whole electrochemical platelet syn-

³ AFM measurements: in collaboration with Adrian Ruff, Institute for Electroanalysis and Sensor Technology, University of Bochum, formerly: Institute for Polymerchemistry, University of Stuttgart

thesis, the height distribution of several platelet ensembles has been determined. The minimum height is 10 nm and the maximum measured is around 300 nm, depending on the reaction duration. However, thick platelets tend to be inhomogeneous in height and have other irregularities as well as defect structures. To study the surface character of electrochemically grown gold platelets, AFM measurements on top of a platelet are performed, see figure 5.6 (A). A suitable spot is selected and a high-resolution scan over this small area is made, as shown in figure 5.6 (B). However, AFM measurements are not performed in high vacuum, which is why particles from air adsorb to the surface, which can be seen in the AFM image. The profile plot in figure 5.6 (C) is taken along the black cross-section line and shows no remarkable surface roughness, excluding all impurities attached to the sample. Height deviations of only a few Ångströms are observable which is within the AFM noise level. This suggests the investigated gold platelets to be perfectly smooth, indicating neither surface defects nor atomic steps.

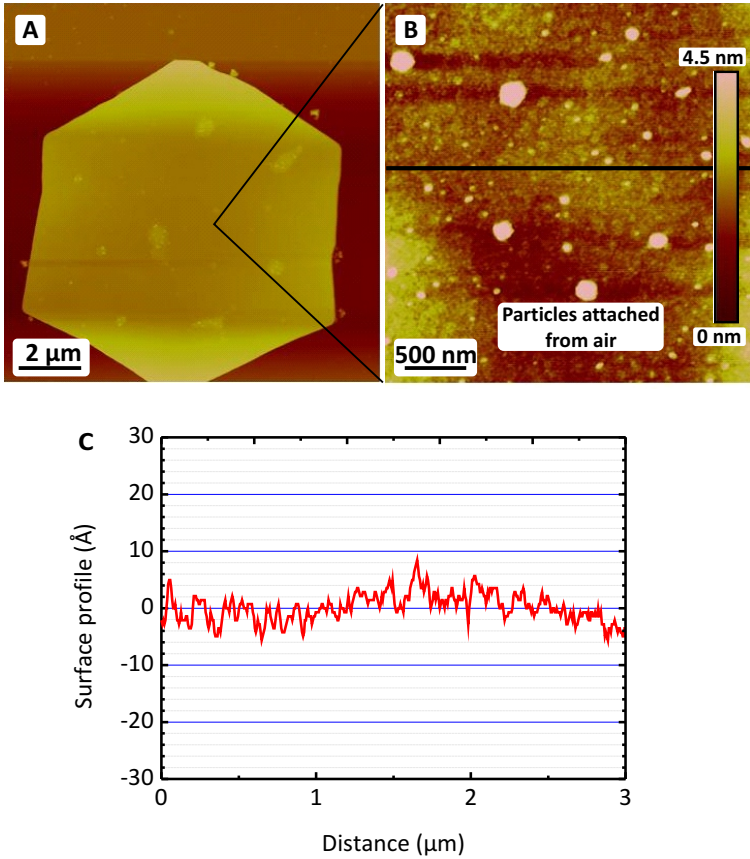


Figure 5.6: AFM surface characterization of the hexagonal platelet in A). A zoom-in image in B) yields first information about the surface character. Unfortunately, dirt particles from the air contaminate the surface area. Image C) illustrates the surface profile along the black cross-section line. It only shows AFM noise, indicating the absence of surface roughness or crystal defects.

5.4.2 *Low Energy Electron Microscopy*

To obtain precise information about the surface quality, low energy electron microscopy (LEEM) measurements⁴ are performed. This is a sensitive surface analytical method to investigate surface qualities and properties on atomic scale dimension. The experiment is carried out in ultra-high vacuum, using the Elmitec SPELEEM III setup at the University of Duisburg-Essen. To perform LEEM investigations, gold platelets are directly synthesized onto doped silicon substrates, to avoid charging effects during the measurement. Figure 5.7 depicts the resulting mirror mode LEEM image, exhibiting a hexagonal gold platelet of 120 nm height and roughly 12 μm lateral dimension, using a 15 μm field of view. Here, the ultra-high surface quality becomes visible, showing neither surface contaminations nor atomic steps, crystal defects or dislocations.

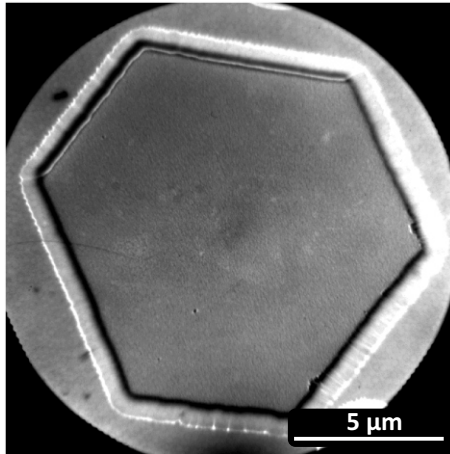


Figure 5.7.: Mirror-mode LEEM image of a hexagonal gold platelet. Such a surface analytical technique of high sensitivity, demonstrates their perfectly smooth surface without any atomic steps, defects or dislocations. Their surface is atomically flat.

⁴ LEEM measurements: Frank Meyer zu Heringdorf, Faculty of Physics and Center for Nanointegration Duisburg-Essen (CENIDE), University of Duisburg-Essen

5.4.3 *Transmission Electron Microscopy*

Transmission electron microscopy is an essential tool to obtain high resolution images of gold platelets as well as exact information about their crystal structure and atomic formation. Gold platelets are directly synthesized onto a 30 nm thick silicon nitride membrane of 1 mm² size and analyzed using the Zeiss Sub-eV-Sub-Ångström-Microscope (SESAM) at the Max Planck Institute for Intelligent Systems in Stuttgart. Figure 5.8 represents different TEM images⁵ of typical platelet structures. The images confirm the high crystal quality without any noticeable defects. However, tension and strain fields extending all across the platelet are visualized by TEM, resulting in different stripe patterns. These are caused by deformation and bending of the platelet during deposition onto the substrate and the drying process. On top of the lowermost structure, a second platelet, which is completely black, started growing. The induced stress onto the big platelet underneath is recorded by TEM.

⁵ TEM images, electron diffraction and EFTEM measurements: Wilfried Sigle, Max Planck Institute for Intelligent Systems, Stuttgart

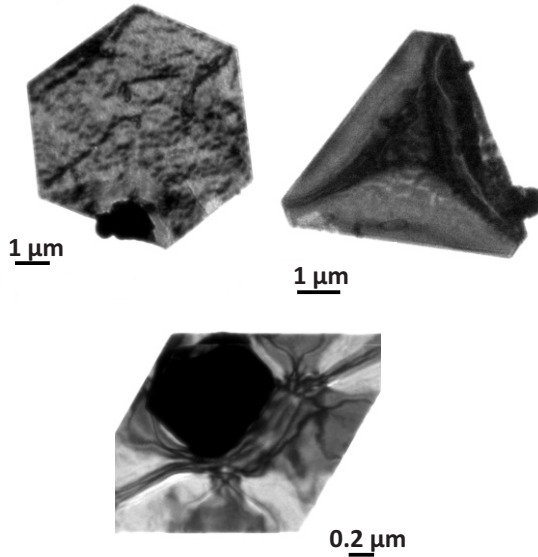


Figure 5.8.: TEM images of different gold platelets. They exhibit strain fields and tension extending over the entire structure, illustrated by different gray shadings. On top of the lowermost platelet, a second platelet started to grow (black area). This causes disturbances, which can be visualized by the TEM.

5.4.4 *Electron Diffraction*

Furthermore, the TEM provides the possibility to perform selected area electron diffraction (SAED) on different samples and therefore study the atomic arrangement of our gold platelet structures. For investigation, a platelet of about 6 μm lateral size dimension is chosen and electron diffraction scans are performed at several positions. As result, a perfectly hexagonal symmetric diffraction pattern is obtained at each investigated spot, as depicted in figure 5.9. This proves the electrochemically synthesized gold platelets to be face-centered cubic (fcc) single-crystals, grown along the (111)-plane which is supported by the substrate.

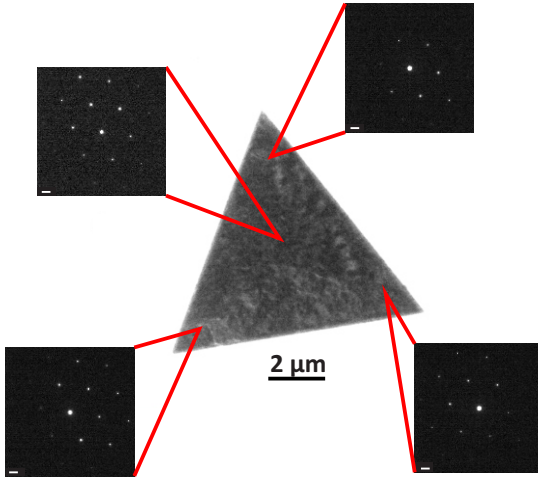


Figure 5.9.: An electron diffraction scan over the pictured triangular platelet shows hexagonal atomic arrangement of the (111)-facet at each position. This indicates single-crystallinity in (111)-direction. The scale bar of all diffraction patterns is 21 nm.

During platelet growth, different kinds of defect structures can occur within the single-crystalline gold platelets. In figure 5.10, a Siamese twin structure is shown as an example, where two gold platelets are grown together and inseparably connected to each other. The high magnification image of the red circled area illustrates the seam region of the two platelets, showing several cracks and perturbations. SAED in the seam region gives a surprising picture: the pattern exhibits twelve-fold symmetric arrangement of the constitutive atoms, which can be interpreted as superposition and anchoring of the two individual parts.

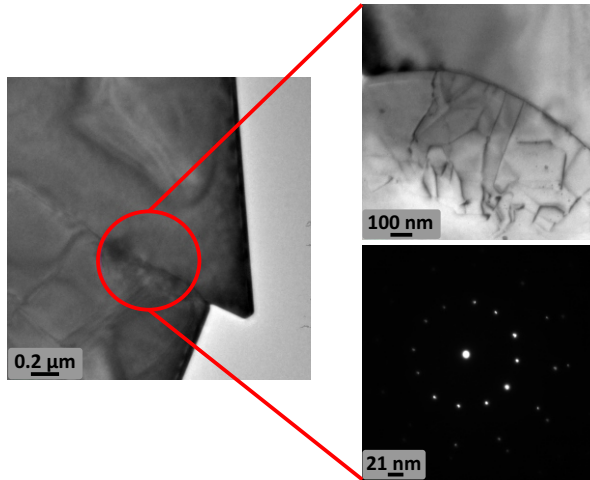


Figure 5.10.: Example for one defect type: TEM image of a Siamese twins structure. Zoom into the red circled area, illustrates the seam region where the two platelets are grown together. The electron diffraction pattern within this overlapping zone shows twelve-fold symmetric arrangement of the constitutive atoms.

5.5 ENERGY FILTERED TRANSMISSION ELECTRON MICROSCOPY

Keeping the fascinating characteristics of electrochemically synthesized single crystalline gold platelets in mind, their plasmonic properties should be equally striking. As first approach for plasmon excitation on these single crystalline gold platelets, transmission of high energy electrons through the sample is considered, which is possible with TEM techniques.

Already in the year 1957, Ritchie theoretically described energy- and angular distribution of fast electrons penetrating a finite metal foil [26]. For that purpose, he assumed these high energy electrons to lose a significant amount of energy to plasma oscillations, so-called plasmons, in the sea of conduction electrons within the bulk metal.

Powell and Swan confirmed the theoretical predictions of Ritchie by measuring characteristic electron energy loss features in aluminum and magnesium films using a reflection geometry [27, 28],

while Stern and Ferrel considered transmission spectra [29]. Furthermore in [29], a theory is developed which considers the native oxide layer covering these metals. Measurement of angle dependent energy loss spectra allows determination of the dispersion relation of radiative surface plasmons in thin oxidized aluminum films [30].

A special technique in transmission electron microscopy is energy filtered transmission electron microscopy (EFTEM), where a focused electron beam of high kinetic energy impinges on the sample. These electrons interact with conduction electrons of the gold atoms, transfer energy and thus excite electron oscillations. Due to this interaction, the transmitted electrons lose a specific amount of energy, which is associated with the excited plasmon modes. Detection of transmitted electrons allows for formation of a 2D energy-filtered image of the sample [54]. This technique enables imaging of all localized surface plasmons modes, which are non-propagating oscillations of the conduction electrons in a small metal particle, see chapter 5 in reference [6].

A triangular platelet of about $1\ \mu\text{m}$ side lengths is used for EFTEM measurements, which are shown in figure 5.11. Furthermore, an energy resolved image series is depicted together with the corresponding energy loss between $1.6\ \text{eV}$ and $0.6\ \text{eV}$, respectively. The temperature color scale of the images illustrates the energy-loss probabilities. Blue colors imply low energy-loss probability whereas bright colors (yellow) indicate maximum energy-loss probability. This directly illustrates the enhanced electromagnetic near fields generated by the plasmonic oscillation. Equidistant field maxima in the $1.2\ \text{eV}$ -, $1.0\ \text{eV}$ - and $0.8\ \text{eV}$ energy loss images indicate higher order plasmon modes, as explained in [55].

The platelet in figure 5.11 has approximately $1\ \mu\text{m}$ lateral dimension and a thickness of about $50\ \text{nm}$, which is big for TEM investigations. It is quite small in size compared to other platelets of the ensemble. Therefore, other techniques are necessary to investigate the plasmonic properties of electrochemically grown

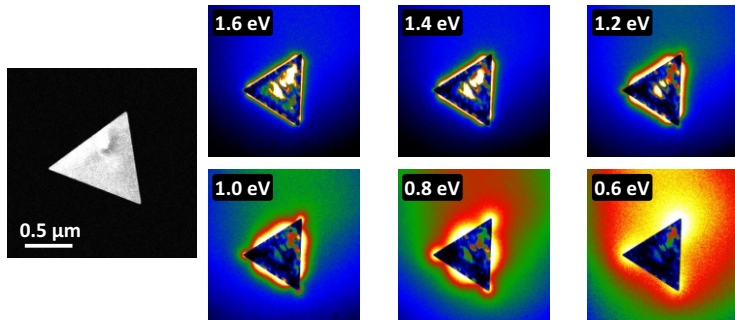


Figure 5.11.: The triangular platelet of 1 μm side lengths is suitable for EFTEM measurements. Next, six energy filtered images are illustrated and the correspondent energy loss is indicated in each inset.

single crystalline gold platelets, as will be discussed in detail in the other chapters of this thesis.

EXPERIMENTAL METHODS

Single-crystalline gold platelets offer excellent properties to study fundamental plasmonics. Due to their atomically flat, micrometer sized surfaces and their thickness of only a few nanometers, they provide the ideal system for SPP excitation at metal-dielectric interfaces. This chapter introduces patterning of gold platelets via focused ion beam (FIB) milling and the experimental concept.

Normal incidence two-photon photoemission microscopy is introduced as versatile technique for SPP excitation and imaging. Furthermore, time-resolved pump-probe measurements give insight into SPP dynamics.

6.1 FOCUSED ION BEAM MILLING

Electrochemically synthesized single crystalline gold platelets of lateral sizes between 5 μm and 10 μm are directly synthesized onto n-doped, atomically flat silicon substrates. Conductive substrates are used to avoid charging effects during the FIB milling processes. Naturally, single crystalline gold platelets have triangular or hexagonal shape. To expand their scope of application, any structure composed of single crystalline gold is highly desirable. Therefore, patterning of single crystalline gold platelets is indispensable within the following work.

This is done by FIB milling, which is an extremely versatile technique to arbitrarily pattern thin material films with structures of nanometer resolution. Here, single crystalline gold platelets are structured by using the FEI Helios 600 D534, located at the Institute of Applied Optics at the University of Stuttgart⁵. A focused

⁵ Focused ion beam milling: Liwei Fu and Huiyu Li, Institute of Applied Optics, University of Stuttgart

beam of gallium ions is used to precisely structure the single crystalline gold platelets.

To illustrate precision and versatility of FIB milling, two examples are displayed in figure 6.1. The SEM images in (A) depict a micrometer sized bow tie antenna, milled out of a hexagonal gold platelet. Magnification of the gap region in the red circled area shows the extremely high quality of this method. The gap size between the two isosceles triangles is about 50 nm. It is remarkable that the milled edges are perfectly clean and smooth without undesired material deposition, disturbances, or defects. In figure 6.1 (B), two SPP waveguides of 5 μm length, 100 nm width and 100 nm distance are milled into a single-crystalline gold platelet. The high magnification image shows structures of highest precision with perfectly sharp edges over several micrometers.

In combination with the atomic accuracy of single crystalline gold platelets, FIB milling provides an outstanding technique which allows for fabrication of structures with highest precision in the μm - and nm-range. This should lead to improvements and new possibilities in various fields of plasmonics.

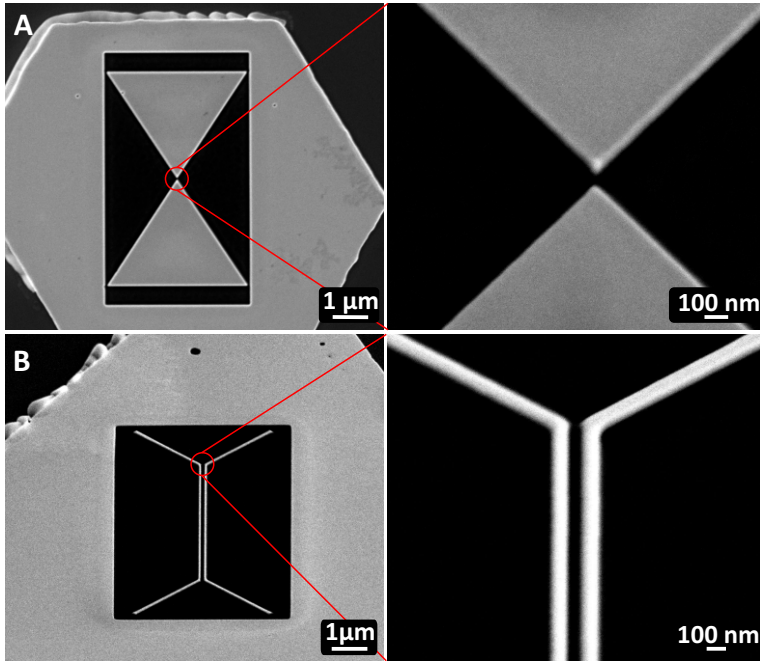


Figure 6.1.: Focused ion beam (FIB) milling is a flexible tool to structure single crystalline gold platelets with any plasmonic structure. Top: a triangular gap antenna with side lengths of about $4 \mu\text{m}$ and a gap size of around 50 nm . Bottom: waveguide structure of $5 \mu\text{m}$ length. The distance between the two wires is 100 nm .

6.2 EXPERIMENTAL CONCEPT OF PLASMON EXCITATION

Figure 6.2 schematically illustrates the experimental concept of SPP generation in general. Single crystalline gold platelets are deposited onto silicon substrates. For PEEM, the sample is placed into an ultra-high vacuum chamber. The platelets are in direct contact with the substrate and cannot be removed without being destroyed. The silicon substrate is covered with a 2.5 nm thick

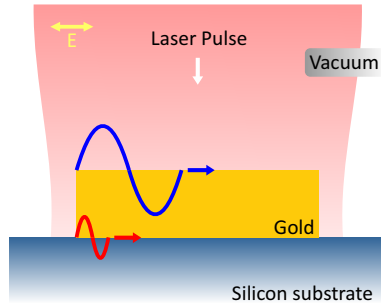


Figure 6.2.: Experimental concept: Single crystalline gold platelets are deposited onto silicon substrates. This configuration allows SPP excitation at the two material interfaces using normal incident, ultra-short laser pulses (< 20 fs) with 800 nm wavelength and linear polarization. Long-range SPPs are predominantly located at the gold-vacuum interface (blue wave) and short-range SPPs are mainly propagating at the gold-silicon interface (red wave).

layer of native oxide, which was measured ellipsometrically⁶ before. First, degassing and annealing remove adhesive molecules.

These samples possess two atomically flat material interfaces facilitating SPP excitation and propagation: one gold-vacuum-interface and one gold-silicon-interface. Due to different refractive indices of the adjacent materials, SPPs of different wavelengths are expected. Furthermore, such a sample geometry makes SPP excitation possible at the sharp platelet edges due to the compensation of momentum mismatch between incident light- and SPP electric field.

Within this work, SPPs are excited and imaged via λ PPE PEEM. During λ PPE PEEM experiments, ultrashort laser pulses (< 20 fs) of 800 nm wavelength with linear TM polarization impinge onto the sample in normal incidence configuration [56]. The polarization direction of the incident electrical field is indicated by a yellow arrow. In figure 6.2, the two SPP types are shown as different waves, propagating at each interface with different amplitude, wavelength and phase velocity. SPPs which are localized

⁶ Ellipsometry measurements: Audrey Berrier, 1st Physics Institute, University of Stuttgart

predominantly at the gold-vacuum interface are defined as LR SPPs because of their propagation distance of several tens of micrometers on top of a gold surface. Here, they are represented by a blue wave. Due to losses, they have a slightly shorter wavelength than the excitation source. SPPs, which are predominantly located at the gold-silicon interface, are labeled as SR SPPs, because of their smaller wavelength and their short range of propagation of roughly $1.2 \mu\text{m}$. They are indicated as red wave in figure 6.2 and have a significantly smaller wavelength due to the high refractive index of silicon (3.7 at 800 nm wavelength).

6.3 TWO-PHOTON PHOTOEMISSION MICROSCOPY

6.3.1 *Setup and Experiment*

Both SPP excitation and imaging within this work are carried out by normal incidence two-photon photoemission electron microscopy, using the Elmitec SPELEEM III setup at the University of Duisburg-Essen⁷ [56]. This setup also allows interferometric time resolved pump-probe measurements to study SPP dynamics [57]. In figure 6.3, the basic experimental setup is explained. 16 fs laser pulses at a central wavelength of 800 nm with appropriate dispersion management are incident on a single crystalline gold platelet, attached to an atomically flat silicon surface, at normal incidence with linear polarization. Due to a sub-monolayer of cesium atoms on the sample, the electron work function of gold is reduced and electron emission from the SPP waves is facilitated. These emitted electrons are collected by an electron objective, guided through magnetic fields and focused onto an imaging screen. Such electron optics visualizes SPP waves with nanometer resolution.

⁷ PEEM measurements are performed by Philip Kahl, Daniel Podbiel, Pierre Kirschbaum, Christian Witt and Frank Meyer zu Heringdorf from the Faculty of Physics and Center for Nanointegration Duisburg-Essen (CENIDE), University of Duisburg-Essen

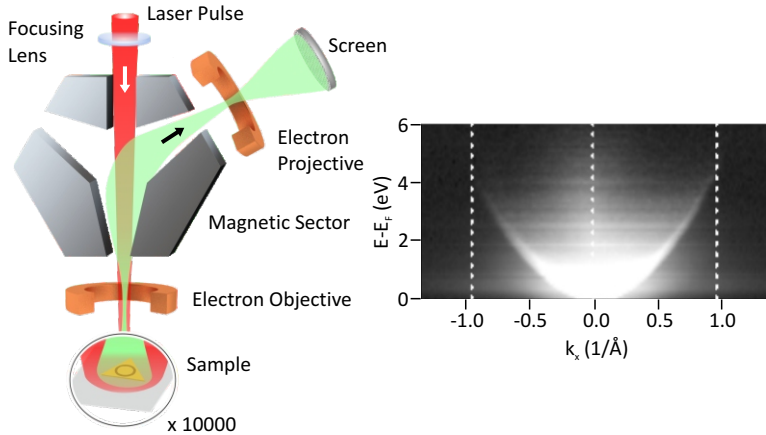


Figure 6.3.: The normal incidence two photon photoemission microscopy setup is illustrated in the left image. After SPP excitation, electrons are emitted from the sample and imaged with nanometer resolution using electron optics. As recently demonstrated, the E_x component of the surface plasmon field along the incident polarization is responsible for electron emission. The right image shows the energy dispersion for emitted electrons in dependence on the wave vector x -component k_x .

The right part in figure 6.3 depicts the cone-shaped energy dispersion of the electrons in dependence on wave vector x -component k_x of excited SPP waves within a 2PPE PEEM experiment. On the y -axis, the energy difference between excitation energy and Fermi energy E_F is plotted. This illustrates that for higher absolute values of k_x , electrons of increasing energy are emitted from the sample.

6.3.2 Basic Principles

During the 20th century, two-photon photo-electron emission has developed as versatile tool to study electron dynamics in metals [58, 59]. In parallel, it is already known that surface plasmons increase the yield of emitted photo-electrons drastically [60–62] and in combination with PEEM, a general method for SPP stud-

ies is found.

Depending on the bulk-plasma frequency of the utilized metal, femtosecond (fs) laser pulses cause a collective excitation of the conduction electrons. Redistribution of these electrons is responsible for the reflection properties and emission of photo-electrons (photo-electric effect). The main part of the optical energy, which was transferred to the electrons, is reflected as light while only a small fraction is absorbed. The absorption is caused by collective electron motions, leading to a non-equilibrium electron distribution that can exist for significant time. Finally, due to electron-phonon collisions, the equilibrium state is restored. Single-photon processes, which are associated with a first laser pulse, do not lead to photo-electron emission. Only a second laser pulse provides enough energy to emit electrons from the metal and therefore probe the electron distribution. However, application of intense laser pulses can also cause direct two-photon absorption and directly induce two-photon processes.

Such considerations directly lead to time-resolved pump-probe experiments in 2PPE PEEM to study SPP dynamics [57, 63–66]. For this purpose, incident ultra-short laser pulses are divided into two equal parts via a Mach-Zehnder interferometer and delayed in time. The first impinging pulse excites SPPs which are propagating away from their excitation area. Then, the time-delayed probe pulse interrogates the already excited SPP waves, which makes determination of their time dynamics possible. This enables studies of SPP dynamics on the femtosecond time scale. The resulting 2PPE PEEM contrast is therefore a superposition of several electric fields, generated from the incident laser pulses and SPP waves, containing several distinct features [67]. Figure 6.4 shows an SEM image of an evaporated metal film with grating coupler for SPP excitation. Underneath, the corresponding PEEM image is illustrated, explaining all occurring PEEM signatures. i) Describes the static region of the SPP field. Here, the laser- and the SPP fields are present at the same time, interfering constructively or destructively. Region ii) represents the dynamic part of the SPP pattern, where no laser pulse is present and the 2PPE

yield only comes from the SPP wave. SPP waves uncouple from the excitation grating, propagate away and decay after a certain distance. Feature iii) originates from the finite dimension of the grating coupler. Its edges produce circular waves, which constructively interfere and produce this pronounced feature.

Furthermore, recent experiments have shown [25], that the main part of 2PPE yield which is generated by SPP waves is mainly caused by the x -component E_x of its electric field vector.

For experiments performed with SR SPPs on single crystalline gold platelets, static and dynamic patterns of the PEEM image play a crucial role.

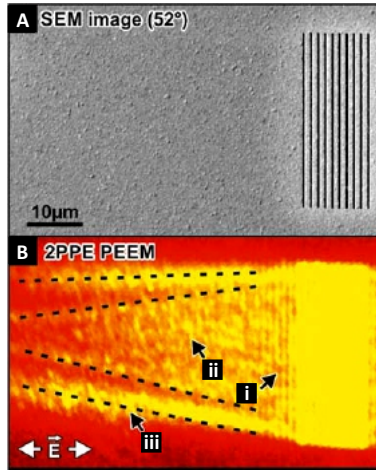


Figure 6.4.: (A) SEM image of an evaporated metal film with a grating coupler for SPP excitation. (B) Typical 2PPE PEEM image, exhibiting several characteristic features. i) Describes the static region of the SPP field. ii) Dynamic region, SPPs propagate away from the static region. iii) SPP wave front, created due to the finite dimension of the grating coupler. The image is taken from [67].

SHORT-RANGE SURFACE PLASMONICS

For many decades, researchers have been fascinated by the excitation of SPPs and the investigation of their remarkable properties. Usually, they refer to LR SPPs, which are electromagnetic waves in air or vacuum, coupled to the free electrons of a thick metal layer. In contrast, SR SPP modes are investigated in this. These are excited on a gold-silicon interface, where the wavelength is reduced drastically, mostly due to the high refractive index of the adjacent material.

The SR SPP modes have received less attention compared to LR SPPs [68–71] due to difficult accessibility, high damping and hence short decay lengths. In metals, only few attempts have been undertaken to explore SR SPPs [72]. For example, metal-insulator-metal (MIM) waveguides have been utilized, where the SPP wavelength was as short as 51 nm for 650 nm excitation light [73]. One should mention that recent efforts in graphene or other layered materials such as hexagonal boron nitride (h-BN) also exhibit extremely small SPP wavelength. Usually, this is possible at infrared wavelengths [74–77]. Moreover, there are several approaches to focus propagating SPPs [78–80]. Also SR SPP focusing on a silver-silicon nitride interface was introduced recently [81], where the minimum focal spot of 66 nm is mapped by near field microscopy.

SPPs excitation and propagation takes place at metal-dielectric interfaces. A thin metal film surrounded by two different dielectrics allows plasmonic wave propagation at each interface with different phase velocity and decay lengths because of different refractive indices of the ambient materials. Utilizing a substrate of high refractive index reduces the wavelength of excited SPPs drastically.

7.1 EXCITATION AND DYNAMICS OF LONG- AND SHORT-RANGE SURFACE PLASMON POLARITONS ON SINGLE-CRYSTALLINE GOLD PLATELETS

Normal incidence (NI) 2PPE PEEM is a versatile technique to study and image electronic surface properties of a great variety of samples. In particular, single-crystalline gold platelets offer new and outstanding possibilities to validate the theoretical considerations from chapter 2.3. With micrometer sized atomically flat surfaces and a thickness in the nanometer range, they provide an ideal system for SPP investigations at both interfaces. Furthermore, time-resolved pump-probe measurements in PEEM, allow to study SPP dynamics.

Figure 7.1 shows two 2PPE PEEM images of a hexagonal single-crystalline gold platelet, which was synthesized electrochemically and dispersed onto a silicon substrate. It has a thickness of 120 nm and approximately 12 μm lateral extension. Ultra-short incident laser pulses excite SPPs at the platelet edges. A sub-monolayer of cesium atoms, which was evaporated onto the gold platelet before, reduces the electron work function of gold and enables electron emission by the SPP wave. Depending on the polarization direction of the incident electric field vector, which is indicated by a yellow arrow, each image shows a specific SPP standing wave pattern. The central wavelength of the laser pulses is $\lambda_0 = 800 \text{ nm}$ and from the PEEM images, the SPP wavelength can be estimated slightly shorter due to losses. This identifies the SPP wave as the LR SPP, existing at the gold-vacuum interface. Due to the 120 nm thickness, only LR SPP excitation and imaging is supported by the gold platelet. During the following discussion, LR SPPs are illustrated with blue color.

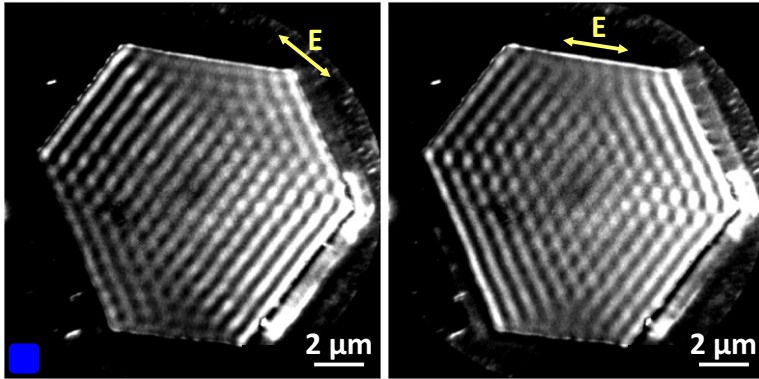


Figure 7.1: 2PPE PEEM images of a hexagonal platelet with 120 nm height show different LR SPP standing wave patterns, depending on the polarization direction of the incident electric field vector (in yellow). Within the following discussion, the LR SPP is marked in blue.

The situation changes fundamentally in figure 7.2, where SPP excitation is performed on a thin single-crystalline gold platelet of 37 nm height. According to the polarization direction of the incident electric field vector, two wave signatures become visible in the experimental 2PPE PEEM image. The LR SPP propagated across the entire platelet surface and gets blurred due to the reduced thickness of the gold platelet. The second plasmonic feature is much stronger pronounced and attracts attention because of its short wavelength. Wavelength estimation from the image and comparison with the theoretical predictions from chapter 2.3, it is determined to be the SR SPP. The PEEM image shows that SR SPPs decay after a few wavelengths of propagation. Even so, SR SPPs are excited at the gold-silicon interface and imaging of both SPP modes is possible simultaneously due to the thin gold platelet. Furthermore, thin platelets induce coupling between the LR- and SR SPPs and therefore, the resulting SPP pattern in figure 7.2 is a superposition of the LR- and SR SPP modes. In the following analysis, SR SPPs are labeled in red.

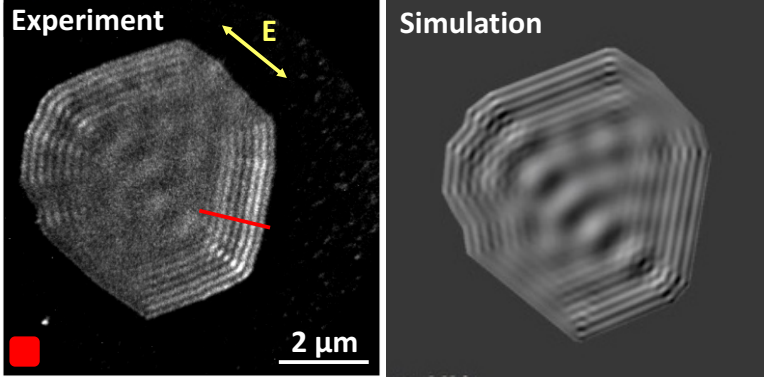


Figure 7.2.: LR- and SR SPP excitation and imaging is possible on a platelet of 37 nm height. SR SPPs are the dominant experimental feature, however decay after a short propagation distance. The SPP pattern is determined by the polarization direction of the incident light field. In the following, SR SPPs are labeled in red. The simulation image reproduces the 2PPE PEEM results.

To reproduce SPP excitation via PEEM from figures 7.1 and 7.2, a model⁹ is developed, which includes all electric fields contributing to the PEEM signal. These are the electric fields of the incident light pulses superposed with those of the excited LR- and SR SPPs at the material interfaces of the sample. Furthermore, it is assumed that SPPs are created at the edges of the single-crystalline gold platelet and propagate into the center. The platelet is approximated by a polygon of straight line segments. Each segment is supposed to be a source of plane-wave plasmons. This means, a beam of SPP waves from each line segment is added to the total electric field. The sum of all fields leads to interference effects. The plasmon electric field \vec{E}_p is taken from the known plane-wave solutions for thin films on dielectrics, including propagation losses [82]

$$\vec{E}_p(\mathbf{r}, t) = E_p \left(\frac{i\gamma\hat{n} - \alpha\hat{z}}{k} \right) G(\mathbf{r}, t - t_a) e^{i(\alpha\hat{n}\cdot\mathbf{r} - \omega(t-t_a))}. \quad (7.1)$$

⁹ PEEM model and simulations: Tim Davis, School of Physics, University of Melbourne, Australia

Here, \hat{n} is a vector in the plane of the gold platelet perpendicular to the boundary segment and \hat{z} is the normal to the platelet surface. The plasmon wave number is α and $\gamma^2 = \alpha^2 - \epsilon_m k^2$. Here, ϵ_m is the relative permittivity of the metal near the surface, $k = \omega/c$ is the free-space wavenumber, ω the frequency of light and c the speed of light in vacuum. The plasmon amplitude is multiplied by a propagating Gaussian envelope $G(\mathbf{r}, t - t_a)$, centered at time t_a , to take account of the pulsed nature of the incident light.

The electron emission rate from the surface due to coherent two-photon absorption is proportional to $I^2(\mathbf{r}, t) = |\mathbf{E}_T^*(\mathbf{r}, t) \cdot \mathbf{E}_T(\mathbf{r}, t)|^2$, where $\mathbf{E}_T(\mathbf{r}, t)$ is the sum of all electric fields from the incident light and the SPP waves. The simulation images represent the numerically evaluated time integration $\int_{-\text{inf}}^{\text{inf}} I^2(\mathbf{r}, t) dt$ for a given delay time between pump and probe pulses.

Analyzing LR- and SR SPP features quantitatively, their emission profile cross-sections are taken from the 2PPE PEEM images in figures 7.1 and 7.2. In figure 7.3, the LR SPP profile in blue is directly plotted on top of the SR SPP profile in red. From the blue curve, the LR SPP wavelength ($\lambda_{\text{LR-SPP}}$) is determined by measuring the distance between two maxima, see the vertical, dashed black lines. This is 785 nm, which is slightly shorter than the excitation wavelength of 800 nm as expected from the dispersion relation in chapter 2.3. The red emission profile shows a beat pattern of LR- and SR SPPs, indicating coupling and superposition of the two plasmonic excitations due to the small thickness of the single crystalline gold platelet. Comparison between the blue and the red curve shows accordance between the LR SPP wavelengths on these two gold platelets. The 2PPE yield coming from of the LR SPP on the 37 nm platelet is quite low. The SR SPPs, plotted as red curve are excited at the platelet edge, however, they decay after approximately 1.5 μm of propagation. After SR SPPs are decayed, only LR SPPs exist in the center of the plasmonic surface. SR SPPs, excited on the platelet in figure 7.2 have a wavelength of 185 nm ($\lambda_{\text{SR-SPP}}$).

The corresponding theoretical emission profiles from the PEEM model are plotted directly underneath, representing the LR SPP again in blue and the superposition of LR- and SR SPP from the thin gold platelet in red. The modeled results reproduce the experimental profiles. Here, the LR SPP wavelength $\lambda_{\text{LR-SPP}}$ is 780 nm and the SR SPP wavelength is 180 nm. The vertical dashed lines also show that $\lambda_{\text{LR-SPP}}$ is independent of the gold platelet thickness.

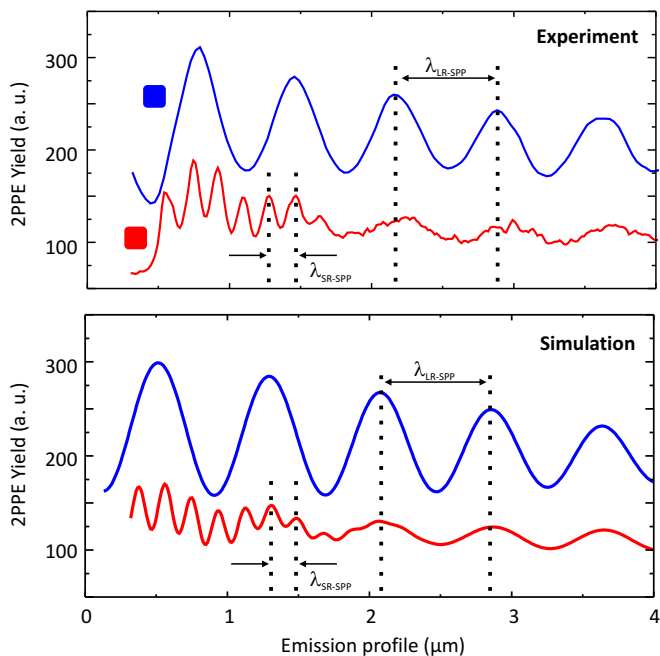


Figure 7.3.: Emission profile cross-sections from the PEEM images in figure 7.1 (blue) and 7.2 (red). The blue profile determines the long-range SPP wavelength, which is $\lambda_{\text{LR-SPP}} = 785$ nm. The red profile illustrates the superposition of long- and short-range SPPs. The SR SPP wavelength is $\lambda_{\text{SR-SPP}} = 185$ nm. Underneath, theoretical emission profiles from the PEEM model are plotted. Comparison between experiment and simulation shows good agreement for all SPP features. From the PEEM model, one can extract $\lambda_{\text{LR-SPP}}$ as 780 nm and $\lambda_{\text{SR-SPP}}$ as 180 nm.

Time-resolved PEEM measurements in figure 7.4 illustrate the dynamics of SR SPP waves. In (A), emission profiles at the red cross-section line on the 37 nm thick gold platelet in figure 7.3 are plotted for two different delay times Δt_1 and $\Delta t_2 > \Delta t_1$ between pump and probe laser pulses. Comparison of these two profiles reveal the static- and the dynamic PEEM pattern, as already introduced in chapter 6.3.2. The static area is located near the edge of the platelet, where SR SPPs are excited. Here, the electric fields from laser pulses and SR SPPs are present at the same time and therefore interfere constructively or destructively. Wave packets of different delay times maintain their position. In the dynamic region however, the signal comes from SPP waves alone and therefore reveals their dynamics [67]. SR SPP wave packages uncouple from their excitation source and start propagating. For delay time Δt_2 , the covered propagation distance is longer than for the shorter delay time Δt_1 .

Furthermore, the phase velocity of propagating SR SPPs can be calculated from these time-resolved PEEM measurements. This is illustrated in figure 7.4 (B) by plotting a sequence of emission profiles with different delay times Δt . This diagram represents the wave packet position in dependence on the pump- and probe pulse delay times. The color coding defines the bright red fields as emission maxima and from this, the characteristic PEEM features become obvious as well. Within the static region, the position of SR SPP wave packets is constant for all measured delay times. In the dynamic region however, the wave packets change their position for longer delay times. This is indicated by the dashed white line in figure 7.4 (B). The slope of the dashed white line corresponds to the phase velocity of propagating SR SPPs at the gold-silicon interface. Here, the SR SPP phase velocity is $0.23 c$, which is just a quarter of the velocity of light in vacuum c .

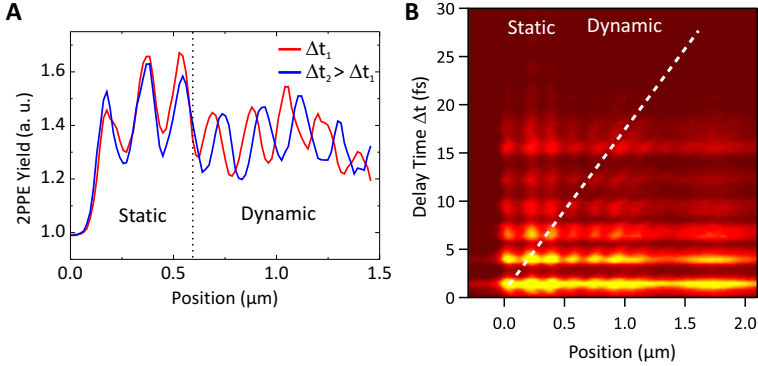


Figure 7.4.: (A) Two short-range SPP emission profiles for different delay times Δt_1 and Δt_2 illustrate the static and dynamic PEEM signal. (B) Time-resolved 2PPE PEEM measurements, represented in a delay time over wave package position plot. For longer delay times, wave packages move in position which is indicated by the dashed white line. The slope of this line corresponds to the phase velocity of propagating plasmonic waves, which is $0.23 c$.

7.2 FOCUSING SHORT-RANGE SURFACE PLASMON POLARITONS TO A 60 NM SPOT OF ELECTRON EMISSION

Figure 7.5 shows an atomically flat 22 nm thick plasmonic gold surface which has been deposited on an atomically flat silicon substrate. Here, it is demonstrated that short-range surface plasmons can be used for the creation of an electron nanofocus with smallest dimension of 60 nm for incident light at 800 nm. This is achieved in the center of a disk with 2 μm diameter cut into a triangular single-crystalline gold platelet using FIB. To assist the nanofocusing, four additional rings with a period of 150 nm have been placed around the disk (see SEM image in figure 7.5 (A)). Figure 7.5 (B) shows the time-averaged 2PPE PEEM image from the sample. At the edges, the SR SPPs are excited with an approximate wavelength of 180 nm and a decay length of about 1 μm . Along the polarization direction, in the central disk, a more intense short-range surface plasmon pattern is observed. At the edges of the triangle, interference of the SR SPPs is also observed.

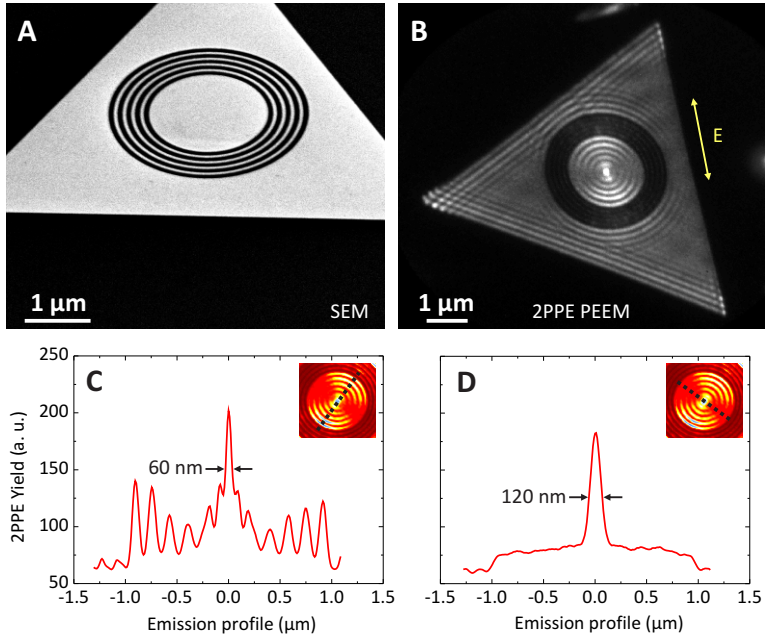


Figure 7.5.: SEM image of a 22 nm high single crystalline gold platelet, patterned with a circular grating of 150 nm period and a central disc of 2 μm diameter. The SEM view is tilted by 52°. 2PPE PEEM at 800 nm laser wavelength excites both long and short-range surface plasmons on the structured platelet. Long-range surface plasmons of about 800 nm wavelength are hardly visible, whereas the short-range plasmons are predominant. Due to the surrounding grating, the short wavelength plasmon can couple into the central disc, which acts as focusing device. At the focus point, highest electron emission is observed.

Due to the extremely high quality and the defect-free single crystallinity of the atomically flat gold film, no hot spots due to protrusions or extrusions are observed. Figure 7.5 (C) shows the false-color PEEM image from the focus and the intensity cross sections along the polarization direction. The central hot spot has a full width at half maximum (FWHM) of 60 nm, corresponding to $\lambda_0/13.3$, whereas in the perpendicular direction, shown in figure 7.5 (D), the FWHM is 120 nm. In terms of $\lambda_{\text{SR-SPP}}$ the central spot is $\lambda/3$, which is expected for a Bessel function radial slope.

The intensity profiles in figure 7.5 illustrate that there is a sharp maximum of enhanced electron emission at the focus point. Consequently, such an ultranarrow electron beam is a local electron emitter of bunches of sub-50 fs duration. This could be utilized as localized and ultrafast electron source for femtosecond electron microscopy, permitting subwavelength imaging, as well as deep subwavelength imaging illumination and lithography. In addition, enhanced light-matter interaction should occur when placing a quantum emitter directly into the nanofocus. This could also be useful for nanosensing with a very tightly focused spot that is well bound to the metal, particularly when combined with a radially polarized excitation.

In addition to the time-averaged picture in figure 7.5, time dependence of the plasmon focus is now considered in figure 7.6. PEEM data are utilized at different delay times to characterize propagation and interaction of SR SPP waves inside the single-crystalline gold disk. Using linearly polarized light, SR SPPs are launched by the circular grating and coupled into the disk. Starting from the outer static region, SPP wave fronts counter-propagate towards each other, superpose in the dynamic center and focus to a small spot due to the circular structure geometry. Due to alternating constructive and destructive interference of the counter-propagating SPP waves, a periodic change between maximum and minimum at the focal spot takes place. The two extrema are illustrated in figure 7.6. Experimental PEEM data are shown in figure 7.6 (A) and (B). Maximum electron emission

in the central focus takes place at delay time $\Delta t_1 = t_0$ between pump- and probe pulse. At $\Delta t_2 = t_0 + 1.064$ fs, after half an optical cycle, there is minimum electron emission in the focal spot. After one optical cycle, there is again maximum electron emission in the middle of the disk. To reproduce these experimental findings, the PEEM model¹⁰, introduced in chapter 7.2 is applied. The results are illustrated in figures 7.6 (C) and (D) for maximum and minimum electron emission, respectively. Taking all electrical fields contributing to the PEEM signal into account, the model confirms the experimental results in an excellent fashion.

The electron emission cross-sections parallel to the electric field vector of the linearly polarized excitation source is characterized and plotted in figure 7.7. (A) and (B) show the emission profiles for maximum and minimum electron emission, obtained from the corresponding experimental data in figure 7.6. In the time-resolved experiment, the emission maximum has a FWHM of 60 nm. Furthermore, the PEEM model provides the possibility to derive the experimental emission profiles, confirming all features occurring in the experiments perfectly.

All experimental and simulated time-resolved data are provided as movie on the attached memory stick.

¹⁰ PEEM model and simulations: Tim Davis, School of Physics, University of Melbourne, Australia

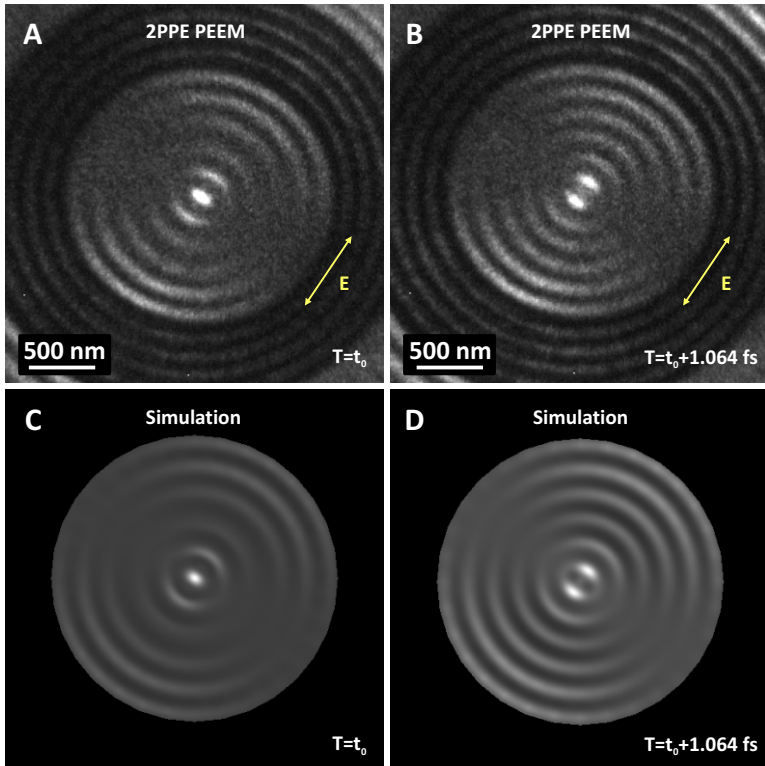


Figure 7.6.: Time resolved picture of the SR SPP focus in the $2\ \mu\text{m}$ disk. (A) and (B) show experimental data from a 2PPE PEEM pump-probe experiment. In (A), there is maximum electron emission in the center at delay time $\Delta t_1 = t_0$. (B) shows minimum electron emission at the central spot at delay time $\Delta t_2 = t_0 + 1.064$ fs between pump-and probe pulse, which corresponds to half an optical cycle. (C) and (D) show theoretical images for maximum and minimum electron emission, generated from the PEEM model.

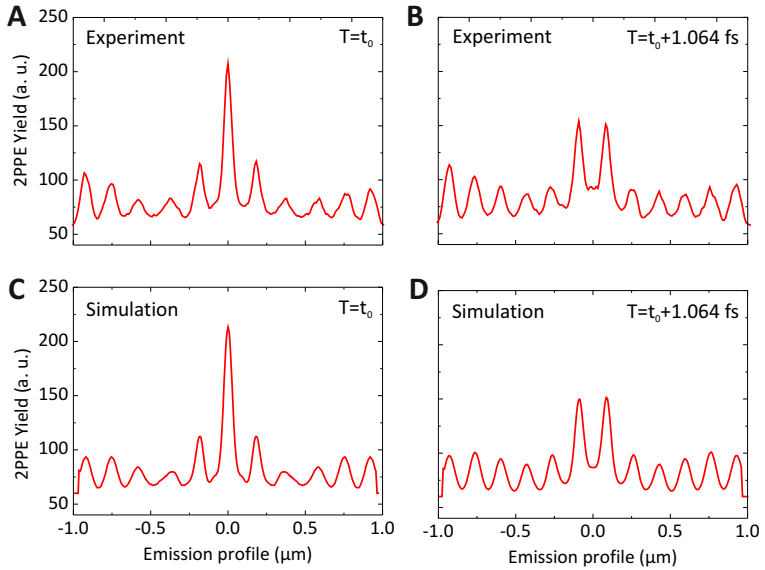


Figure 7.7.: Emission profiles corresponding to figure 7.6. (A) and (B) show profiles from the experimental data for maximum- and minimum electron emission taken parallel to the polarization direction of the electric field vector. The peak in case of maximum electron emission also has a FWHM of 60 nm. The maximum is at $\Delta t_1 = t_0$ and the minimum occurs at $\Delta t_2 = t_0 + 1.064$ fs, being half an optical cycle apart from each other. (C) and (D) illustrate the theoretical profiles derived from the 2PPE PEEM model.

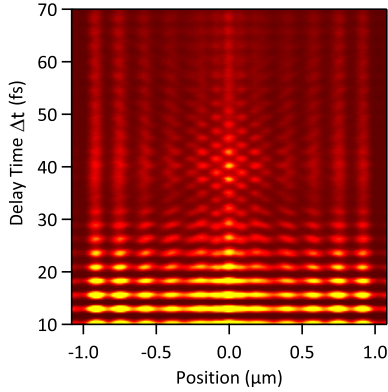


Figure 7.8: The dynamics of focused SR SPPs can be explained from time-resolved PEEM measurements as well, by plotting emission profile cross-sections in dependence of the delay time of the two laser pulses. Emission maxima are light red, the emission minima have dark red color. The focus point is located at center position 0 and the plasmon waves start propagating from the disk edges at position ± 1 .

The dynamics of SR SPPs within the focus region is illustrated and investigated with the help of figure 7.8. Delay-time dependent cross-sections through the center of the emission pattern are taken parallel to the polarization direction and stacked on top of each other. The color code of the image indicates emission maxima at bright red positions and emission minima in dark red areas. The plasmon focus point is located in the dynamic center of the plasmonic disk, at position 0 in the diagram. The edges of the disk are at positions ± 1 and in this area, the static region of the PEEM pattern is situated. For $\Delta t > 0$, SR SPPs are propagating away from the static regions and superpose in the center, depending on the time delay, constructively or destructively. Therefore, at the focus position 0, electron emission maxima and minima are alternating. The focus pattern develops with phase-velocity of the propagating SR SPP, which can be calculated from figure 7.8 in the same way as demonstrated already before in figure 7.4 (B). This yields further reduced phase velocity of the focusing SPP of 0.17 c.

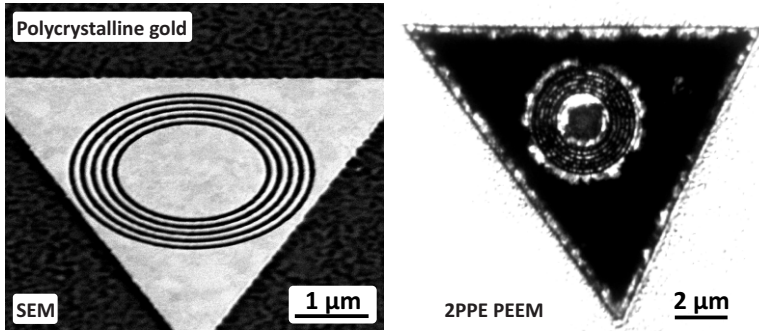


Figure 7.9.: Disk structure of $2\ \mu\text{m}$ diameter for SR SPP focusing, milled into a $20\ \text{nm}$ thick polycrystalline gold film. The SEM image is tilted by 52° . The corresponding 2PPE PEEM image illustrates that no SR SPP excitation is possible.

At this point, it is essential to compare SR SPP excitation and focusing on single crystalline gold platelets with SR SPP excitation on polycrystalline gold films. The identical disk structure of $2\ \mu\text{m}$ diameter is milled into a $20\ \text{nm}$ thick evaporated gold film. Again, a circular grating of $150\ \text{nm}$ period is milled around the disk to support SR SPP excitation. In figure 7.9, an SEM image of this polycrystalline structure is presented, already revealing rough edges as compared to the smooth single crystalline gold. It is obvious that FIB milling leads to inhomogeneous and fringed structural edges and furthermore, the surface is no longer atomically flat. This affects the 2PPE PEEM pattern drastically. On the right side of figure 7.9, the corresponding PEEM image is illustrated. Due to the fringed edges, SPP excitation, and in particular SR SPP excitation is not possible. Intense PEEM signals are only generated at inhomogeneities caused by the FIB cuts, or surface roughness and protrusions. The PEEM image in figure 7.9 points out that SR SPP focusing on polycrystalline gold structures is difficult or rather not possible. Therefore, single-crystalline gold platelets are required for SR SPP mode excitation.

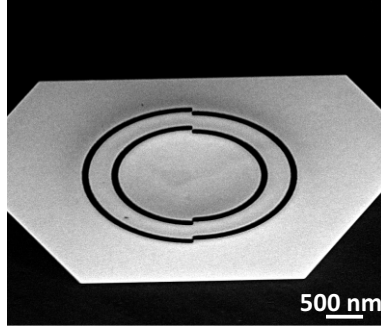


Figure 7.10.: SEM image of a plasmonic half moon structure consisting of two semicircles with radius difference $\lambda_{SR-SPP}/2$ cut into a 20 nm thick single crystalline gold platelet. The inner diameter of the structure is 2 μm. There are two parallel cuts at a distance of $\lambda_{LR-SPP}/2$ to suppress the LR SPP due to destructive interference, the width of the single cuts $\lambda_{SR-SPP}/2$, and the SEM view is tilted by 52°.

SR SPP focusing can be improved by suppressing the LR SPP. This is carried out by slightly changing the structure geometry into two oppositely placed half moon shaped cuts [44, 45, 81], as shown in figure 7.10. These are milled into a single-crystalline gold platelet of 20 nm thickness with an inner diameter of the half moon structure of 2 μm. Both of the two concentric FIB cuts have a width of $\lambda_{SR-SPP}/2$ to support SR SPP excitation and are placed in a distance of $\lambda_{LR-SPP}/2$ to suppress excitation of the LR SPP within the plasmonic lens due to destructive interference.¹¹

Using such a structure geometry for the same time-resolved 2PPE PEEM experiment as described above, a qualitative improvement of SR SPP focusing is found. The time-resolved PEEM images are illustrated in figure 7.11 for the two different polarization directions. Perpendicular to the half moon aperture in (A) and (B) and parallel in (C) and (D). Similar to the circular structure, SPP waves are excited at the structure edges according to the

¹¹ Structure design: Grisha Spektor, Department of Electrical Engineering, Technion, Israel Institute of Technology, Haifa, Israel

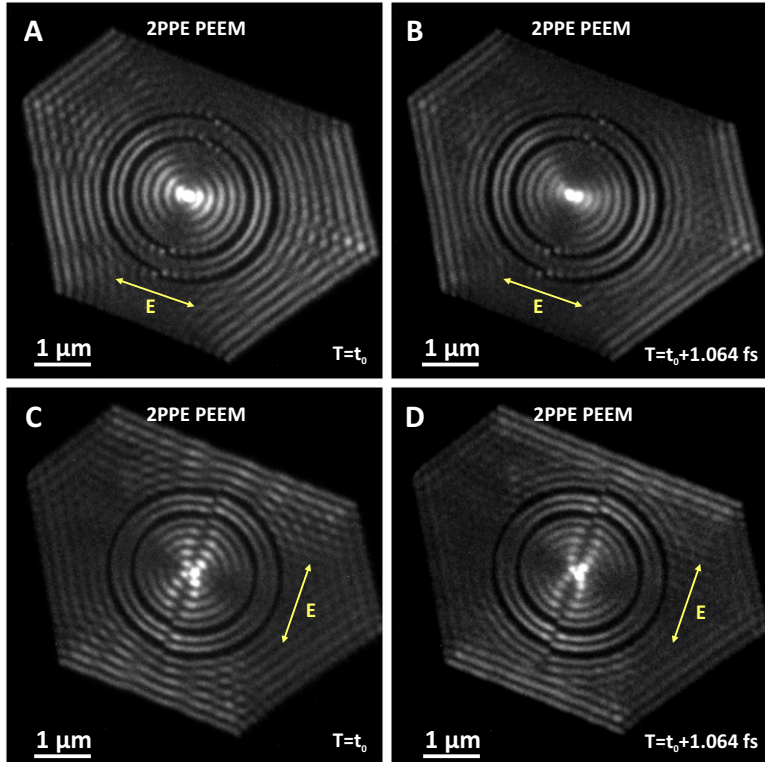


Figure 7.11. SR SPP excitation and focusing via time-resolved 2PPE PEEM assisted by a half moon plasmonic lens structure. PEEM images are recorded at two different delay times between pump and probe pulse, showing maximum and minimum electron emission in the central spot. In (A) and (B), the polarization direction of the incident electric field vector is oriented perpendicular to the half moon aperture. (C) and (D) show PEEM emission patterns where the polarization direction of the electric field vector is rotated by 90° .

electrical field polarization. They also counter-propagate to the center and superpose constructively and destructively, depending on the time-delay. The image in (A), at delay-time $\Delta t_1 = t_0$, shows a circular, intense SR SPP focus of emitted electrons in the center of the structure. Half an optical cycle later at delay-time $\Delta t_2 = t_0 + 1.064$ fs, minimum electron emission occurs in the center as already expected from the circular structure. This is depicted in figure 7.11 (B). However, during these measurements the minimum is almost covered by the strong intensity of the two side-maxima.

The SR SPP pattern changes completely in figure 7.11 (C) and (D) due to rotation of the incident electric field vector by 90° . SR SPPs are excited separately in each half moon and wave superposition takes place in the same way as already explained above. However, due to the radius difference of $\lambda_{\text{SR-SPP}}/2$, the two SPP waves, propagating through the two half moons, are phase-shifted by π . Therefore, in the center of the structure, a quite complicated SPP pattern appears at the two considered delay-times. At delay-time $\Delta t_1 = t_0$, there is an emission minimum in the smaller structure half, while a maximum occurs in the center of the bigger half moon. The situation inverts after half an optical cycle, at delay-time $\Delta t_2 = t_0 + 1.064$ fs. Now, in the middle of the big disk there is minimum electron emission and in the center of the smaller disk of the half moon structure maximum electron emission takes place.

7.3 OBSERVING THE ORBITAL ANGULAR MOMENTUM OF SHORT-RANGE SURFACE PLASMON POLARITONS

Chapter 3 introduces light carrying SAM and OAM. With the help of helical cuts in metal films, the angular momentum of light can be transferred to a plasmonic wave, which results in a vortex pattern.

Within the context of this work, SR SPPs are excited via 2PPE PEEM on electrochemically grown, atomically flat single crystalline gold platelets. Using circularly polarized light for SPP excitation provides an appropriate technique to create SR SPP vortices. For the following experiments, helical Archimedean spiral structures are milled into the smooth plasmonic gold surfaces, creating plasmonic vortex lens (PVL) structures of increasing geometrical charge m . Time-resolved PEEM measurements allow observation of SR SPP vortices and investigation of their dynamic behavior.

However, one has to be aware that in 2PPE PEEM the resulting picture is a superposition of several electrical fields with different origin. These come from incident pump- and probe pulses as well as from a contribution of the plasmon generated electric field. Within this section, the plasmonic orbital angular momentum transferred from the circularly polarized light to SPPs is described from the perspective of the PEEM observer.

The first structure investigated is an Archimedean spiral¹² of odd geometrical charge $m = 1$. It is realized by milling two concentric slits of appropriate shape into a 20 nm thick single crystalline gold platelet. The cuts have a width of $\lambda_{SR-SPP}/2$ to support SR SPP excitation and are separated by $\lambda_{LR-SPP}/2$ to suppress the LR SPP due to destructive interference. The inner diameter of the spiral structure is 2 μm . In figure 7.12, 2PPE PEEM images of the spiral with right handed sense of rotation are illustrated for one optical cycle. First, SR SPPs are excited

¹² Structure design: Grisha Spektor, Department of Electrical Engineering, Technion, Israel Institute of Technology, Haifa, Israel

by utilizing right-hand circularly polarized light (RCP), which is illustrated as white, circular arrow. The excitation light has the same sense of rotation as the structure. In the top of figure 7.12, the corresponding PEEM image at delay-time t_0 is represented. SR SPPs are excited at the slits. After leaving the static region, they coil into the central spot of the spiral and therefore having orbital angular momentum. This SR SPP movement is indicated by the red arrow. In the structural center, one single intense electron emission maximum is observed.

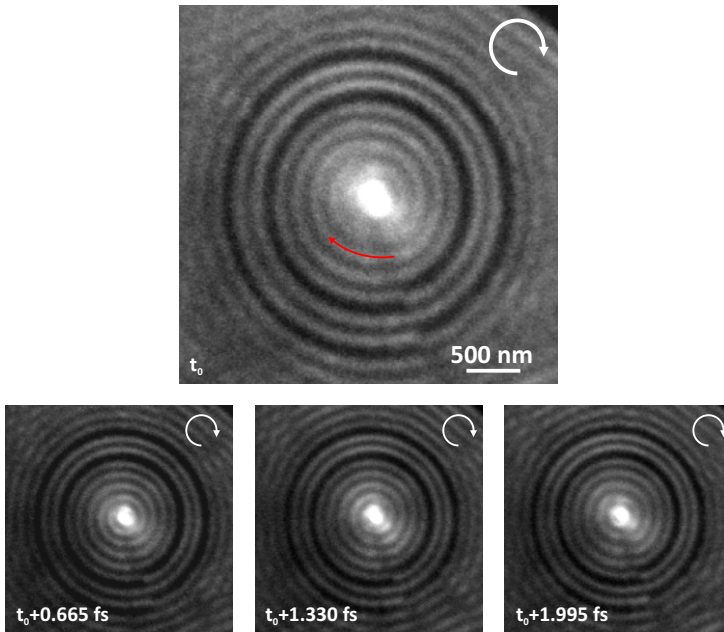


Figure 7.12.: 2PPE PEEM image of an Archimedean spiral, consisting of two slits of $\lambda_{\text{SR-SPP}}/2$ width. These two have distance $\lambda_{\text{LR-SPP}}/2$ in order to suppress the LR SPP. The SR SPP is excited with right hand circularly polarized light. In the center of the spiral, one intense focal point comes up. The time evolution is illustrated for one optical cycle.

In the lower half of figure 7.12, the time-resolved image series for SPP excitation with RCP light is presented. During one optical cycle, 2PPE PEEM images are recorded in constant delay-time steps of 0.665 fs between pump and probe laser pulses. Excitation with RCP light leads to one strong 2PPE yield maximum in the middle of the Archimedean spiral, circulating around, independent of time. See also the enclosed movie of figure 7.12.

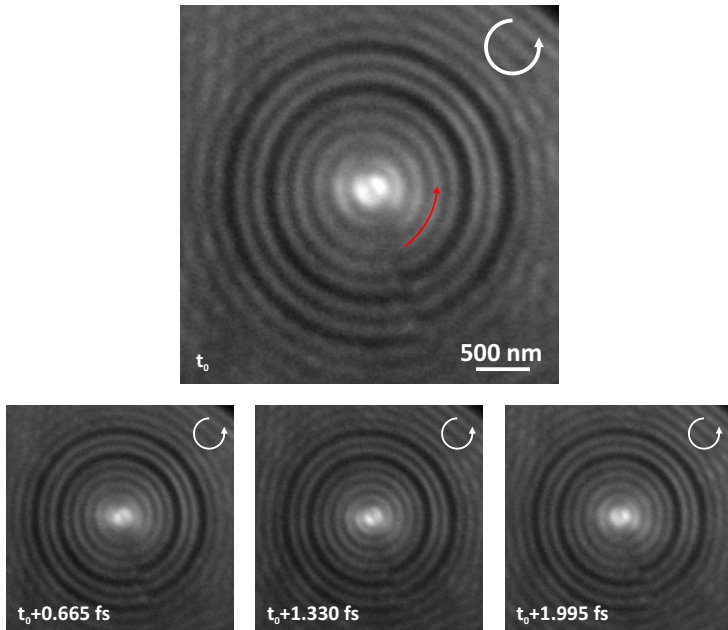


Figure 7.13.: SR SPP excitation with left hand circularly polarized light on the same Archimedean spiral structure. In the center, there is an emission minimum surrounded by two strong side maxima. The time resolved behavior is shown for one optical cycle.

In figure 7.13, SR SPPs are excited with left hand circularly polarized (LCP) light, which is opposite to the spiral sense of rotation. Now, the plasmonic pattern changes completely. SR SPP waves, which are excited at the FIB cuts, spiral contrary to the sense of rotation into the center of the Archimedean spiral. This is indicated again by the red arrow in figure 7.13. Here, the SR SPP propagation is disturbed by the structure geometry and this results in a splitting into two inhomogeneous side maxima. Consequently, in the center of the spiral, an electron emission minimum prevails. Below, time-resolved images are shown for one optical cycle using LCP light for SPP excitation. This two-lobe emission pattern exists during the complete measurement. However, the emission maxima slightly change in shape and intensity, depending on the laser pulse delay time.

These results agree with the experiments of Erez Hasman [39] on long-range surface plasmons, where such plasmonic patterns are established in near-field microscopy due to selective, spin dependent coupling of circularly polarized light to a plasmonic mode, which is induced by a spiral structure. Each circular polarization direction excites one specific spiral SPP mode. These can be described mathematically by the 0th- and 2nd- order Bessel function, ascribing topological 0 and 2 to the SR SPP excitation, respectively.

This finding impressively illustrates that spin angular momentum, carried by circularly polarized light, can be converted into OAM of SR SPPs which are created through helical grooves milled into a perfectly smooth single crystalline gold surface. The time-resolved movie of 7.13 is also provided on the memory stick.

The experiment becomes more complex by utilizing the structure illustrated in figure 7.14, combined with circularly polarized light for SR SPP excitation. This is an Archimedean spiral of geometrical charge $m = 4$ ¹³. It consists of four Archimedean spiral segments of a quarter rotation, which are twisted by a pitch of $\lambda_{\text{SR-SPP}}/2$ in a right-handed sense of rotation. Again, the structure is milled into a 20 nm high single-crystalline gold platelet, consisting of two concentric slits of $\lambda_{\text{SR-SPP}}/2$ width, placed in a distance of $\lambda_{\text{LR-SPP}}/2$ to suppress the LR SPP. During time-resolved measurements, this structure should give a twist to SR SPPs.

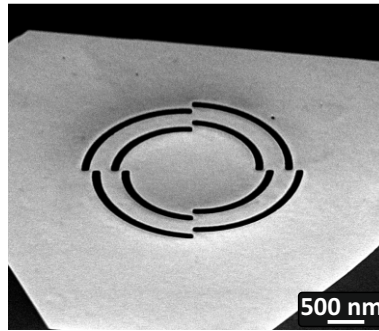


Figure 7.14: SEM image of an Archimedean spiral of geometrical charge $m = 4$, structured into a single-crystalline gold platelet of 20 nm height. The inner diameter of the structure is 2 μm . The SEM view is tilted by 52°.

Figures 7.15 and 7.16 illustrate PEEM images of the $m = 4$ structure for SR SPP excitation with RCP and LCP light, respectively. The static snapshot on the left side in figure 7.15 displays the SR plasmonic pattern, resulting in a four-lobe structure. From each spiral arm, SR SPP waves are excited and propagate towards the center of the structure, where they focus to a small spot of electron emission. As circularly polarized light is used as excitation source, orbital angular momentum is transferred to the plasmonic pattern. The direction of this rotational movement is

¹³ Structure design: Grisha Spektor, Department of Electrical Engineering, Technion, Israel Institute of Technology, Haifa, Israel

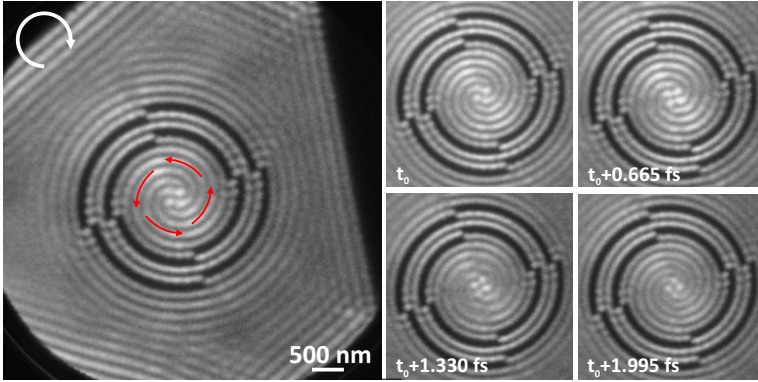


Figure 7.15.: Excitation of SR SPPs on an Archimedean spiral structure of geometrical charge $m = 4$. SR SPPs are generated by using left-handed circularly polarized light and due to the milled structure a plasmon vortex of order four is created in the center. The image series on the right shows snapshots at four different delay times during one optical cycle. Starting at t_0 , a quarter rotation of the SR SPP pattern is observed in 0.665 fs steps, illustrating the plasmonic angular orbital momentum of the SR SPP transferred from the circularly polarized light.

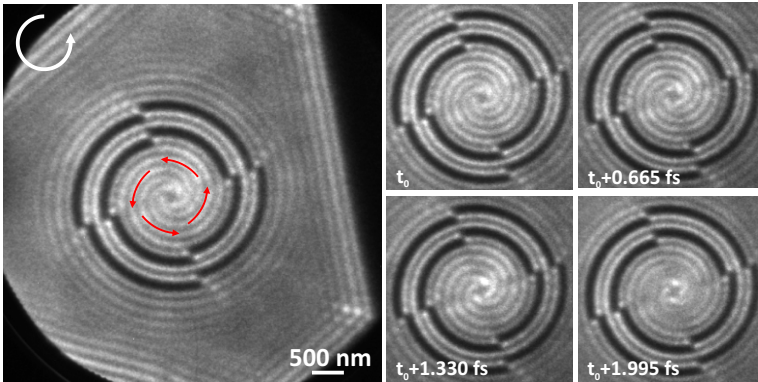


Figure 7.16.: Excitation of SR SPPs with right-handed circularly polarized light, assisted by the same $m = 4$ Archimedean spiral. Although the plasmonic pattern is less pronounced, it shows a similar four-lobe structure. During time-resolved PEEM measurements the SR SPP rotational wave exhibits the same sense of rotation as for left-handed circularly polarized light.

indicated by the red arrows around the structure center. The four pictures on the right side in figure 7.15, show the dynamic behavior of the $m = 4$ spiral during one optical cycle. The images are recorded by increasing the delay-time between pump- and probe pulse in 0.665 fs steps. During one optical cycle, the central plasmonic pattern performs a quarter rotation. It is remarkable that the rotation direction of the plasmonic pattern is opposite to the RCP excitation light. In the center of this spiral structure, inside the four focal points, there is an electron emission minimum which is not affected by the plasmon rotation.

SR SPP excitation with LCP light shows a quite similar situation, see figure 7.16. The same plasmonic four lobe pattern becomes visible in the static PEEM image on the left side, however, less pronounced and blurred. The rotation direction of the SPP pattern is again indicated by red arrows and is the same as for RCP light excitation. The time-resolved PEEM measurements during one optical cycle are illustrated on the right side in figure 7.16 in 0.665 fs steps.

Altogether, the handedness of the $m = 4$ spiral structure enforces the rotation direction of the excited SR plasmonic angular orbital momentum.

The extreme case of SAM coupling to SPPs, which was performed within this work, is illustrated by the following images. The sample geometry is enlarged by using large-sized single crystalline gold platelets, chemically synthesized according to the method in reference [50]. The result of this synthesis procedure yields gold platelets of very large lateral dimensions, between $50\ \mu\text{m}$ and $120\ \mu\text{m}$, and a thickness up to several micrometers. Archimedean spirals of geometrical charge $m = 20$ and $40\ \mu\text{m}$ inner diameter¹⁴ are milled into these atomically flat surfaces. The grating pattern of five concentric grooves of $\lambda_{\text{LR-SPP}}/2$, helps to couple LR SPPs into the structure. In figure 7.17, SEM images of this structure are illustrated.

A static 2PPE PEEM image is shown in figure 7.18. It has to be mentioned, that due to the thickness of the single crystalline gold platelet of about $4\ \mu\text{m}$, only LR SPPs can be excited, propagating at the gold-vacuum interface. RCP light is used as excitation source. Here, the measured wavelength is $\lambda_{\text{LR-SPP}}$ of $785\ \text{nm}$. LR SPPs are excited at the $m = 20$ grating and propagate towards the center. Due to constructive interference, a strong maximum of electron emission from SPP waves occurs in a central ring within the spiral structure. Due to strong electron emission, no fine structure of the SPP pattern is visible. Within this ring, destructive SPP interference takes place and in the center of the structure, there is no electron emission.

To observe the actual plasmonic pattern, which is overlaid by the strong emission effect, the background signal has to be subtracted from the 2PPE PEEM image. As expected, the right image in figure 7.18 reveals 20 focal spots of maximum electron emission, arranged in a ring structure. This pattern is generated due to constructive interference of SPP waves from each of the 20 spiral arms.

A long-time pump-probe 2PPE PEEM measurement on the $m = 20$ spiral is illustrated in figure 7.19. The images depict different delay times in $28.884\ \text{fs}$ steps, and LR SPPs are excited with RCP

¹⁴ Structure design: Daniel Podbiel, Faculty of Physics and Center for Nanointegration Duisburg-Essen (CENIDE), University of Duisburg-Essen

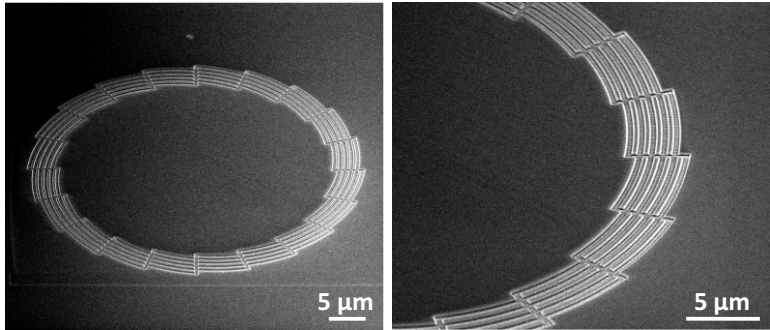


Figure 7.17.: SEM images of the $m = 20$ Archimedean spiral of $40 \mu\text{m}$ diameter milled into a large-sized single-crystalline gold platelet, synthesized according to [50]. On the right side there is a section to illustrate the grating of $\lambda_{\text{LR-SPP}}/2$ for efficient SPP coupling. The SEM views are tilted by 52° .

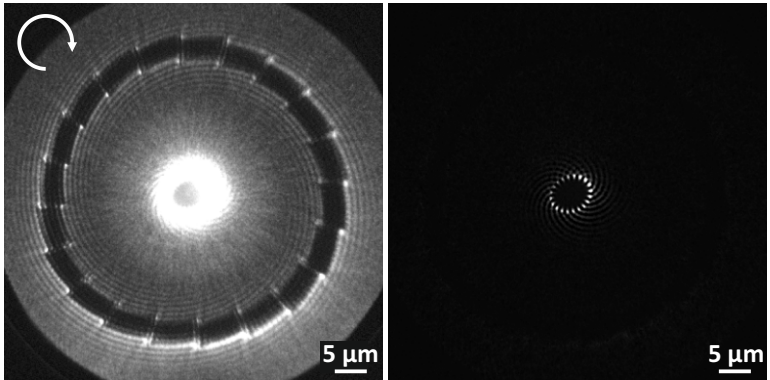


Figure 7.18.: LR SPP excitation with right-hand circularly polarized light on a $m = 20$ Archimedean spiral of $40 \mu\text{m}$ diameter, milled into a large-sized single-crystalline gold platelet. SPPs are excited at the structure and propagate to the center. Due to constructive interference of SPP waves, strong and ring-shaped photo-electron emission takes place in the center. Subtracting the background in the right image reveals the structural details of the central feature, which consists of 20 distinct emission maxima generated by each spiral arm.

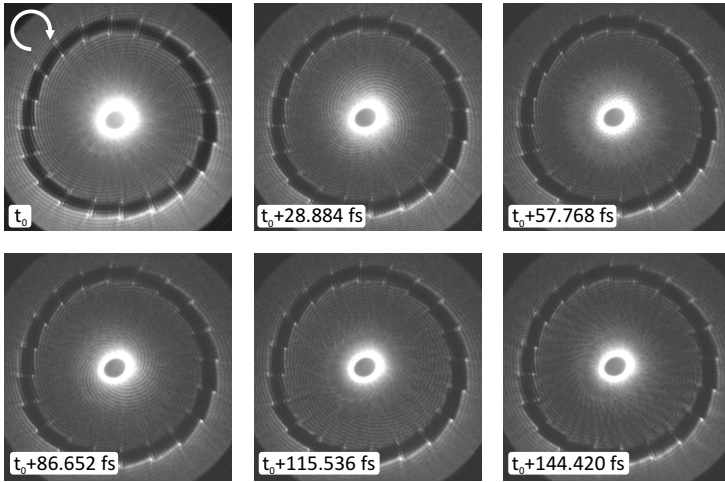


Figure 7.19. Time-resolved 2PPE PEEM image series of the $m = 20$ spiral structure. The LR SPP is excited with circularly polarized light and the images are illustrated in 28.884 fs steps. Here, SPP propagation and interference on a long-time scale can be observed.

light. This image series shows SPP excitation at the 20 spiral arms and propagation to the center. There, SPP interference takes place. For very long delay times, SPP waves are propagating out of the center again and interfere with incoming waves. The transfer of OAM to the LR SPP from the spin angular momentum of the circularly polarized incident light is illustrated impressively, giving a twist to the plasmonic emission pattern. During 20 optical cycles, the SPP pattern performs one full rotation. The two time-resolved movies, with and without background, are provided additionally on the memory stick.

Within this work, the dynamics of the plasmonic angular orbital momentum, generated by helical plasmonic spiral structures in single-crystalline gold films, is visualized and established in time-resolved 2PPE PEEM experiments with sub-femtosecond time steps. The distinct dynamic features, arising in the center of structures with increasing geometrical charge m are investigated and discussed within this chapter, using structures of geometri-

cal charges $m = 1$, $m = 4$ and $m = 20$. These results raise new and fundamental questions requiring some further experiments have to be performed.

For geometrical charge $m = 1$, formation of the central plasmonic feature depends on the polarization direction (spin angular momentum) of the incident circularly polarized light. In contrast, the $m = 4$ spiral shows the same plasmon pattern of four emission maxima for both polarization directions. This is also applicable for the $m = 20$ structure. Is this the characteristic behavior of structures having an even number as geometrical charge? Will the plasmonic pattern, excited in an structure with odd geometrical charge change by applying RCP and LCP light? Do time-resolved z PPE PEEM measurements, because of superposition of several different electrical fields, image the reality?

Apart from these fundamental questions concerning the angular momentum transfer from light to SPPs, more questions arise. For example, is it possible to place an object directly into the central point of such PVL structures? For example, nano-objects such as colloids, quantum emitters or molecules. What kind of interaction would take place between the object and the emitted electrons? Would this lead to extraordinary enhanced electron emission? And would it be possible to excite certain molecules into higher energetic states with an angular momentum difference other than the usual ± 1 (RCP and LCP light)? Would it also be possible to further transfer OAM from SR SPPs to the applied object and make it rotate? And in contrast to this, can an object be trapped within an electron emission minimum and observed in PEEM?

7.4 TOWARDS THE REALIZATION OF A PLASMONIC STADIUM BILLIARD EXPERIMENT

7.4.1 *Preliminary Remarks*

During the last century, the stadium billiard experiment was used as model system in quantum research to find evidence of classical chaos in quantum mechanical systems. Two experiments motivated chaos in quantum mechanics. First, a random matrix theory was derived to explain the spectra of compound nuclei. Second, the physics of highly excited hydrogen and alkali atoms in strong magnetic and radio frequency fields could be explained within this theory. Since the 1990s, microwave billiard experiments came up, searching for quantum mechanical descriptions of classical waves.

The link between classical- and quantum mechanics is the correspondence principle, postulating a relation between linear quantum mechanics and nonlinear classical mechanics for large quantum numbers.

In classical mechanics, one aims to find particle trajectories in various potentials. Considering a circular billiard first, the trajectories are regular with two constants of motion, the total energy and the angular momentum. Because of these two degrees of freedom, the system is integrable. The distance between two trajectories increases linearly with time. Stadium billiard systems however, only have one constant of motion, which is the total energy. The distance between two trajectories increases exponentially with time and therefore adopt chaotic character, see figure 7.20. Numerical integration of the classical trajectories is elementary.

In quantum mechanics, Heisenbergs uncertainty relation determines the initial conditions, which is why the concept of trajectories loses its significance.

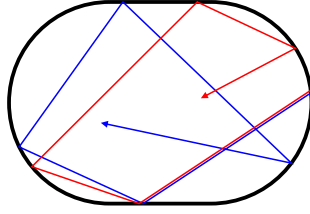


Figure 7.20.: In stadium billiard systems, the distance between two particle trajectories increases exponentially. After some time it is chaotic.

For billiard systems, the stationary Schrödinger equation reduces to a simple wave equation

$$-\frac{\hbar^2}{2m} \left(\frac{\partial^2}{\partial x^2} + \frac{\partial^2}{\partial y^2} \right) \Psi_n = E_n \Psi_n. \quad (7.2)$$

In the absence of potentials, equation (7.2) is equivalent to the time-independent wave equation, which is the Helmholtz equation

$$-\left(\frac{\partial^2}{\partial x^2} + \frac{\partial^2}{\partial y^2} \right) \Psi_n = k_n^2 \Psi_n, \quad (7.3)$$

where Ψ_n is the amplitude of a classical wave field.

Here, the quantum mechanical time-independent Schrödinger equation is equivalent to the classical wave equation and is therefore the starting point for microwave experiments in stadium shaped resonators [83] where the boundary conditions are crucial. From the quantum mechanical point of view, the wave function Ψ must be zero at the boundaries. Considering electromagnetic waves, the tangential component of the electric field and the normal component of the magnetic induction must disappear at the stadium boundaries. Considering two dimensional billiards, the electromagnetic boundary conditions reduce to $E_z = 0$, when z is oriented perpendicular to the resonator. Identifying Ψ with E_z , electromagnetic and quantum mechanical boundary conditions are the same. A semi-classical approach [84] illustrates that

the density of eigenvalues can be decomposed into a monotonic and an oscillatory part. The oscillatory part in the eigenvalue density is the sum over all classical periodic orbits and furthermore, it is shown in [85] that contributions from different periodic orbits can be obtained via Fourier transformation. Therefore, resonances in the reflectance spectrum of such microwave experiments can be attributed to eigenfrequencies and eigenvalues of the stadium billiard system. In addition, eigenfunctions of such microwave resonators can be experimentally determined, as it is shown in [86].

Based on this semi-classical approach [84], wave function simulations are performed within work of King [87]. In figure 7.21 the dynamic of a propagating Gaussian shaped wave packet is illustrated, bouncing back and forth within a stadium resonator.

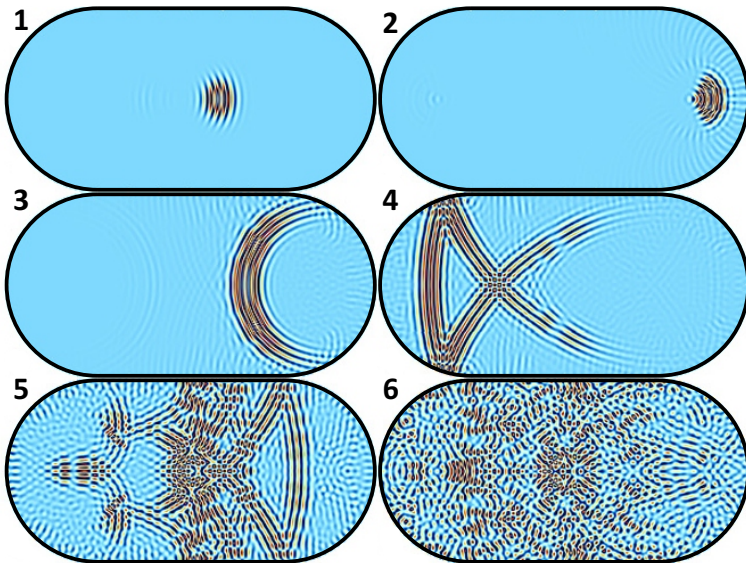


Figure 7.21. Wave function simulation in a stadium billiard system [87]. A wave packet propagates within a stadium. After some time, a chaotic wave pattern has formed.

In image 4 in figure 7.21, the wave package is split up and due to constructive and destructive interference of wave packets, a chaotic standing wave pattern is formed gradually.

One application of this is a high-power semiconductor laser based on a stadium shaped optical resonator [88]. A bow-tie resonance mode leads to a performance improvement and a power increase of three orders of magnitudes into the favorable far-field directions.

7.4.2 *Concepts and Experiments*

Intention of this chapter is to establish a stadium billiard experiment in plasmonics. All components needed for such experiments are developed and introduced within the previous chapters. Time-resolved 2PPE PEEM offers the opportunity to study plasmon propagation and wave interference on the femtosecond time scale for a great variety of samples. In combination with the atomically flat surfaces of single-crystalline gold platelets and structuring via focused ion beam milling, high quality plasmonic stadium structures are fabricated.

Propagating SPP wave packages are supposed to build up a chaotic system after being reflected several times at the stadium structure boundaries. Large-sized single crystalline gold platelets, synthesized by the method of Radha [50], provide defect-free gold surfaces of several tens of square-micrometers. Stadium structures are milled into the atomically flat plasmonic gold surfaces and described by their long- and short half axis. Two sets of different structure sizes are chosen, having half axis lengths of $10 \times 15 \mu\text{m}$ and $20 \times 30 \mu\text{m}$, respectively, which is quite convenient for LR SPP propagation. Furthermore, tiny structural variations such as intrusions or scatterers are placed somewhere in the stadium. Furthermore, helicity of the stadium boundary should provide additional disturbance when LR SPPs are excited with circularly polarized light. To launch LR SPPs, stadium structures are designed to have a grating of five parallel FIB cuts of $\lambda_{\text{LR-SPP}}$ pe-

riod. The depth of the FIB cuts is chosen to be around 200 nm, to allow for SPP excitation. Furthermore, the FIB-grating should enable reflection of propagating SPP waves.

The following concept should apply: LR SPPs are excited at the stadium grating and propagate across the structure until having reached the opposite side of the stadium. Here, they should be reflected at the FIB grating. Due to the stadium curvature, SPP waves are reflected in various directions and then superpose with arriving SPP waves. This process should be repeated several times until the superposed wave packages form a chaotic pattern.

Figure 7.22 gives an overview of different types of stadium structures which are considered in the experiment. Images (A) and (B) show structures with $10 \times 15 \mu\text{m}$ half axis length. In (A), a large-sized single-crystalline gold platelet is illustrated. A 5-cut grating of $\lambda_{\text{LR-SPP}}$ period for efficient SPP coupling configures the stadium. Image (B) depicts a stadium structure with a single cut of $\lambda_{\text{LR-SPP}}/2$ width, exhibiting a helical disturbance of geometrical charge $m = 1$. Figures 7.22 (C) to (F) represent stadium structures with half axis of $20 \times 30 \mu\text{m}$ length. The 5-cut stadium in (C), possesses a helical $m = 1$ structure as well, corresponding to a stadium with additional angular momentum, or, as one could say, is providing a rotating stadium frame for the bouncing particle, which could lead to Coriolis forces. This image illustrates that the platelet edges are far away from the stadium structure and therefore, no boundary effects influence SPP propagation and interference. (D) shows a simple stadium structure, surrounded by 5 FIB cuts. The stadium in figure (E) has one small intrusion of diameter $\lambda_{\text{LR-SPP}}/2$ milled near the coupling grating. Such disturbance is supposed to bring additional interference into the propagating LR SPPs. In the SEM image (F), a stadium structure with a 5-cut coupling grating and geometrical charge $m = 2$ is depicted. SPP excitation on such helical structures with circularly polarized light should also allow the creation of higher order orbital angular momenta.

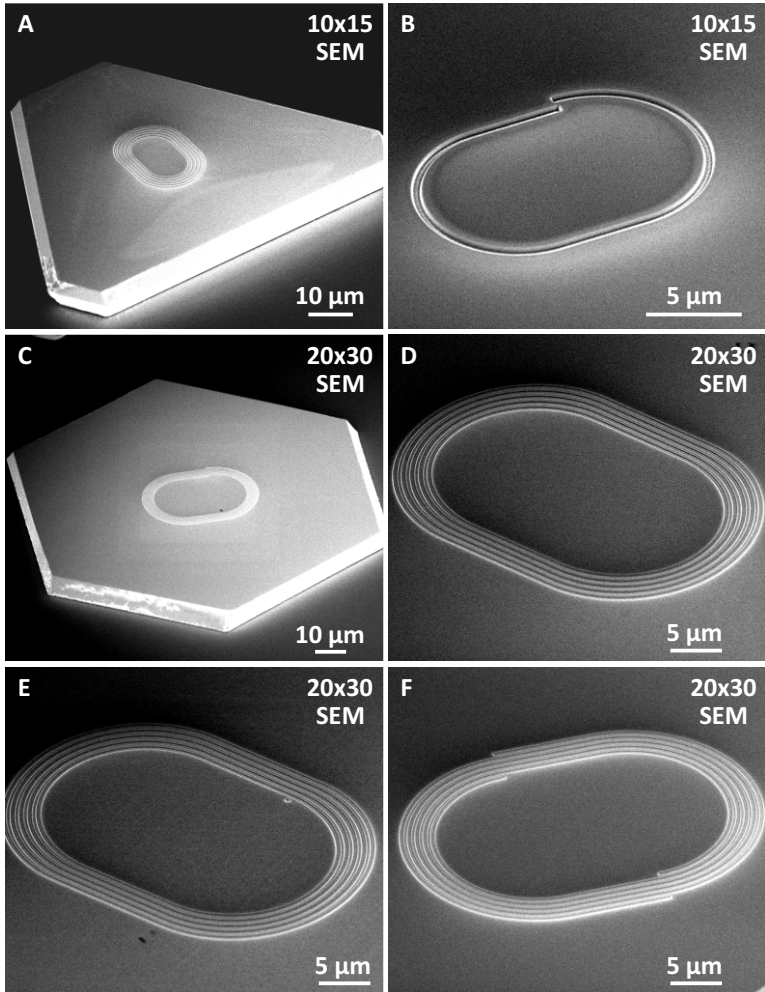


Figure 7.22.: SEM images of stadium structures with different sizes ($10 \times 15 \mu\text{m}$ and $20 \times 30 \mu\text{m}$ length of short- and long half-axis) cut into large-sized single-crystalline gold platelets. Width of the cuts is $\lambda_{\text{LR-SPP}}/2$ and their depth is around 200 nm . To increase the efficiency for SPP coupling to the incident light, stadium structures consist of a grating of five cuts of period $\lambda_{\text{LR-SPP}}$. Some of the stadium structures disturbing different elements like geometrical charges $m = 1$ and $m = 2$ or small intrusions milled into the surface at different positions.

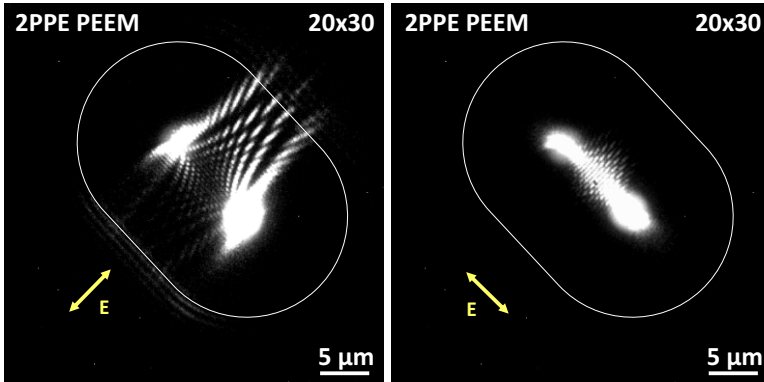


Figure 7.23.: 2PPE PEEM image of a 20x30 stadium structure, illustrating the polarization dependence of the SPP interference pattern between the two focal points. The pattern in left image is excited from incident light with polarization direction perpendicular to the big half-axis. A complex interference pattern is formed between the two focal points. In the right image the polarization direction is rotated by 90° . The interference pattern between the two focal points is overexposed due to intense electron emission.

In figure 7.23, static 2PPE PEEM images of a 20x30 stadium structure, composed of five FIB cuts to facilitates SPP excitation, are illustrated for two different linear polarization directions. In the left image, the polarization direction of the electric field vector is oriented perpendicular to the long half axis. At the two focal points of the stadium structure, intense electron emission takes place. Coming from the focal points, a complex, rhombic LR SPP interference pattern is generated in the center of the stadium. In the right image, the polarization direction is rotated by 90° and is now oriented parallel to the long half axis of the stadium. Parallel to the long half axis, in between the two focal points, intense electron emission takes place. This almost covers the interference pattern from counter-propagating SPP waves. Therefore, during further measurements, the polarization direction is adjusted perpendicular to the long half axis of the stadium structure.

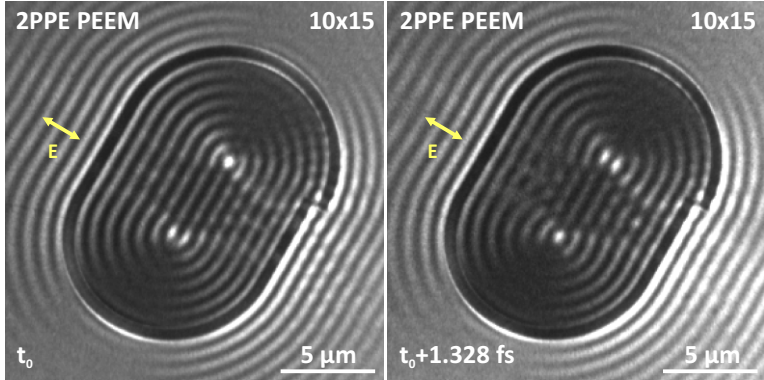


Figure 7.24.: 2PPE PEEM images, recorded at two different delay times, using a 10×15 stadium structure of geometrical charge $m = 1$ and one FIB-cut of $\lambda_{LR-SPP}/2$ for SPP excitation. The polarization direction of the incident field vector is oriented perpendicular to the long half-axis. The images show a LR SPP pattern. Remarkably, the two focal points switch periodically, but out of phase between maximum and minimum within one optical cycle. However, reflection of SPP waves at the stadium FIB-cut is not well observed.

Time resolved PEEM measurements are illustrated in figure 7.24, for the 10×15 stadium of geometrical charge $m = 1$ in figure 7.22 (B). A single FIB-cut of $\lambda_{LR-SPP}/2$ width is used for SPP excitation. The left image is taken at delay time Δt_1 and shows a typical wave pattern of the stadium structure. In its center, the rhombic interference pattern is only slightly indicated, but the two focal points are very pronounced. However, at Δt_1 , due to constructive and destructive interference, one focal point reveals an electron emission maximum while at the second focal point an emission minimum occurs. At delay time Δt_2 , which is half an optical cycle later, the quality of the focal points changes so that the first focal point is a maximum, while the other one has minimum electron emission. After one optical cycle, the initial situation is recovered. This means that the two focal points switch periodically between maximum and minimum phase, shifted with regards to each other by 90° .

Further analysis of the time resolved measurements reveals that

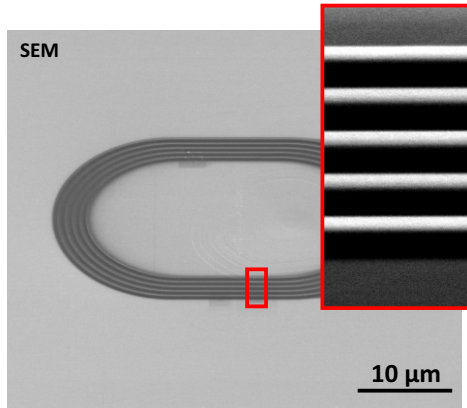


Figure 7.25.: SEM image of a Pt-stadium of $20 \times 30 \mu\text{m}$ lateral size and 300 nm height, which is deposited onto a large single-crystalline gold platelet via ion beam induced deposition, in order to increase the reflectivity for propagating SPP waves. The inset in the red box shows a high magnification image of the deposited platinum ridges.

no reflection of SPP waves takes place at the milled boundaries of the stadium structure. Therefore, chaotic superposition of incoming and reflected SPP waves is not observed within this experimental configuration.

To increase reflection of SPP waves at the stadium boundaries, alternative structuring methods are necessary. As already introduced in [89], SPP reflection is increased drastically by using a ridge pattern, which is applied via ion-beam induced deposition instead of FIB milling into the metal film. In figure 7.25, a 20×30 platinum stadium is illustrated¹⁵, which was deposited onto a large-sized single-crystalline gold platelet. The stadium consists of 5 platinum ridges of roughly 200 nm height applied in a periodic distance of $\lambda_{\text{LR-SPP}}/2$.

The PEEM image of the platinum stadium is shown in figure

¹⁵ Pt-stadium fabrication via ion beam induced deposition: Pierre Kirschbaum, Faculty of Physics and Center for Nanointegration Duisburg-Essen (CENIDE), University of Duisburg-Essen

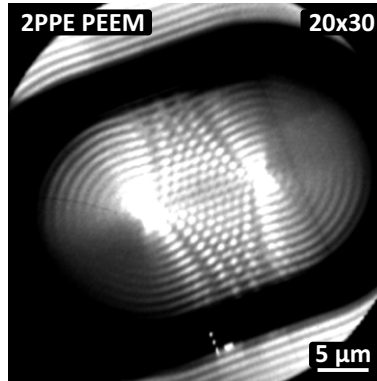


Figure 7.26. 2PPE PEEM image of the Pt-stadium structure again shows the interference pattern of excited LR SPPs. The polarization direction of the incident electric field vector is perpendicular to the long half-axis of the structure. Time-resolved 2PPE PEEM measurements, however, do not show back-reflection and superposition of SPP waves at the platinum ridges.

7.26. LR SPPs are excited with linearly polarized light, oriented perpendicular to the long half axis. The typical picture with two focal points and the SPP interference pattern in between appears. Time-resolved 2PPE PEEM measurements yield information about SPP reflection at the platinum walls and shows again no reflection of SPP waves. There is no significant improvement of the SPP reflection properties in comparison to the FIB milled structures. To achieve SPP wave reflection in stadium structures, different approaches have to be considered for future experiments. For example, materials of very high reflection coefficients could be used for stadium deposition. Furthermore, different structure geometries should be taken into account to study the reflection properties of propagating SPP waves.

CONCLUSION AND OUTLOOK

In this work single crystalline gold platelets are used to study LR- and SR SPPs via 2PPE PEEM measurements.

A completely new procedure is established to synthesize single crystalline gold platelets electrochemically. Due to dissolution of a gold electrode, triangular and hexagonal gold platelets of a few nanometer thickness and lateral dimensions in the micrometer range, precipitate during the electrochemical reaction. Deposition on various substrates allow extensive characterization. Indeed, these electrochemically grown gold platelets turn out to be exclusively composed of gold atoms and have defect free, atomically flat surfaces. TEM- and SAED investigations exhibit single crystallinity in (111)-direction, which is supported by the substrate.

Single crystalline gold platelets on silicon substrates enable excitation and investigation of surface plasmon polaritons via 2PPE PEEM at their material interfaces. Using very thin gold platelets of around 20 nm thickness, two SPPs of different wavelengths can be observed. Due to the high refractive index of silicon at 800 nm excitation wavelength, the SPP wavelength at the gold-silicon interface is reduced drastically to 185 nm, while the SPP wavelength at the gold vacuum interface is 780 nm. During time-resolved pump-probe experiments, the SR SPP phase velocity is determined to be around a quarter of the velocity of light in vacuum.

Focused ion beam milling provides a flexible possibility to structure single crystalline gold platelets. Milling a disk of 2 μm diameter into a single crystalline gold platelet of 22 nm thickness, the SR SPP is focused to a spot of FWHM of 60 nm. In PEEM, photo-electron emission from the plasmon wave is observed and thus, the SR SPP focus can be interpreted as an ultra-small source

of ultrashort electron pulses.

SR SPP excitation with circularly polarized light at helical slits, which are milled into the gold platelet, facilitates OAM transfer from light to the short range plasmon. Time-resolved 2PPE PEEM measurements provide the full dynamical picture of the plasmonic OAM in helical structures of different geometric charges, namely $m = 1, 4,$ and 20 .

Observing LR SPPs propagating in stadium structures on large sized single crystalline gold platelets [50] is the first step towards a plasmonic stadium billiard experiment. Time-resolved interference of counter-propagating SPP waves is observed, depending on the polarization direction of the incident electric field vector. This leads to two focal points with alternating and phase shifted maximum or minimum, respectively. However, within the first experiments SPP wave reflection and therefore superposition of reflected waves cannot be observed.

There are more fundamental ideas emerging from the new electrochemical reaction. Normal incidence 2PPE PEEM on structured single crystalline gold platelets offers fascinating possibilities to investigate pure plasmonic effects. Some of them are listed in the following paragraphs.

The 60 nm plasmon focus in PEEM is an ultra-narrow, pulsed electron source. Therefore, it is extremely attractive to investigate the interaction between this electron beam and various objects. Therefore, a nanoscale object has to be placed directly in the center of the plasmonic disc, where interaction with the focus can take place. Such object could be a colloid, quantum dot or a molecule. One important question is, what kind of interaction can take place. Furthermore, is it possible to bring molecules into excited states due to interaction with these emitted electrons? Is it also possible to trap one object within an plasmonic orbital angular momentum structure and transfer the angular momentum coming from the SR SPP to the object?

Further experiments on higher order helical structures are desirable using geometrical charges m of odd numbers. Furthermore, SPP excitation with light of different polarization states, like ra-

dially or azimuthally polarized light could induce interesting effects. More detailed PEEM simulations are necessary to fundamentally understand the result and furthermore, predict new effects theoretically.

Moreover, patterning single crystalline gold platelets with metasurfaces, which is a structured surface, containing different shaped plasmonic antenna elements can be used to manipulate the incident light.

The growth mechanism of single crystalline gold platelets during the electrochemical process is still unknown. To learn more about the crystallization process it is desirable to transfer the electrochemical reaction into a liquid cell TEM. Therefore, the process has to be miniaturized and adjusted for TEM investigations. With the TEM, it should be possible to in-situ observe the platelet growth and formation mechanism on an atomic level.

The experiments introduced within this thesis are just an initial point. Out of this, there are already new ongoing projects. In the following, this work is acknowledged and described briefly.

- Large sized single crystalline gold platelets [50] are used as substrates for fluorescence enhancement measurements¹⁶. Therefore, as illustrated in figure 8.1, silver cubes of around 80 nm to 100 nm side lengths are dispersed on these single crystalline gold platelets. A thin polymer film, containing appropriate dye molecules, covers the gold platelet and produces a small gap between the silver cube and platelet. Plasmon excitation in the silver cube leads to strong field enhancement in the gap and therefore excitation of the dye molecules, which is expected to cause fluorescence enhancement and changes in lifetime of different dye molecules [90]. In the right part of figure 8.1, a dark field image of a single crystalline gold platelet covered with silver cubes is depicted. The different colors of the silver cubes correspond to their plasmon resonance.

¹⁶ Simon Ristok, 4th Physics Institute, University of Stuttgart

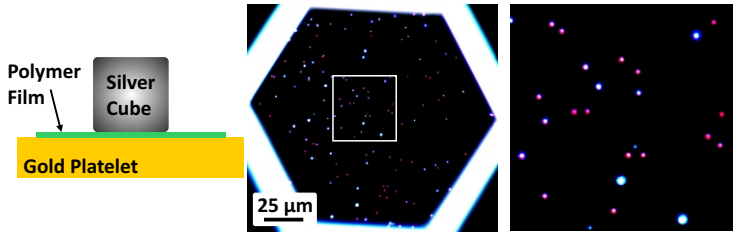


Figure 8.1.: Schematic cross-section through a plasmonic patch antenna, facilitating fluorescence enhancement investigations. Dark field image, showing silver cubes dispersed on top of a large single crystalline gold platelet.

- Surface enhanced infrared absorption¹⁷ [91] is a well established method to detect molecular vibrational signals aided by a single linear plasmonic rod antenna. In figure 8.2, the plasmonic antenna is milled out of a triangular single crystalline gold platelet and covered with a monolayer of octadecanethiol (ODT), which contains CH_2 molecules. The fundamental plasmonic resonance of the single crystalline gold antenna is excited by parallel polarized light and located at a wavenumber of about 2800 cm^{-1} . In addition to the fundamental resonance, two more features are observed at 2850 cm^{-1} and 2917 cm^{-1} , which can be ascribed to the symmetric ($2850 - 2863\text{ cm}^{-1}$) and asymmetric ($2916 - 2936\text{ cm}^{-1}$) stretch vibrations of the CH_2 molecule. For excitation with light polarized perpendicular to the antenna, none of these features is visible. Due to the electromagnetic field enhancement caused by the plasmon resonance, the molecular vibrational signal is enhanced drastically up to one million compared to the vibrational signal without antenna structure. The enhancement factor of CH_2 stretch vibrations measured on a polycrystalline gold antenna structures, fabricated by colloidal hole-mask lithography and tilted angle rotation evaporation, is 20000 [92]. This is extremely encouraging and in fu-

¹⁷ Frank Neubrech, 4th Physics Institute, University of Stuttgart, Jochen Vogt, and Christian Huck, Kirchhoff Institute for Physics, Heidelberg University

ture, this concept will be used to detect smallest molecular changes, for example conformational changes in proteins.

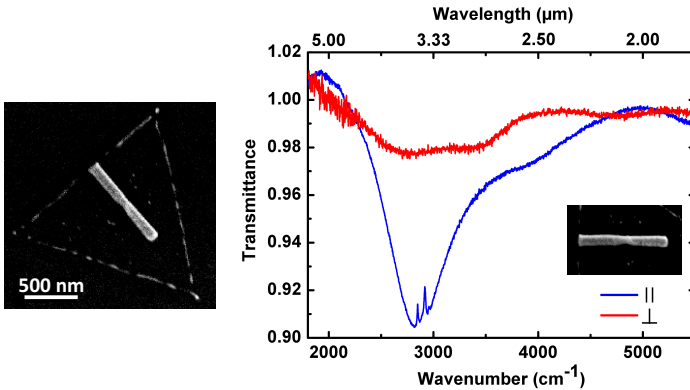


Figure 8.2.: A rod antenna, milled out of a triangular single crystalline gold platelet is covered with a monolayer of ODT. Infrared spectroscopy reveals the enhanced vibrational signal of the adsorbed molecules. The enhancement factor is close to one million.

- Single crystalline gold platelets can also serve as substrates for surface enhanced Raman spectroscopy¹⁸. Therefore, a monolayer of methylene blue is applied to the platelet surface and the Raman signal is measured at different positions. In figure 8.3, the measurement positions on the platelet and the corresponding Raman signals are illustrated. In the platelet center, only a tiny Raman signal can be measured due to the atomically flat surface of the gold platelet. The Raman signal increases slightly at an edge position. At the tip position however, the Raman signal of methylene blue increases enormously. Therefore, single crystalline gold platelets will be used as substrates for localized Raman spectroscopy in several future projects.

¹⁸ Simon Ristok, and Frank Neubrech, 4th Physics Institute, University of Stuttgart. Armin Schulz, Max Planck Institute for Solid State Research, Stuttgart

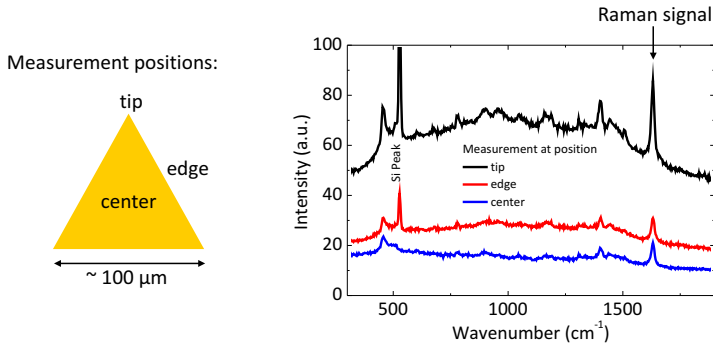


Figure 8.3.: Surface enhanced Raman spectroscopy on large single crystalline gold platelets, covered with a monolayer methylene blue, is performed at different positions: in the center, at an edge and at a tip. The corresponding Raman signals are plotted in the diagram aside. At the platelet tip, the Raman signal is highest.

- Short range SPPs on single crystalline gold platelets can be excited with scanning nearfield optical microscope (SNOM)¹⁹ as well. Figure 8.4 illustrates SNOM images of the SR SPP. A helium-neon laser of 633 nm central wavelength is used for SPP excitation, resulting in a measured SR SPP wavelength of approximately 90 nm. Again, for SR SPP focusing, a disk of 2 μm diameter is milled into the gold platelet and a concentric grating of 150 nm period is utilized to assist SPP excitation. Here, due to the smaller decay length of SR SPPs, plasmon focusing is not possible.

Considering the SPP dispersion relation at gold-silicon interfaces, as shown in figure 2.7, the SR SPP wavelength can be tuned due to variation of the excitation wavelength. Within the framework of this experiment, the SR SPP wavelength is mapped by using a wavelength tunable excitation source. Furthermore, the minimum SR SPP wavelength pos-

¹⁹ Pablo Alonso-Gonzalez, and Rainer Hillenbrand, CIC nanoGUNE, Donostia-San Sebastián, Spain. Divya Virmani, and Stefan Kaiser, Max Planck Institute for Solid State Research, Stuttgart

sible, which is expected to be 70 nm at 537 nm excitation, will be determined experimentally.

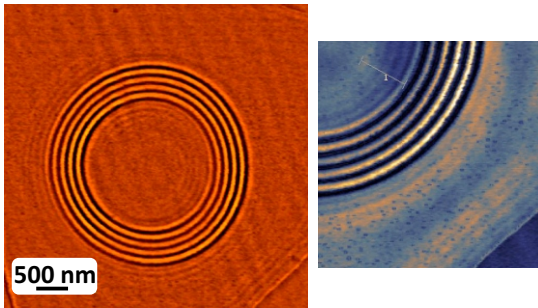


Figure 8.4.: Excitation of SR SPPs on single crystalline gold platelets via SNOM. The excitation wavelength is 633 nm and the resulting SR SPP wavelength is about 90 nm. Within the disk of 2 μm diameter, concentric SR SPP waves are excited. However, due to their short decay length, no SPP focus can form.

- During a second SNOM experiment on electrochemically grown single crystalline gold platelets²⁰, SPPs are excited at a wavelength of 1500 nm for parallel and perpendicular polarization with respect to the marked platelet edge. The results are illustrated in figure 8.5. The topography images on the left side confirm once more the high quality and the atomically flat surface character of single crystalline gold platelets. Furthermore, amplitude and phase images represent the typical long-range SPP pattern for the two different polarization directions. The long-range SPP wavelength roughly correlates to the 1500 nm excitation wavelength. It is remarkable that at platelet edges, a higher-order wedge plasmon mode is excited like already shown in chapter 5.5 during performed EFTEM measurements.

²⁰ Vladimir Zenin, University of Southern Denmark, Odense, Denmark

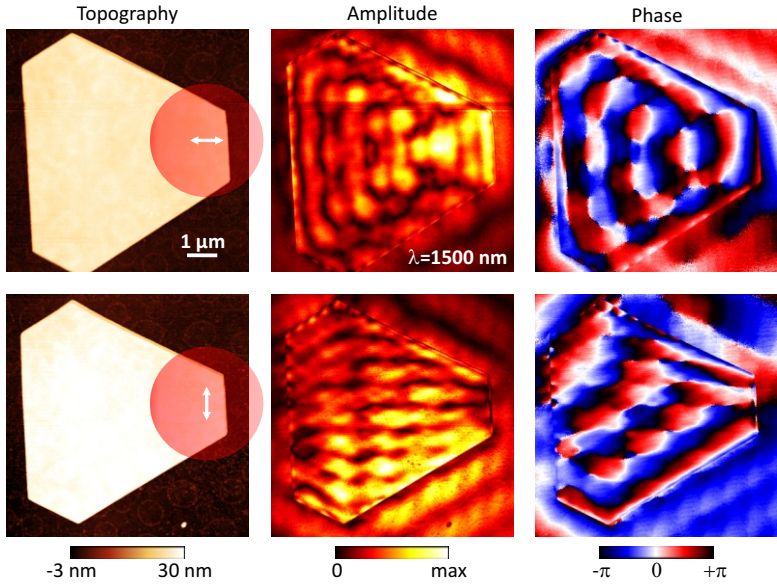


Figure 8.5.: SNOM measurements with $\lambda_0 = 1500$ nm excitation wavelength. AFM, as well as SPP amplitude- and phase images are summarized. Long-range SPPs are excited parallel and perpendicular to the marked platelet edge and show the typical interference pattern. At the platelet edges, a wedge plasmon mode is excited.

- It is not only of interest to vary the SR SPP wavelength by changing the excitation wavelength but also by modifying the surrounding material. Of special interest are 2D-materials²¹, for example graphene, h-BN or molybdenum disulfide (MoS_2). In the left part of figure 8.6, single crystalline gold platelets are directly synthesized on graphene multilayers. This future project will investigate plasmonic interactions between the gold platelet and the graphene. SPP excitation will be performed via 2PPE PEEM and SNOM. Furthermore, it should be investigated if by choosing single crystalline gold platelets of appropriate size, as in [77],

²¹ Patrick Herlinger, Max Planck Institute for Solid State Research, Stuttgart

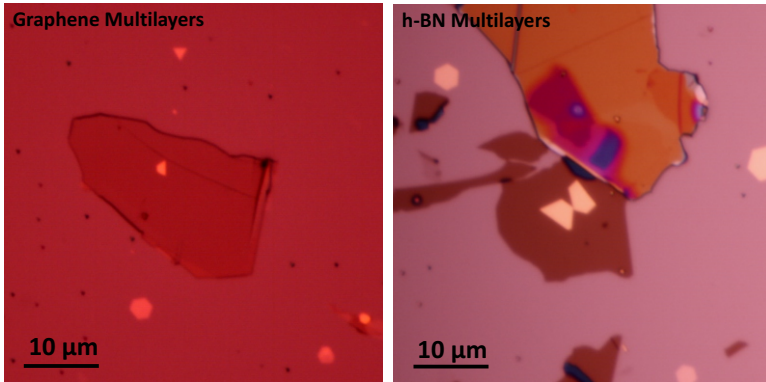
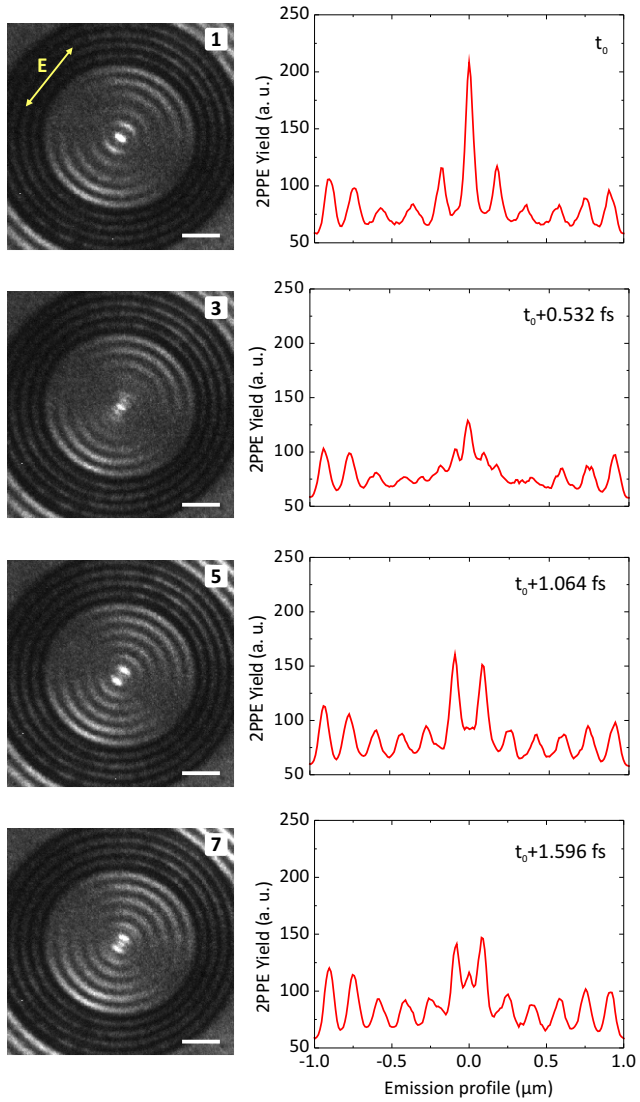


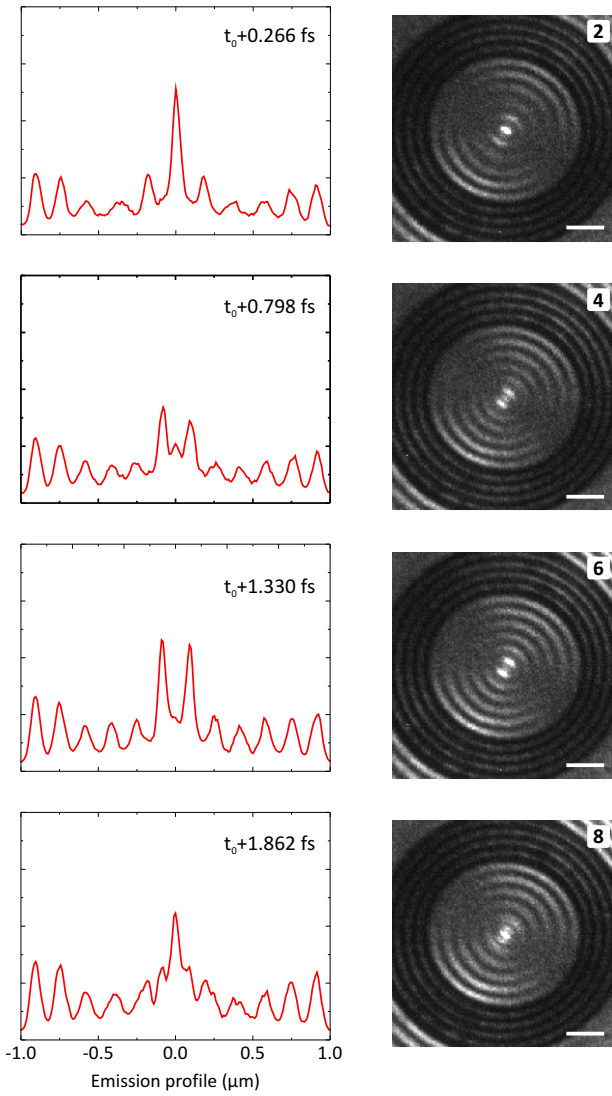
Figure 8.6.: Single crystalline gold platelets deposited on graphene- and h-BN multilayers. Appropriate size of the gold platelet should enable SPP excitation in graphene. Furthermore, change of the environmental material should also modify the SPP wavelength.

to transfer SPPs from the gold platelet to the graphene. The right image of figure 8.6 shows single crystalline gold platelets utilizing multilayer h-BN as substrate. Here, the SR SPP wavelength should increase due to the smaller refractive index of h-BN.

APPENDIX

Full time-resolved picture of the SR SPP focus during one optical cycle, illustrated in 0.266 fs steps and showing PEEM images as well as the corresponding emission profile cross-sections. The emission profile cross section is taken parallel to the polarization direction of the incident electric field vector, directly through the focus. This evolution illustrates the focus maximum decaying to minimum electron emission in the center of the disk and rising up again. All intermediate states are shown. The scale bar is 500 nm.





ACRONYMS

2PPE	two-photon photoemission
AFM	atomic force microscopy
CE	counter electrode
EDX	energy dispersive X-ray
EFTEM	energy filtered transmission electron microscopy
FIB	focused ion beam
fs	femtosecond
FWHM	full width at half maximum
h-BN	hexagonal boron nitride
HCl	hydrochloric acid
ITO	indium tin oxide
LEEM	low energy electron microscopy
LR	long range
MIM	metal-insulator-metal
MoS₂	molybdenum disulfide
NI	Normal incidence
OAM	orbital angular momentum
ODT	octadecanethiol
PEEM	photoemission electron microscopy
PVL	plasmonic vortex lens

APPENDIX

SAED selected area electron diffraction

SAM spin angular momentum

SEM scanning electron microscopy

SNOM scanning nearfield optical microscope

SPP surface plasmon polariton

SR short range

TE transverse electric

TEM transmission electron microscope

TM Transverse magnetic

WE working electrode

BIBLIOGRAPHY

- [1] M. Born and E. Wolf, *Principles of Optics* (Cambridge University Press, 1999), 7. edn.
- [2] J. C. Maxwell, *A Treatise on Electricity and Magnetism*, Vol. 1 and 2 (Dover reprint, 1954), 3. edn.
- [3] E. K. Abbe, *Abhandlungen über die Theorie des Mikroskops* (Gustav Fischer, Jena, 1004).
- [4] S. W. Hell and J. Wichman, "Breaking the diffraction resolution limit by stimulated emission: stimulated-emission-depletion fluorescence microscopy," *Opt. Lett.* **19**, 780 – 782 (1994).
- [5] L. Novotny and B. Hecht, *Principles of Nano-Optics* (Cambridge University Press, 2006).
- [6] S. A. Maier, *Plasmonics: Fundamentals and Applications* (Springer Science+Business Media LLC, 2007).
- [7] E. N. Economou, "Surface Plasmons in Thin Films," *Phys. Rev.* **182**, 539–554 (1969).
- [8] H. Raether, *Surface Plasmons on Smooth and Rough Surfaces and on Gratings* (Springer-Verlag, 1988).
- [9] C. F. Bohren and D. R. Huffman, *Absorption and Scattering of Light by Small Particles* (Viley-VCH, Weinheim, 2004).
- [10] U. Kreibig and M. Vollmer, *Optical Properties of Metal Clusters* (Springer-Verlag, 1993).
- [11] N. Liu and H. Giessen, "Coupling effects in optical metamaterials," *Angew. Chemie - Int. Ed.* **49**, 9838–9852 (2010).

- [12] N. Meinzer, W. L. Barnes, and I. R. Hooper, "Plasmonic meta-atoms and metasurfaces," *Nat Phot.* **8**, 889–898 (2014).
- [13] J.-S. Huang, V. Callegari, P. Geisler, C. Brünig, J. Kern, J. C. Prangasma, X. Wu, T. Feichtner, J. Ziegler, P. Weinmann, M. Kamp, A. Forchel, P. Biagioni, U. Sennhauser, and B. Hecht, "Atomically flat single-crystalline gold nanostructures for plasmonic nanocircuitry," *Nat. Commun.* **1**, 150 (2010).
- [14] A. V. Zayats, I. I. Smolyaninov, and A. A. Maradudin, "Nano-optics of surface plasmon polaritons," *Phys. Rep.* **408**, 131–314 (2005).
- [15] D. Sarid, "Long-Range Surface -Plasma Waves on Very Thin Metal Films," *Phys. Rev. Lett.* **47**, 1927–1930 (1981).
- [16] W.-j. Lee, J.-e. Kim, and H. Y. Park, "Silver superlens using antisymmetric surface plasmon modes," *Opt. Express* **18**, 4780–4782 (2010).
- [17] H. Boersch, J. Geiger, A. Imbusch, and N. Niedrig, "High Resolution Investigation of the Energy Losses of 30 keV Electrons in Aluminum Foils of Various Thicknesses," *Phys. Lett.* **22**, 146–147 (1966).
- [18] J. B. Swan, A. Otto, and H. Fellenzer, "Observed Retardation Effects on the Energy of the ω -Surface Plasmons in Thin Aluminium Foils," *Phys. Status Solidi* **23**, 171–176 (1967).
<http://doi.wiley.com/10.1002/pssb.19670230115>
- [19] J. J. Burke, G. I. Stegeman, and T. Tamir, "Surface-polariton-like waves guided by thin, lossy metal films," *Phys. Rev. B* **33**, 5186–5201 (1986).
- [20] B. Prade, J. Y. Vinet, and A. Mysyrowicz, "Guided optical waves in planar heterostructures with negative dielectric constant," *Phys. Rev. B* **44**, 13 556–13 572 (1991).

- [21] I. Hooper and J. Sambles, "Coupled surface plasmon polaritons on thin metal slabs corrugated on both surfaces," *Phys. Rev. B* **70**, 045 421 (2004).
<http://link.aps.org/doi/10.1103/PhysRevB.70.045421>
- [22] D. Woolf, M. Loncar, and F. Capasso, "The forces from coupled surface plasmon polaritons in planar waveguides." *Opt. Express* **17**, 19 996–20 011 (2009).
- [23] L. Fu, H. Schweizer, T. Weiss, and H. Giessen, "Optical properties of metallic meanders," *J. Opt. Soc. Am. B* **26**, B111 (2009).
- [24] P. B. Johnson and R.-W. Christy, "Optical constants of the noble metals," *Phys. Rev. B* **6**, 4370 (1972).
- [25] D. Podbiel, P. Kahl, and F.-J. Meyer zu Heringdorf, "Analysis of the contrast in normal-incidence surface plasmon photoemission microscopy in a pump-probe experiment with adjustable polarization," submitted (2015).
- [26] R. H. Ritchie, "Plasma Losses by Fast Electrons in Thin Films," *Phys. Rev.* **106**, 874–881 (1957).
- [27] C. J. Powell and J. B. Swan, "Origin of the Characteristic Electron Energy Losses in Aluminum," *Phys. Rev.* **115**, 869–875 (1959).
- [28] C. J. Powell and J. B. Swan, "Origin of the Characteristic Electron Energy Losses in Magnesium," *Phys. Rev.* **116**, 81–83 (1959).
- [29] E. A. Stern and R. A. Ferrell, "Surface Plasma Oscillations of a Degenerate Electron Gas," *Phys. Rev.* **120**, 130–136 (1960).
- [30] R. Vincent and J. Silcox, "Dispersion of Radiative Surface Plasmons in Aluminum Films by Electron Scattering," *Phys. Rev. Lett.* **31**, 1487–1490 (1973).

- [31] E. Kretschmann and H. Raether, "Radiative decay of non-radiative surface plasmons excited by light," *Z. Naturforsch.* **23**, 2135–2136 (1968).
- [32] A. Otto, "Excitation of Nonradiative Surface Plasma Waves in Silver by the Method of Frustrated Total Reflection," *Zeitschrift für Physik* **216**, 398–410 (1968).
- [33] A. M. Yao and M. J. Padgett, "Orbital angular momentum: origins, behavior and applications," *Adv. Opt. Photonics* **3**, 161–204 (2011).
- [34] K. Bliokh, F. Rodríguez-Fortuño, F. Nori, and A. Zayats, "Spin-orbit interactions of light," *Nat. Photonics* **9**, 796–808 (2015).
- [35] F. Cardano and L. Marrucci, "Spin-orbit photonics," *Nat. Photonics* **9**, 776–778 (2015).
- [36] J. H. Poynting, "The Wave Motion of a Revolving Shaft , and a Suggestion as to the Angular Momentum in a Beam of Circularly Polarised Light Author (s): J . H . Poynting Source : Proceedings of the Royal Society of London . Series A , Containing Papers of a Published by," *Proc. R. Soc. Lond. A Ser. A* **82**, 560–567 (1909).
- [37] R. A. Beth, "Mechanical Detection and Measurement of the Angular Momentum of Light," *Phys. Rev.* **50**, 115–125 (1936).
- [38] L. Allen R. J. C. Spreeuw and M. W. B. J. P. Woerdman, "Optical Angular Momentum of Light and the Transformation of Lauguerre-Gauss Laser Modes," *Phys. Rev. A* **45**, 8185–8189 (1992).
- [39] Y. Gorodetski, A. Niv, V. Kleiner, and E. Hasman, "Observation of the spin-based plasmonic effect in nanoscale structures," *Phys. Rev. Lett.* **101**, 1–4 (2008).

- [40] H. Kim, J. Park, S.-W. Cho, S.-Y. Lee, M. Kang, and B. Lee, "Synthesis and Dynamic Switching of Surface Plasmon Vortices with Plasmonic Vortex Lens," *Nano Lett.* **10**, 529–536 (2010).
- [41] S.-W. Cho, J. Park, S.-Y. Lee, H. Kim, and B. Lee, "Coupling of spin and angular momentum of light in plasmonic vortex," *Opt. Express* **20**, 10 083 (2012).
- [42] Z. Shen, Z. J. Hu, G. H. Yuan, C. J. Min, H. Fang, and X.-C. Yuan, "Visualizing orbital angular momentum of plasmonic vortices." *Opt. Lett.* **37**, 4627–4629 (2012).
- [43] A. David, B. Gjonaj, Y. Blau, S. Dolev, and G. Bartal, "Nanoscale shaping and focusing of visible light in planar metal–oxide–silicon waveguides," *Optica* **2**, 1045 (2015).
- [44] G. Spektor, A. David, B. Gjonaj, G. Bartal, and M. Orenstein, "Metafocusing by a Metasprial Plasmonic Lens," *Nano Lett.* **15**, 5739–5743 (2015).
- [45] G. Spektor, A. David, B. Gjonaj, L. Gal, G. Bartal, and M. Orenstein, "Linearly dichroic plasmonic lens and heterochiral structures," *Opt. Express* **24**, 2436 (2016).
- [46] C. H. Hamann and W. Vielstich, *Elektrochemie* (Viley-VCH, Weinheim, 2005), 4. edn.
- [47] D. M. Kolb, "Electrochemical Surface Science," *Angew. Chemie Int. Ed.* **40**, 1162–1181 (2001).
- [48] D. Kolb, "An atomistic view of electrochemistry," *Surf. Sci.* **500**, 722–740 (2002).
- [49] Z. Guo, Y. Zhang, Y. DuanMu, L. Xu, S. Xie, and N. Gu, "Facile synthesis of micrometer-sized gold nanoplates through an aniline-assisted route in ethylene glycol solution," *Colloids and Surfaces A: Physicochemical and Engineering Aspects* **278**, 33–38 (2006).

- [50] B. Radha, M. Arif, R. Datta, T. K. Kundu, and G. U. Kulka-rni, "Movable Au microplates as fluorescence enhancing substrates for live cells," *Nano Research* **3**, 738–747 (2010).
- [51] J. H. Park, N. M. Schneider, J. M. Grogan, M. C. Reuter, H. H. Bau, S. Kodambaka, and F. M. Ross, "Control of Electron Beam-Induced Au Nanocrystal Growth Kinetics through So-lution Chemistry." *Nano Lett.* **15**, 5314–5320 (2015).
- [52] M. T. Reetz and W. Helbig, "Size-Selective Synthesis of Nanostructured Transition Metal Clusters," *J. Am. Chem. Soc.* **116**, 7401–7402 (1994).
- [53] C. Huang, Y. Su, and S. Wu, "The effect of solvent on the etching of ITO electrode," *Mater. Chem. Phys.* **84**, 146–150 (2004).
- [54] J. Nelayah, L. Gu, W. Sigle, C. T. Koch, I. Pastoriza-Santos, L. M. Liz-Marzán, and P. a. van Aken, "Direct imaging of surface plasmon resonances on single triangular silver nanoprisms at optical wavelength using low-loss EFTEM imaging." *Opt. Lett.* **34**, 1003–1005 (2009).
- [55] L. Gu, W. Sigle, C. T. Koch, B. Ögüt, P. a. van Aken, N. Talebi, R. Vogelgesang, J. Mu, X. Wen, and J. Mao, "Resonant wedge-plasmon modes in single-crystalline gold nanoplatelets," *Phys. Rev. B* **83**, 195433 (2011).
- [56] P. Kahl, S. Wall, C. Witt, C. Schneider, D. Bayer, A. Fischer, P. Melchior, M. Horn-von Hoegen, M. Aeschlimann, and F. J. Meyer zu Heringdorf, "Normal-Incidence Photoemis-sion Electron Microscopy (NI-PEEM) for Imaging Surface Plasmon Polaritons," *Plasmonics* **9**, 1401–1407 (2014).
- [57] A. Kubo, K. Onda, H. Petek, Z. Sun, Y. S. Jung, and H. K. Kim, "Femtosecond imaging of surface plasmon dynamics," *Nano Lett.* **5**, 1123–1127 (2005).
- [58] E. Knoesel, a. Hotzel, T. Hertel, M. Wolf, and G. Ertl, "Dy-namics of photoexcited electrons in metals studied with

- time-resolved two-photon photoemission," *Surf. Sci.* **368**, 76–81 (1996).
- [59] H. Petek and S. Ogawa, "Femtosecond time-resolved two-photon photoemission studies of electron dynamics in metals," *Prog. Surf. Sci.* **56**, 239–310 (1997).
- [60] J. G. Endriz and W. E. Spicer, "Study of aluminum films. II. Photoemission studies of surface-plasmon oscillations on controlled-roughness films," *Phys. Rev. B* **4**, 4159–4184 (1971).
- [61] T. Tsang, T. Srinivasanrao, and J. Fischer, "Surface-Plasmon Field-Enhanced Multiphoton Photoelectric-Emission From Metal-Films," *Phys. Rev. B* **43**, 8870–8878 (1991).
- [62] M. Aeschlimann, C. A. Schmittenmaer, H. E. Elsayed-Ali, R. J. D. Miller, J. Cao, Y. Gao, and D. A. Mantell, "Observation of surface enhanced multiphoton photoemission from metal surfaces in the short pulse limit," *J. Chem. Phys.* **102**, 8606–8613 (1995).
- [63] O. Schmidt, M. Bauer, C. Wiemann, R. Porath, M. Scharte, O. Andreyev, G. Schönhense, and M. Aeschlimann, "Time-resolved two photon photoemission electron microscopy," *Appl. Phys. B* **74**, 223–227 (2002).
- [64] A. Kubo, N. Pontius, and H. Petek, "Femtosecond microscopy of surface plasmon polariton wave packet evolution at the silver/vacuum interface." *Nano Lett.* **7**, 470–5 (2007).
- [65] F.-J. Meyer zu Heringdorf, L. Chelaru, S. Möllenbeck, D. Thien, and M. Horn-von Hoegen, "Femtosecond photoemission microscopy," *Surf. Sci.* **601**, 4700–4705 (2007).
- [66] C. Lemke, T. Leißner, S. Jauernik, A. Klick, J. Fiutowski, J. Kjelstrup-hansen, H.-g. Rubahn, M. Bauer, A. Physik, and

- C.-a.-u. Kiel, "Mapping surface plasmon polariton propagation via counter-propagating light pulses," *20*, 12 877–12 884 (2012).
- [67] F.-J. Meyer zu Heringdorf, P. Kahl, A. Makris, S. Sindermann, D. Podbiel, and M. Horn-von Hoegen, "Signatures of plasmoemission in two photon photoemission electron microscopy," *Proc. SPIE* **9361**, 93 610W (2015).
- [68] W. L. Barnes, A. Dereux, and T. W. Ebbesen, "Surface plasmon subwavelength optics." *Nature* **424**, 824–830 (2003).
- [69] J. A. Schuller, E. S. Barnard, W. Cai, Y. C. Jun, J. S. White, and M. L. Brongersma, "Plasmonics for extreme light concentration and manipulation." *Nat. Mater.* **9**, 193–204 (2010).
- [70] H. J. Lezec, a. Degiron, E. Devaux, R. a. Linke, L. Martin-Moreno, F. J. Garcia-Vidal, and T. W. Ebbesen, "Beaming light from a subwavelength aperture." *Science* **297**, 820–822 (2002).
- [71] E. T. Rogers, J. Lindberg, T. Roy, S. Savo, J. E. Chad, M. R. Dennis, and N. I. Zheludev, "A super-oscillatory lens optical microscope for subwavelength imaging," *Nat. Mater.* **11**, 432–435 (2012).
- [72] A. Yanai and U. Levy, "The role of short and long range surface plasmons for plasmonic focusing applications." *Opt. Express* **17**, 14 270–14 280 (2009).
- [73] H. T. Miyazaki and Y. Kurokawa, "Squeezing visible light waves into a 3-nm-thick and 55-nm-long plasmon cavity," *Phys. Rev. Lett.* **96**, 097 401 (2006).
- [74] Z. Fei, a. S. Rodin, G. O. Andreev, W. Bao, a. S. McLeod, M. Wagner, L. M. Zhang, Z. Zhao, M. Thiemens, G. Dominguez, M. M. Fogler, a. H. C. Neto, C. N. Lau, F. Keilmann, and D. N. Basov, "Gate-tuning of graphene plasmons revealed by infrared nano-imaging," *Nature* **487**, 82–85 (2012).

- [75] J. Chen, M. Badioli, P. Alonso-González, S. Thongrattanasiri, F. Huth, J. Osmond, M. Spasenović, A. Centeno, A. Pesquera, P. Godignon, A. Zurutuza Elorza, N. Camara, F. J. G. de Abajo, R. Hillenbrand, and F. H. L. Koppens, "Optical nano-imaging of gate-tunable graphene plasmons," *Nature* **487**, 77–81 (2012).
- [76] S. Dai, Z. Fei, Q. Ma, A. S. Rodin, M. Wagner, A. S. McLeod, M. K. Liu, W. Gannett, W. Regan, K. Watanabe, T. Taniguchi, M. Thiemens, G. Dominguez, A. H. Castro Neto, A. Zettl, F. Keilmann, P. Jarillo-Herrero, M. M. Fogler, and D. N. Basov, "Tunable phonon polaritons in atomically thin van der Waals crystals of boron nitride," *Science* **343**, 1125–1129 (2014).
- [77] P. Alonso-González, a. Y. Nikitin, F. Golmar, A. Centeno, A. Pesquera, S. Vélez, J. Chen, G. Navickaite, F. Koppens, A. Zurutuza, F. Casanova, L. E. Hueso, and R. Hillenbrand, "Controlling graphene plasmons with resonant metal antennas and spatial conductivity patterns." *Science* **344**, 1369–73 (2014).
- [78] M. Stockman, "Nanofocusing of Optical Energy in Tapered Plasmonic Waveguides," *Phys. Rev. Lett.* **93**, 137404 (2004).
- [79] D. K. Gramotnev and S. I. Bozhevolnyi, "Nanofocusing of electromagnetic radiation." *Nat. Photonics* **8**, 13–22 (2013).
- [80] Z. Fang, Q. Peng, W. Song, F. Hao, J. Wang, P. Nordlander, and X. Zhu, "Plasmonic focusing in symmetry broken nanocorrals," *Nano Lett.* **11**, 893–897 (2011).
- [81] B. Gjonaj, A. David, Y. Blau, G. Spektor, M. Orenstein, S. Dolev, and G. Bartal, "Sub-100 nm focusing of short wavelength plasmons in homogeneous 2D space," *Nano Lett.* **14**, 5598–5602 (2014).
- [82] T. J. Davis, "Surface plasmon modes in multi-layer thin-films," *Opt. Commun.* **282**, 135–140 (2009).

- [83] H. Stöckmann and J. Stein, ““Quantum”chaos in billiards studied by microwave absorption,” *Phys. Rev. Lett.* **64**, 2215–2218 (1990).
- [84] M. Gutzwiller, “Phase-Integral Approximation in Momentum Space and the Bound States of an Atom,” *J. Math. Phys.* **8**, 1979–2000 (1967).
- [85] D. Wintgen, “Connection between long-range correlations in quantum spectra and classical periodic orbits,” *Phys. Rev. Lett.* **58**, 1589–1592 (1987).
- [86] J. Stein and H. J. Stöckmann, “Experimental determination of billiard wave functions,” *Phys. Rev. Lett.* **68**, 2867–2870 (1992).
- [87] C. King, “Exploring Quantum, Classical and Semiclassical Chaos in the Stadium Billiard,” *Quanta* **3**, 16–31 (2014).
- [88] C. Gmachl, F. Capasso, E. E. Narimanov, J. U. Noeckel, a. D. Stone, J. Faist, D. L. Sivco, and A. Y. Cho, “High-Power Directional Emission from Microlasers with Chaotic Resonators,” *Science* (80-.). **5**, 1556–1564 (1998).
- [89] M. U. González, J.-C. Weeber, A.-L. Baudrion, A. Dereux, A. L. Stepanov, J. R. Krenn, E. Devaux, and T. W. Ebbesen, “Design, near-field characterization, and modeling of 45 degree surface-plasmon Bragg mirrors,” *Phys. Rev. B* **73**, 155–416 (2006).
- [90] A. Rose, T. B. Hoang, F. McGuire, J. J. Mock, C. Ciraci, D. R. Smith, and M. H. Mikkelsen, “Control of radiative processes using tunable plasmonic nanopatch antennas,” *Nano Lett.* **14**, 4797–4802 (2014).
- [91] F. Neubrech, A. Pucci, T. W. Cornelius, S. Karim, A. Garcia-Etxarri, and J. Aizpurua, “Resonant plasmonic and vibrational coupling in a tailored nanoantenna for infrared detection,” *Phys. Rev. Lett.* **101**, 2–5 (2008).

- [92] S. Cataldo, J. Zhao, F. Neubrech, B. Frank, C. Zhang, P. V. Braun, and H. Giessen, "Hole-mask colloidal nanolithography for large-area low-cost metamaterials and antenna-assisted surface-enhanced infrared absorption substrates." *ACS Nano* **6**, 979–85 (2012).

ACKNOWLEDGMENTS

During the time of my PhD thesis, I received a lot of help and support. Therefore, I would like to say thank you to everyone who contributed to this work:

- Prof. Dr. Harald Giessen for giving me all freedom to develop this fascinating topic, for his great ideas, tireless enthusiasm and initiating all collaborations mandatory for this work. In addition, I would like to thank him for all conferences I could attend and all travels I could make.
- Prof. Dr. Peter Michler for his interest in my work and being second supervisor also for my PhD thesis.
- Prof. Dr. Günter Wunner for his interest in my work and being the head of the examination committee.
- Prof. Dr. Frank Meyer zu Heringdorf for his collaboration and hosting me quite often at the University of Duisburg-Essen. Furthermore, I would like to thank him for performing lots of PEEM measurements.
- Philip Kahl and Daniel Podbiel for making the main part of the PEEM measurements, for their patience with the complex gold platelet samples and for the nice atmosphere we always had in the PEEM lab.
- Dr. Liwei Fu and Huyiu Li for giving me the opportunity to use the FIB machine at the Institute of Applied Optics (University of Stuttgart), milling lots of structures and also introducing me into the FIB technique.
- Prof. Dr. Tim Davis for developing a PEEM model within the short period being at the 4th Physics Institute, making all PEEM simulations and providing his software.

- Jun. Prof. Dr. Thomas Weiss for making all dispersion relation simulations and providing his matlab code.
- Grisha Spektor for his collaboration and sharing many ideas, in particular about the orbital angular momentum coupling.
- Simon Ristok for his excellent job in continuing and extending the gold platelet project and providing countless samples of large sized single crystalline gold platelets.
- Dr. Frank Neubrech for being the first one using electrochemically grown gold platelets for his SEIRA projects.
- Dr. Mario Hentschel, Dr. Heiko Linnenbank, and Marco Nägele for proofreading my thesis, for their help and lots of fruitful discussions.
- Dr. Christine von Rekowski for her proficient help regarding all administrative affairs.
- Monika Ubl and Michael Kube for technical support. Furthermore, I would like to thank Monika Ubl for fabricating marker gratings on many gold platelet samples lithographically, facilitating this work significantly.
- Dr. Jun Zhao for being my office mate for many years and the good times we had.
- Last but not least, I would like to thank my whole family and all my friends, in particular my parents for their great support during the past years.

CURRICULUM VITAE

Personal data

Name	Bettina Frank
Day of birth	06.11.1976
Place of birth	Ludwigsburg
Citizenship	German
Address	Kirchenweinbergstrasse 4 71672 Marbach
Mail	b.frank@physik.uni-stuttgart.de

Curriculum vitae

1987 - 1993	Realschule Marbach General Certificate of Secondary Education
1993 - 1997	Technical education, hearing aid technician
1997 - 2001	Professional activity as hearing aid technician
2001 - 2004	Kolping-Kolleg, secondary school Advanced courses in Physics, English and Latin
2004 - 2010	Studies of Physics University of Stuttgart Elective subjects: Nuclear- and Biophysics
2009 - 2010	Diploma thesis at the 4 th Physics Institute, University of Stuttgart: <i>Large area fabrication of metamaterials by tilted shadow nanosphere lithography</i>
2010 - 2016	PhD thesis at the 4 th Physics Institute, University of Stuttgart: <i>Short-Range Surface Plasmonics on single-crystalline Gold Platelets</i>

COLOPHON

This document was typeset using the typographical look-and-feel classicthesis developed by André Miede. The style was inspired by Robert Bringhurst's seminal book on typography "*The Elements of Typographic Style*". classicthesis is available for both L^AT_EX and LyX:

<https://bitbucket.org/amiede/classicthesis/>

Happy users of classicthesis usually send a real postcard to the author, a collection of postcards received so far is featured here:

<http://postcards.miede.de/>

Final Version as of July 8, 2016 (classicthesis).